Voltage control of magnetic anisotropy in ultrathin epitaxial magnetic layers

Dissertation

zur Erlangung des Doktorgrades der Naturwissenschaften
(Dr. rer. nat.)

der Naturwissenschaftlichen Fakultät II
Chemie, Physik und Mathematik

der Martin-Luther-Universität
Halle-Wittenberg

vorgelegt von
Herrn Mirko Ribow
geb. am 02.03.1984 in Ochsenhausen

Tag der Verteidigung: 27.06.2018

Gutachter:
Prof. Dr. Georg Woltersdorf
Prof. Dr. Kathrin Dörr
PD Dr. Andy Thomas

Contents

Dedication

To Lena and Noah

List of Figures

List of Tables

List of acronyms

ALD	Atomic layer deposition
bcc	Body-centered cubic
CAD	Computer aided design
CW	Continuous wedge
fcc	Face-centered cubic
FMR	Ferromagnetic resonance
LBL	Layer-by-layer
LIA	Lock-in amplifier
LLG	Landau-Lifshitz-Gilbert
LMOKE	Longitudinal magneto-optic Kerr effect
MA	Magnetic anisotropy
MBE	Molecular beam epitaxy
MCA	Magnetocrystalline anisotropy
MEA	Magnetoelastic anisotropy
ML	Monolayer
MOKE	Magneto-optic Kerr effect
MSA	Magnetic shape anisotropy
PMOKE	Polar magneto-optic Kerr effect
RHEED	Reflection high-energy electron diffraction
RTE	Resistive thermal evaporator
SOC	Spin-orbit coupling
SW	Step wedge

TMOKE	Transversal magneto-optic Kerr effect
TR-MOKE	Time-resolved magneto-optic Kerr effect
UHV	Ultrahigh vacuum
VCM	Voltage control of magnetism
VCMA	Voltage control of magnetic anisotropy
QCM	Quartz crystal microbalance
3D	Three-dimensional

List of symbols and constants

A	Exchange constant
A_{TM}	TR-MOKE signal
A_l^m	Crystal-field coefficients
a	Lattice constant
a_{e}	Lattice constant of epitaxial and substrate layer
a_{s}	Lattice constant of substrate layer
α	Damping parameter
$\alpha_{\mathrm{x,y,z}}$	Direction cosines in global system
B_{i}	Magnetoelastic coefficient
$B_{\mathrm{i}}^{\mathrm{eff}}$	Effective magnetoelastic coefficient
$B_{\mathrm{i}}^{\mathrm{i}}$	Magnetoelastic interface coefficient
$B_{\mathrm{i}}^{\mathrm{v}}$	Magnetoelastic volume coefficient
$\mathcal{B}_{\mathrm{eff}}$	Effective magnetic induction
$C_{1,2}$	Constants describing erroneous contributions in FMR spectra
c_{ij}	Stiffness tensor components
D_{i}	First order expansion coefficient of magnetoelastic anisotropy
d	Film thickness
d_{c}	Critical film thickness
d_{Co}	Co film thickness
d_{Fe}	Fe film thickness
d_{SRT}	Spin-reorientation film thickness
$\mathcal{D}$	Demagnetizing tensor

$\mathcal{D}_{\mathrm{zz}}$	Demagnetizing tensor element along the surface normal
$\Delta\epsilon_{\mathrm{K}}$	Kerr ellipticity signal in modulation measurement
$\Delta\theta_{\mathrm{K}}$	Kerr rotation signal in modulation measurement
ΔH	Ferromagnetic resonance linewidth
ΔK_{eff}	VCMA induced change in effective out-of-plane MA
ΔU^{pd}	Photodiode signal in modulation measurement
δ	Analyzer angle
E_{d}	Magnetostatic energy density
E_{e}	Elastic energy
E_{MA}	Uniaxial magnetic anisotropy
E_{MEA}	Magnetoelastic anisotropy
E_{MCA}	Magnetocrystalline anisotropy
$E^{\mathrm{c}}_{\mathrm{MCA}}$	Magnetocrystalline anisotropy of a cubic system
$E^{\mathrm{t}}_{\mathrm{MCA}}$	Magnetocrystalline anisotropy of a tetragonal system
E_{MSA}	Magnetic shape anisotropy
E_{p}	P-polarized electric field component
E_{s}	S-polarized electric field component
E_{tot}	Total energy
$E^{\parallel}_{\mathrm{u}}$	Uniaxial in-plane magnetic anisotropy
E_{Z}	Zeeman energy
$E^{\perp}$	Perpendicular magnetic anisotropy
ϵ	Strain
ϵ_{i}	Strain tensor components (in Voigt notation)
ϵ_{K}	Kerr ellipticity
$\epsilon_{\mathrm{K,s}}$	Saturation Kerr ellipticity
$\epsilon^{\pm}_{\mathrm{K,s}}$	Saturation Kerr ellipticity at positive and negative gate voltage

f	Microwave field frequency
f_m	Voltage modulation frequency
Θ	Mixing angle
θ	Polar angle
θ_K	Kerr rotation
$\theta_\mathrm{K,s}$	Saturation Kerr rotation
$\theta^\pm_\mathrm{K,s}$	Saturation Kerr rotation at positive and negative gate voltage
ϕ	Azimuthal angle
ϕ_H	Azimuthal angle between field and [100] cube axis
ϕ_M	Azimuthal Angle between magnetization and [100] cube axis
ϕ_u	Angle between in-plane MA easy axes and [100] cube axis
γ	Surface free energy
γ_e	Surface free energy of the epitaxial layer
γ_i	Surface free energy of the sample interface
γ_s	Surface free energy of the substrate
γ_g	Gyromagnetic ratio
$\vec{H}$	External magnetic field strength
$\vec{H}^\mathrm{loc}$	External magnetic field strength in local system
$\vec{H}_\mathrm{ani}$	Anisotropy field
$\vec{H}^\mathrm{loc}_\mathrm{ani}$	Anisotropy field in local system
$\vec{H}_\mathrm{d}$	Demagnetizing field
$\vec{H}_\mathrm{eff}$	Effective field
H_FMR	Ferromagnetic resonance field
$H^\parallel$	In-plane field component
$H^\perp$	Out-of-plane field component
$H^\pm$	Field at positive and negative gate voltage

h	Microwave excitation field amplitude
$\vec{h}(t)$	Microwave excitation field vector
$\vec{h}^{\mathrm{loc}}(t)$	Microwave excitation field vector in local system
$\mathcal{H}_{\mathrm{eff}}$	Effective magnetic field
$\hbar$	Reduced Planck constant
I	Light intensity
I_0	Light intensity without external magnetic field
η	Lattice mismatch
$\vec{G}$	Reciprocal lattice vector
K	Uniaxial magnetic anisotropy constant
K_{eff}	Effective uniaxial out-of-plane magnetic anisotropy constant
$K_{\mathrm{eff}}^{\mathrm{f}}$	K_{eff} at final gating state
$K_{\mathrm{eff}}^{\mathrm{i}}$	K_{eff} at initial gating state
K_{i}	Interface magnetic anisotropy constant
K_{MSA}	Magnetic shape anisotropy constant
$K_u^{\parallel}$	Uniaxial in-plane magnetic anisotropy constant
K_{v}	Volume magnetic anisotropy constant
$K_2^{\perp}$	Uniaxial out-of-plane magnetocrystalline anisotropy constant
K_4	Biaxial magnetocrystalline anisotropy constant
$K_4^{\perp}$	Biaxial out-of-plane magnetocrystalline anisotropy constant
$K_4^{\parallel}$	Biaxial in-plane magnetocrystalline anisotropy constant
K_6	Sixth order magnetocrystalline anisotropy constant
$\vec{k}_0$	Incident wave vector
$\vec{k}'$	Diffracted wave vector
$\vec{k}_{hk}$	Diffracted wave vector
$\vec{k}_{00}$	Specular beam

κ_l^m	Magnetic anisotropy coefficients
l_{ex}	Exchange length
λ	Magnetostrictive strain
$\vec{M}$	Magnetization vector
$\vec{M}^{\mathrm{loc}}$	Magnetization vector in local system
M_{eff}	Effective magnetization
$\vec{M}_{\mathrm{eq}}$	Magnetization vector at equilibrium
M_{s}	Saturation magnetization
$M^{\perp}$	Out-of-plane magnetization component
$M^{\parallel}$	In-plane magnetization component
M'	In- or out-of plane magnetization component
$\vec{m}(t)$	Dynamic magnetization vector component
$\vec{m}'(t)$	Dynamic magnetization vector component in local system
$m_{\mathrm{v,w}}$	Magnetization oscillation amplitudes in local system
μ_{B}	Bohr magneton
μ_0	Vacuum permeability
N	Number of monolayers
$\hat{n}$	Normal vector
p	Vacuum chamber pressure
p_{b}	Vacuum chamber base-pressure
τ	Film stress
$U_{\mathrm{A,B}}$	Balanced photodiode voltages
U_{g}	Gate voltage
U^{pd}	Photodiode voltage
$U^{\mathrm{pd},\pm}$	Photodiode voltage at positive and negative gate voltage
U_0^{pd}	Photodiode voltage without external magnetic field

$U_{\mathrm{b}}^{\mathrm{pd}}$	Incoherent contribution to photodiode voltage
V	Volume
$Y_l^m(\theta,\phi)$	Orthonormal spherical harmonics
ξ	VCMA coefficient
$\chi_{\mathrm{vv,vw,wv,ww}}$	Susceptibility tensor elements
ω	Microwave field angular frequency
$\hat{x},\hat{y},\hat{z}$	Unit vectors in global system
$\hat{u},\hat{v},\hat{w}$	Unit vectors in local system

1. Introduction

The voltage control of magnetic anisotropy (VCMA) offers exciting possibilities for developing future spintronic applications. In particular VCMA based magnetic random access memory (MRAM) may be attractive, as it could consume significantly less power as compared to devices utilizing the spin transfer torque (STT) for magnetization switching. Besides its relevance for technological applications the VCMA is highly interesting from a fundamental point of view.

This thesis focuses on the VCMA in epitaxial MgO/Fe(Co)-based multilayer structures, which are regarded as archetype for future spintronic applications due to the strong perpendicular magnetic anisotropy (PMA)[1–3], large tunnel magneto resistance (TMR) [4], low STT switching current [5], and promising VCMA [6–52]. From a theoretical point of view the VCMA in MgO/Fe(Co) bilayers is reasonably well described in terms of spin-dependent charge screening [53], which leads to an alteration of the ferromagnet electronic system at the bilayers interface and consequently the interface magnetocrystalline anisotropy (MCA) [54–60]. However, several recent experiments cannot be solely explained by the electronic VCMA. Here strong non-linear [30, 46, 52, 61], hysteretic [6, 47] and v-shaped [27] voltage dependencies, long transient times [28, 30], unexpectedly large high VCMA coefficients [10, 30], a buffer layer dependence of the VCMA coefficient sign [31], and an unexpected magnetic layer thickness dependence [49] have been observed. These effects have been explained by taking into account magneto-ionics [62, 63], charge trapping [17], a possible inverse piezolectric effect in the MgO dielectric layer [35], and thickness-dependent film strain [49, 64]. The in-depth understanding of the physical mechanism of the VCMA is essential for the development of future spintronic applications. The main objectives of this thesis is to establish the experimental methods needed for the preparation of high quality epitaxial MgO/Fe(Co)-based multilayers in which the VCMA can be realized and to explore its physical origin in detail.

An ultrahigh vacuum (UHV) molecular beam epitaxy (MBE) growth chamber has been developed and built-up during the course of this thesis. With this system the epitaxial growth of three different material systems showing the VCMA is established. The samples are based on MgO/Fe/Au, MgO/Fe/Cr and MgO/Co/Fe/Au multilayers. As the electronic VCMA is only at the interface of the dielectric/ferromagnet bilayer in principle one expects a maximum magnitude of the effect for a ferromagnet film thickness of only one atomic layer. Due to imperfections in the epitaxial layer growth, leading to surface roughness, island formation and interdiffusion and which cannot be completely avoided in the experiment, the maximum is rather expected at a thickness of a few atomic layers. In all investigated samples the magnetic film is prepared in a wedge geometry where the film thickness is varied continuously within a few atomic layers over the width of the substrate. The maximum thickness of the prepared wedge in all three samples is only ∼1 nm. The preparation of the magnetic layer in such a wedge geometry allows for a detailed analysis of the magnetic and VCMA properties as a function of film thickness.

The magnetic properties are examined by analyzing in- and out-of-plane magnetization curves measured by MOKE as well as the angular and frequency dependence of the ferromagnetic resonance measured by time-resolved magneto-optic Kerr effect (TR-MOKE). The VCMA is evaluated by measuring the gate voltage effect on the static magnetization curves and the FMR spectra. Furthermore, the VCMA is determined via a modulation technique: the MOKE response is recorded upon modulating the gate voltage via a lock-in amplifier (LIA) while an external magnetic field is sweeped. By properly normalizing the modulation curve, the VCMA coefficient is quantitatively extracted.

An in-depth understanding of the physical origin of the VCMA is obtained by examining the VCMA gate voltage, gating time, and thickness dependence in the MgO/Fe/Au based multilayer structures. The analysis of the VCMA gate voltage and gating time dependence leads to the conclusion that the measured VCMA is a superposition of the electronic VCMA and charge trapping and/or magneto-ionic effects. The onset of magneto-ionic and/or charge trapping is determined at a gating time of 1.3 ms. The VCMA thickness dependence analysis reveals an unexpected increase of the VCMA coefficient with increasing film thickness. This finding is attributed to the inverse piezoelectric effect in the MgO layer and/or a thickness-dependent Au segregation to the Fe surface during epitaxial growth.

The thesis is organized as follows: in chapter 2 the theoretical concepts utilized throughout this thesis are explained. These concepts are epitaxial growth, magnetic anisotropies, the determination of MA constants from magnetization curves, the voltage control of magnetism (VCM), FMR, and the MOKE. In chapter 3 the experimental setups utilized in the sample preparation, magnetic characterization and the measurement of the VCMA are described. In chapter 4, 5 and 6 the sample preparation, the magnetic properties and the VCMA in MgO/Fe/Au-, MgO/Fe/Cr- and MgO/Co/Fe/Au-based multilayer structures are discussed, respectively. For all three multilayer structures the epitaxial growth is analyzed by reflection high energy electron diffraction (RHEED). The magnetic film thickness of the MgO/Fe/Au-, MgO/Fe/Cr- and MgO/Co/Fe/Au-based multilayer structures ranges from 0 nm to 1 nm, 0.44 nm to 1.25 nm and 0.66 nm to 0.9 nm, respectively. A basic magnetic characterization of all multilayer structures is conducted by analyzing of the out-of-plane magnetization curves as a function of the magnetic layer thickness. The VCMA coefficient in the MgO/Fe/Cr and MgO/Co/Fe/Au samples is measured by the modulation technique in a device with a magnetic layer thickness of 0.67 nm and 0.71 nm, respectively. An extended investigation of the magnetic properties and the VCMA of the MgO/Fe/Au-based sample is conducted. Both in- and out-of-plane magnetization curves are analyzed over the whole magnetic layer thickness range. Furthermore the thickness dependence of all MA constants and the g-factor are extracted from the angular- and frequency-dependent FMR measurements. The VCMA is investigated as a function of the gating time, the gate voltage, and the Fe thickness in a static fashion and by the modulation technique. Furthermore the voltage induced change in the FMR position is measured. In chapter 7 the main results and conclusions obtained in this thesis are summarized.

Appendix A contains informations on the homebuilt resistive thermal evaporators (RTE) and electron-beam evaporators developed and built in the frame of this thesis. In appendix B a detailed description of the microfabrication of the devices used to measure the VCMA with the modulation technique and the (voltage dependent) FMR in the TR-MOKE setup is given.

2. Theoretical background

In the following the theoretical concepts used throughout this thesis are laid out. The chapter is organized in six parts. In part one the basic concepts and the terminology used to describe the epitaxial growth is introduced. Part two discusses the magnetic anisotropy (MA) of thin films. Part three is devoted to the voltage control of magnetism (VCM). In part four the dynamics of thin films are discussed where in particular the ferromagnetic resonance (FMR) condition is derived. Finally, in part six the magneto optic Kerr effect (MOKE) is discussed.

2.1. Epitaxial growth

Epitaxial growth describes the orderly arrangement of a material upon a crystalline surface. The term homoepitaxy is used whenever the deposited and substrate layer are of the same material. Otherwise the growth is described as heteroepitaxy. Pseudomorphic growth occurs if the epitaxial layer completely adapts the crystal structure of the substrate template.

An important criterion for epitaxial growth is the lattice missmatch η which is written as [65]

$$\eta = \frac{a_\mathrm{s} - a_\mathrm{e}}{a_\mathrm{e}}, \tag{2.1}$$

where $a_\mathrm{e,s}$ are the lattice constants of the epitaxial and substrate layer, respectively. Positive η corresponds to tensile strain and negative η corresponds to compressive strain. A small η is a prerequisite for good epitaxial growth. Quite often a small η is achieved by rotation of the epitaxial layer unit cell by 45° with respect to the substrate crystal structure. For example, the epitaxial relation of a Fe film prepared onto a Au layer with (001) surface orientation is Fe[110]$\|$Au[100] where η is only 0.5 % (on the contrary, η would be as large as 30 % for the epitaxial relation: Fe[100]$\|$Au[100]).

A thermodynamic description of epitaxy is given by Bauer et al. [66, 67]. Within this model three different growth modes are predicted. Which of this modes occurs is solely determined by the relation of the surface free energy of the substrate layer (γ_s), the epitaxial (γ_a) layer and the sample interface (γ_i): In case where $\gamma_\mathrm{s} < \gamma_\mathrm{e} + \gamma_\mathrm{i}$ a three dimensional (3D), so called Volmer-Weber growth is predicted. Here the epitaxial layer does not moisten the substrate layer and thus forms 3D islands upon deposition. The layer-by-layer (LBL), or

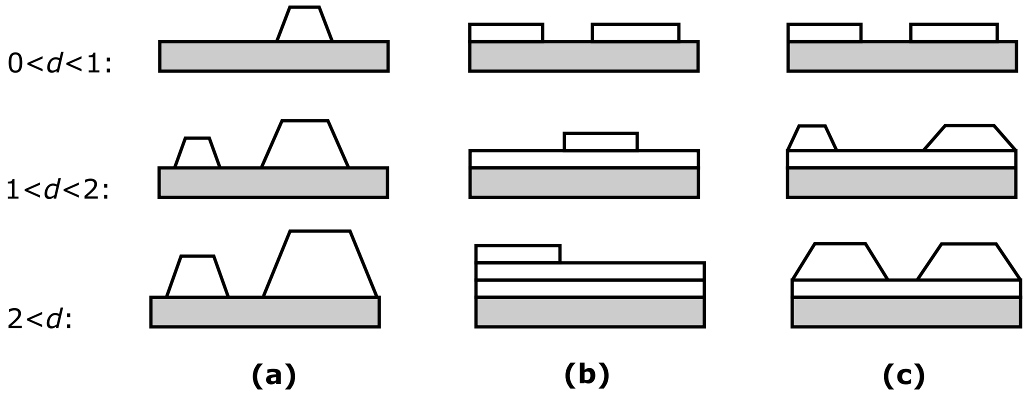

Figure 2.1.: Epitaxial growth modes predicted in dependence of the relation between γ_s, γ_e and γ_i, according to Bauer et al. [66, 67]. Here d is the film thickness of the growing layer. If (a) $\gamma_\mathrm{s} < \gamma_\mathrm{e} + \gamma_\mathrm{i}$, the 3D, or Volmer-Weber growth mode, if (b) $\gamma_\mathrm{s} > \gamma_\mathrm{e} + \gamma_\mathrm{i}$ the LBL, or Frank-van der Merwe, growth mode and if (c) γ_i increases with d, the Stranski–Krastanov growth mode is predicted, respectively.

Frank-van der Merwe growth mode is predicted for the case $\gamma_\mathrm{s} > \gamma_\mathrm{e} + \gamma_\mathrm{i}$. Here a new layer does not start to form until the actual growing layer is completed and thus a perfectly flat film is prepared. In the experiment this is usually the most anticipated mode. In most practical cases however, γ_i will increase with film thickness, for example due to formation of strain in the epitaxial layer. As a consequence a transition from the LBL to the 3D mode occurs. This is called the Stranski-Krastanov growth mode. A schematic representation of the three described growth modes is shown in the figures 2.1(a), (b) and (c), respectively.

Relating the epitaxy to the relation between γ_s, γ_e and γ_i is only justified if thermodynamic equilibrium conditions are fulfilled. These conditions are full filled for very low deposition rates and/or high substrate temperature. Often however, these requirements are not satisfied. In this case the thermodynamic model has to be replaced/complemented by a kinematic description of the epitaxial growth. In a kinematic picture an atom arriving at the surface of a growing layer may undergo several events: the atom can diffuse along the surface, diffuse up or down terraces, bind onto a special site like surface steps, hit other atoms and nucleate, interdiffuse into the substrate, or re-evaporate. A schematic representation of this events is shown in figure 2.2 (in accordance with reference [68]). In the following a qualitative prediction of the epitaxial growth mode in dependence of the surface temperature, the deposition rate and the substrate surface step density is given (in accordance with reference [69, 70]).

As a starting point a surface with high step density, high surface temperature and a low arrival rate of deposited atoms is assumed. In this case the arriving atoms can diffuse over long distances on the substrate surface and easily move up or down surface steps. Due to the low density of arriving atoms, they are more likely bound to a surface step than to nucleate upon a terrace. Thus the growth proceeds in the so-called step flow mode, where a new layer is formed by continuously propagating the steps along the sample surface. The

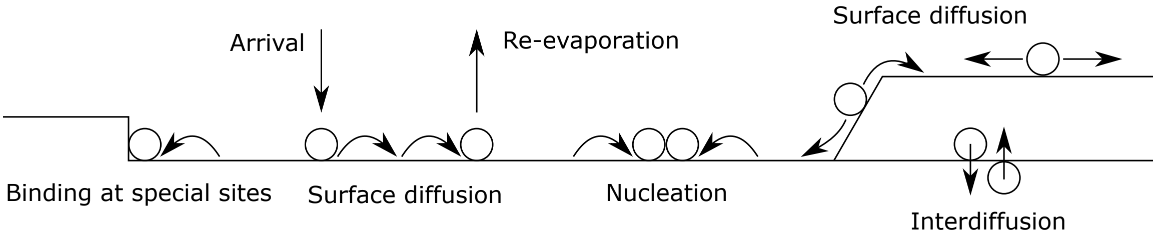

Figure 2.2.: Events an atom can undergo on arrival onto a substrate during epitaxial growth. Figure according to reference [68].

step-flow mode leads to a high quality epitaxial layer, where the roughness stays constant during growth and is mainly determined by the roughness of the substrate layer.

Next, the growth conditions are changed by lowering the surface temperature and increasing the deposition (and thus arrival) rate of atoms. Furthermore the substrate surface shall have a lower step density. In this case the nucleation probability of the arriving atoms is strongly increased which allows them to nucleate on terraces. However, as the atoms still have enough energy to easily move up and down surface steps, a growing layer more likely is to be completed before a new one is formed. As a result the LBL growth mode occurs, where the roughness oscillates between perfectly flat and half filled layer.

Further decreasing of the substrate surface temperature reduces the ability of atoms to freely move up and down surface steps. Thus more nucleation sites are created on growing, not fully filled layers. As a result the average film roughness slowly increases with deposition time. The complete transition from the LBL to the 3D growth is expected by further decreasing the substrate surface temperature to the point where it is impossible for atoms to move up or down surface steps. As a consequence the atoms will stay on the terrace where they arrive. There they will either nucleate or bind to an already formed nucleation site. Under these conditions 3D islands are formed and the film roughness strongly increases with deposition time.

2.2. Magnetic anisotropy in ultrathin films

The MA is defined as the energy per sample volume, that is needed to rotate the magnetization from the easy axis towards the hard axis. The most simple MA, in terms of its mathematical description, is the MA of uniaxial symmetry, where only one easy axis exists. The leading term of the uniaxial MA is written as

$$E_{\mathrm{MA}} = -K\cos^2\theta, \tag{2.2}$$

where K is the MA constant and θ is the angle between the magnetization direction and the symmetry axis of the system. According to the definition used here, the symmetry axis is an easy axis if $K > 0$ and a hard axis if $K < 0$. The uniaxial MA described by

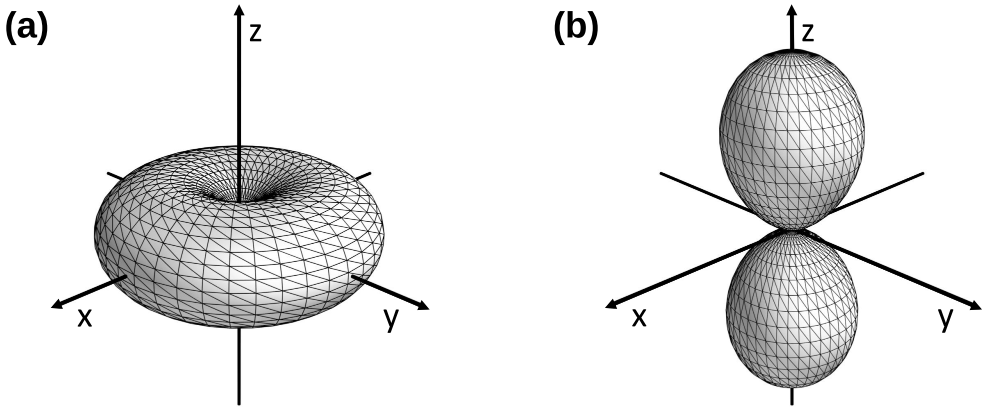

Figure 2.3.: Three-dimensional surface plot of the uniaxial MA: $E_{\mathrm{MA}} = -K\cos^2\theta$. The angle θ is measured relatively to the z-axis of the Cartesian coordinate system. Figure (a) shows the plot for positive K. An easy axis is formed along the z-direction. Figure (b) shows the plot for negative K. Here on the contrary, the z-direction defines the hard axis. In this case no easy axis exists. Instead an easy plane orthogonal to the hard direction is induced. Please note that in figure (a) a constant term has been added to E_{MA} for visual clarity.

equation 2.2 is illustrated in figure 2.3(a) and (b) through the three-dimensional surface plots for $K > 0$ and $K < 0$, respectively. If $K < 0$, no easy axis exists. In this case, an easy plane is induced orthogonal to the hard axis. Often the leading term of the MA is sufficient to adequately describe experimental results and only rarely higher order terms have to be taken into account [71].

Two sources of MA exist, the magnetic dipole interaction and the spin-orbit coupling (SOC). The magnetic dipole interaction mainly manifests itself in a dependence of the free energy on the relative orientation between the sample magnetization and sample shape, which is called magnetic shape anisotropy (MSA). The MSA is in most cases the strongest MA contribution and forces the magnetization to align parallel to the sample surface plane in thin films. All other MA contributions can be traced back to the SOC. In itinerant magnets, the SOC couples the free energy of the system to the relative orientation between the spin moment and the crystal lattice. The resulting MA is called the magnetocrystalline anisotropy (MCA). In principle, the magnetic dipole interaction can also lead to a MCA. However, for elements of cubic structure like Fe and Ni, it can be shown that this interaction cancels when it is summed over the hole crystal. Here we always refer to the SOC induced MCA, as first described by van-Vleck in 1937 [72]. At the interface or the surface of a sample, this MCA is strongly altered due to the lateral symmetry breaking. For ultrathin layers the interface MCA can dominate and it may even overcome the MSA leading to the perpendicular magnetic anisotropy (PMA). In this case the magnetization is oriented along the sample surface normal at equilibrium. As the MCA is determined by the crystal lattice, any lattice distortion will have an impact on the MCA. This effect is described by the magnetoelastic anisotropy (MEA). The MEA can be especially important in pseudomorphically grown thin films, where an η of several percent is a typical value. Finally, unexpected in-plane MAs are often observed in ultrathin magnetic layers. The uniaxial in-plane MA usually is related to a deviation of the magnetic layer structure from the ideal case of a perfectly flat film.

In the following subsections, more detailed descriptions of the MSA, MCA and MEA are presented. Furthermore, the origin of the unexpected in-plane anisotropies found in thin epitaxial films is specified. The purpose of this presentation is the discussion of the different MA contributions relevant for ultrathin epitaxial films. Finally, an overview of theoretical and experimental studies on the PMA in various material systems relevant to this work is presented.

2.2.1. Magnetic shape anisotropy

The MSA is usually deduced in the framework of a magnetic continuum approach. The demagnetizing field $\vec{H}_\mathrm{d}$ of a magnetic sample is written as [73]

$$\vec{H}_\mathrm{d} = \mathcal{D}\vec{M}, \tag{2.3}$$

where $\vec{M}$ is the magnetization and $\mathcal{D}$ is the demagnetizing tensor, which is solely determined by the shape of the sample. The diagonal tensor elements of $\mathcal{D}$ are called demagnetizing factors. It can be shown that for thin films, the only non-vanishing demagnetizing factor is the one along the sample surface normal ($\mathcal{D}_\mathrm{zz}$), where $\mathcal{D}_\mathrm{zz} = 1$ [73]. The magnetostatic energy density of a ferromagnetic body subject to its own demagnetizing field, can be written as [73]

$$E_\mathrm{d} = -\frac{\mu_0}{2V}\int_V \vec{M}\vec{H}_\mathrm{d} dV, \tag{2.4}$$

where μ_0 is the vacuum permeability and V is the volume of the magnetic sample. Equations 2.3 and 2.4 and the demagnetizing factors for thin films lead to the conventional expression used to described the MSA of thin film systems, which can be written as

$$E_\mathrm{MSA} = \frac{1}{2}\mu_0 M_\mathrm{S}^2 \cos^2\theta = -K_\mathrm{MSA}\cos^2\theta, \tag{2.5}$$

where K_MSA is the MSA constant, M_S is the saturation magnetization and θ the angle between the sample surface normal and the magnetization. We can see from equation 2.5 that the MSA forces the magnetization to lie in the sample plane. The K_MSA values for films of Fe, Co and Ni are $-1.84\,\mathrm{MJ/m^3}$, $-1.3\,\mathrm{MJ/m^3}$ and $-0.15\,\mathrm{MJ/m^3}$, respectively [73]. The MSA is usually the main MA which needs to be overcome in order to induce PMA. Film roughness induces a magnetic stray field even for the in-plane orientation of the magnetization and thus reduces the MSA.

For ultrathin films, a treatment based on discrete magnetic dipoles shows that the demagnetizing field slightly decreases towards the sample surface. As a result, D_{zz} has to be corrected by a thickness dependent term [74–77]. For films of body centered cubic (bcc) structure with a (001) surface one can write [78]

$$\mathcal{D}_{\mathrm{zz}} = 1 - \frac{0.425}{N}, \tag{2.6}$$

where N denotes the number of monolayers. For Fe, this equation leads to a pseudo-interface MA contribution of $0.06\,\mathrm{mJ/m^2}$ which amounts to about 10 % of the interface MA contributions typically observed.

2.2.2. Magnetocrystalline anisotropy

The following discussion has three parts. Part one and two describe the MCA of cubic and tetragonal systems, respectively. In part three the interface MCA is discussed, which can be the dominating MA contribution in ultrathin films.

MCA in cubic systems

The MCA can be written as a series expansion of a set of orthonormal spherical harmonics, reflecting the crystal structure of the specimen [73]:

$$E_{\mathrm{MCA}} = \sum \kappa_l^m A_l^m Y_l^m(\theta, \phi). \tag{2.7}$$

Here, A_l^m are the crystal-field and κ_l^m the magnetic anisotropy coefficients. ϕ and θ are the azimuthal and polar angles. For a system of cubic structure, the first terms of the expansion can be written as:

$$\begin{aligned} E^{\mathrm{c}}_{\mathrm{MCA}} = \kappa_0 + \kappa_4^4\Big(\alpha_{\mathrm{x}}^2\alpha_{\mathrm{y}}^2 + \alpha_{\mathrm{y}}^2\alpha_{\mathrm{z}}^2 + \alpha_{\mathrm{x}}^2\alpha_{\mathrm{z}}^2 - \frac{1}{5}\Big) + \\ \kappa_6^4\Big(\alpha_{\mathrm{x}}^2\alpha_{\mathrm{y}}^2\alpha_{\mathrm{z}}^2 - \frac{1}{11}\Big(\alpha_{\mathrm{x}}^2\alpha_{\mathrm{y}}^2 + \alpha_{\mathrm{y}}^2\alpha_{\mathrm{z}}^2 + \alpha_{\mathrm{x}}^2\alpha_{\mathrm{z}}^2 - \frac{1}{5}\Big) - \frac{1}{105}\Big) + ... \end{aligned} \tag{2.8}$$

Here, $\alpha_{\mathrm{x,y,z}}$ are the direction cosines with respect to the $\langle 100\rangle$ crystal cube axes. No uniaxial anisotropy term is allowed because of the geometrical relation $\alpha_{\mathrm{x}}^2+\alpha_{\mathrm{y}}^2+\alpha_{\mathrm{z}}^2 = 1$. If we neglect the constant contribution and sum up the terms of equation 2.8, we can write

$$E^{\mathrm{c}}_{\mathrm{MCA}} = K_4\Big(\alpha_{\mathrm{x}}^2\alpha_{\mathrm{y}}^2 + \alpha_{\mathrm{y}}^2\alpha_{\mathrm{z}}^2 + \alpha_{\mathrm{x}}^2\alpha_{\mathrm{z}}^2\Big) + K_6\Big(\alpha_{\mathrm{x}}^2\alpha_{\mathrm{y}}^2\alpha_{\mathrm{z}}^2\Big). \tag{2.9}$$

This is the expression commonly used to describe the MCA of magnetic materials with cubic crystal structure. K_4 and K_6 are the MCA constants of fourth and sixth order. K_4 is also referred to as the biaxial MA constant. By making use of the relation

$$1 - 2(\alpha_{\mathrm{x}}^2\alpha_{\mathrm{y}}^2 + \alpha_{\mathrm{y}}^2\alpha_{\mathrm{z}}^2 + \alpha_{\mathrm{x}}^2\alpha_{\mathrm{z}}^2) = \alpha_{\mathrm{x}}^4 + \alpha_{\mathrm{y}}^4 + \alpha_{\mathrm{z}}^4, \tag{2.10}$$

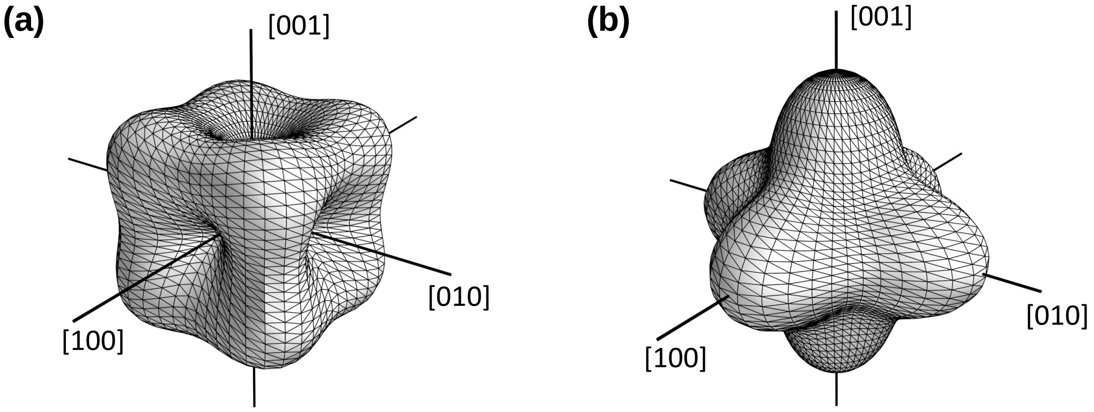

Figure 2.4.: Three-dimensional surface plot of the cubic MCA energy density $E^{\mathrm{c}}_{\mathrm{MCA}} = -K_4/2(\alpha_{\mathrm{x}}^4 + \alpha_{\mathrm{y}}^4 + \alpha_{\mathrm{z}}^4)$ for (a) $K_4 > 0$ and (b) $K_4 < 0$. These parameters correspond to the MCA of Fe and Ni. Fe has three easy axes which are oriented along the $\langle 100 \rangle$ cube axes. On the contrary in Ni, the cube axes are hard directions. Here, the easy axes are oriented along the four $\langle 111 \rangle$ diagonals.

and equation 2.9, where one neglects the sixth order term, one can write

$$E^{\mathrm{c}}_{\mathrm{MCA}} = -\frac{K_4}{2}(\alpha_{\mathrm{x}}^4 + \alpha_{\mathrm{y}}^4 + \alpha_{\mathrm{z}}^4). \tag{2.11}$$

This is a further expression commonly used to describe the MCA of cubic systems, which intuitively reflects the symmetry of the cubic system. In figure 2.4(a) and (b), the three dimensional surface of $E^{\mathrm{c}}_{\mathrm{MCA}}$ described by equation 2.11 is plotted for positive and negative K_4. These plots reflect the MCA landscape of Fe and Ni, where K_4 is $48\,\mathrm{kJ/m^3}$ and $-5\,\mathrm{kJ/m^3}$, respectively.

MCA in tetragonal systems

Thin epitaxial films are almost always grown in a pseudomorphic manner, where an η of several percent is not uncommon. In order to minimize the resulting film stress τ, an elongation or contraction along the direction perpendicular to the film surface occurs. Typically, materials that exhibit cubic structures in the bulk tend to have tetragonal crystal structures when grown as thin films. In this case, the biaxial out-of-plane MCA constant $K_4^{\perp}$ is different from the biaxial in-plane MCA constant $K_4^{\|}$. Furthermore, a uniaxial out-of-plane MCA contribution is allowed, which is forbidden in strictly cubic systems (see section 2.2.2). The MCA of tetragonal systems can be written as [79]:

$$E^{\mathrm{t}}_{\mathrm{MCA}} = -\frac{K_4^{\|}}{2}(\alpha_{\mathrm{x}}^4 + \alpha_{\mathrm{y}}^4) - \frac{K_4^{\perp}}{2}\alpha_{\mathrm{z}}^4 - K_2^{\perp}\alpha_{\mathrm{z}}^2. \tag{2.12}$$

Here $K_2^{\perp}$ is the uniaxial out-of-plane MCA constant. For $K_4^{\|} = K_4^{\perp}$ and $K_2^{\perp} = 0$, one recovers the MCA of cubic systems.

Interface MCA

The interface MCA[1] refers to the modified MCA at the interface of the sample and is caused by the lateral symmetry breaking. Please note that in the following discussion, the interface MCA will always refer to the uniaxial out-of-plane interface MCA. Even though an interface contribution to the biaxial [77, 80–82] and uniaxial [83] in-plane MCA has been observed in epitaxial material systems of tetragonal symmetry, the uniaxial out-of-plane interface MCA is far more studied. This contribution can reach large values, even overcome the MSA and thereby induce the PMA in ultrathin films. The interface MCA is not restricted to tetragonal systems, as it is solely determined by the symmetry breaking at the sample interface.

The first theoretical prediction of an interface MCA promoting PMA was published in 1954 by Néel [84]. Néel's calculations are based on a pair interaction model, assuming localized magnetic moments where SOC is not included. Even though this approach is fundamentally incorrect at describing itinerant materials, Néel's work contributed significantly to the understanding of interface MCA and is often cited in this context. Prototypical systems exhibiting strong interface MCA inducing PMA are Co/Pd or Co/Pt multilayers [85]. The interface MCA in these material systems is related to the d-d orbital hybridization induced charge transfer at the interface and the strong SOC of the non-magnetic heavy metal [86–89]. Thus, a heavy metal layer with large SOC was considered indispensable for PMA. However, PMA was also observed in $\mathrm{MO_x}$/Fe(Co) (M = Mg, Al, Cr, Ta etc.; x = degree of oxidation) samples, despite weak SOC [7, 90–93]. The archetype of such system is MgO/Fe(CoB). It is known by theoretical [94] and experimental studies [95, 96] that the oxygen atoms align on top of the Fe atoms during epitaxial growth. The interface MCA is then mainly determined by the oxygen 2p and Fe 3d orbital hybridization [57, 58, 97, 98]. Consequently the magnitude of the interface MCA strongly depends on the degree of Fe oxidation [57, 58, 97, 98]. However, it also has been shown that an oxygen excess at the Fe/MgO interface results in a negative interface MCA supporting the in-plane magnetization [57, 58, 98]. Thus, the exact growth conditions crucially determine the interface MCA of epitaxially grown MgO/Fe(CoB) systems.

2.2.3. Magnetoelastic anisotropy

The MEA describes the change of a samples MA with respect to an elastic deformation. Changes of the samples dimension with respect to the magnetization direction are called magnetostriction. Two contributions to the free energy, namely the elastic energy E_e and the MEA, have to be accounted for in order to fully describe the relation between the elastic

---

[1] Here, the term *interface* MCA is adopted, because in most cases the samples investigated experimentally are bound by two layers, forming the respective interfaces. Thus, the term *surface* MCA, which is sometimes used in the literature, in most cases is misleading.

and magnetic properties of a sample. For cubic systems they can be written as [65]

$$E_{\mathrm{e}} = \frac{1}{2}c_{11}(\epsilon_1^2 + \epsilon_2^2 + \epsilon_3^2) + c_{12}(\epsilon_1\epsilon_2 + \epsilon_2\epsilon_3 + \epsilon_3\epsilon_1) + \frac{1}{2}c_{44}(\epsilon_4^2 + \epsilon_5^2 + \epsilon_6^2), \tag{2.13}$$

and

$$E_{\mathrm{MEA}} = B_1(\epsilon_1\alpha_1^2 + \epsilon_2\alpha_2^2 + \epsilon_3\alpha_3^2) + B_2(\epsilon_4\alpha_2\alpha_3 + \epsilon_5\alpha_3\alpha_1 + \epsilon_6\alpha_1\alpha_2), \tag{2.14}$$

where c_{ij} are the elastic stiffness tensor components, ϵ_i the strain tensor components (here written in the contracted *Voigt* notation [65]), $B_{1,2}$ the magnetoelastic coefficients and α_i the direction cosines of the magnetization with respect to the cubic axes. The magnetostrictive strain λ is defined as the relative length change with respect to the magnetization orientation. By minimizing the total magnetoelastic free energy (the sum of equations 2.13 and 2.14) with respect to ϵ, one can derive

$$\lambda_{100} = -\frac{2}{3}\frac{B_1}{c_{11} - c_{12}}, \tag{2.15}$$

where λ_{100} is defined as the relative change in length for the magnetization aligned between the [100] and [111] direction, assuming an ideal demagnetized state as starting point. For bulk Fe, λ_{100} is 2.4×10^{-5}. The positive sign of λ_{100} means that Fe will expand if magnetized along the cubic axes. B_1 calculated according to equation 2.15 is $3.4\,\mathrm{MJ/m^3}$. The resulting MEA ($\sim \lambda B$) is approximately two orders of magnitude smaller than the MCA.

The MEA changes quite dramatically for thin films. It is experimentally well confirmed, that B_{i} (the subscript i stands for the different magnetoelastic coefficients) measured in thin films differs significantly from the respective bulk values [99–106]. It was shown that PMA can even be induced by the MEA in thin films [102]. In thin epitaxial films, only the out-of-plane strain ϵ_3 can be considered variable. The respective in-plane strain $\epsilon_{1,2}$ has to be considered constant during magnetization reversal, as the film lattice is strongly fixed to the substrate. As a consequence, the concept of λ fails and equation 2.15 is no longer valid. Magnetoelastic effects in thin films are therefore treated in terms of film stress τ, which occurs during magnetization reversal (magnetostrictive stress). Thin films grown in a pseudomorphic manner are usually strongly strained, due to the η between film and substrate. For an η on the order of a few percent, which is quite common in epitaxial growth, τ reaches several GPa, exceeding the normal yield strength of steel by an order of magnitude. Eventually this τ is relieved at a certain critical film thickness d_{c} through the introduction of misfit dislocations. For example Fe grown epitaxially onto an Ir(100) substrate, where η is $5\,\%$, the end of pseudomorphic growth was measured to occur at 10 ML by means of cantilever crystal curvature technique [105]. The determination of d_{c} and the thickness dependence of the intrinsic film ϵ is a non-trivial task, which makes it very difficult to properly include the MEA in the discussion of thin film MA. An approximation for the d-dependence of ϵ beyond d_{c}, that is often used in the literature [100, 107], was derived by Bruno and Chapert [108]:

$$\epsilon(d) = \eta \frac{d_\mathrm{c}}{d}. \tag{2.16}$$

This equation leads to a MEA ($\sim B_\mathrm{i}\epsilon$) which appears as interface contribution, even though it clearly originates in the volume of the sample. However, several experimental results show that ϵ decays weaker than suggested by equation 2.16 and can be considerably large, even for large d [103, 109]. In order to better describe the MA dependence on d found in experiments, a d-dependent effective magnetoelastic coupling coefficient $B_\mathrm{i}^\mathrm{eff}(d)$ has been proposed [99, 101, 102, 106], which in its simplest form is written as

$$B_\mathrm{i}^\mathrm{eff}(d) = B_\mathrm{i}^\mathrm{v} + B_\mathrm{i}^\mathrm{i}/d. \tag{2.17}$$

Here, B_i^v and B_i^i are the volume and interface magnetoelastic coefficients, respectively. The appearance of an interface MEA contribution is motivated in the same way as the interface MCA introduced in 2.2.2. However, this approach is controversially discussed in the literature. It has been convincingly shown that B_i^eff in epitaxial thin films is more dependent on the intrinsic ϵ than on d [103–105]. The publications show that films with the same ϵ but different d had the same B_i^eff. This result contradicts the explanation of the thin film MEA in terms of an interface MEA contribution. The dependence of B_i^eff on ϵ can be well-fitted by a linear relation [104, 105]:

$$B_\mathrm{i}^\mathrm{eff}(\epsilon) = B_\mathrm{i} + D_\mathrm{i}\epsilon_\mathrm{i}, \tag{2.18}$$

where D_i is the first order expansion coefficient. These observations show that the dependence of B_i on ϵ plays a decisive role in explaining the MEA in thin epitaxial films. Thus the absolute magnitude of the thin film MEA is very sensitive to growth conditions, film thickness, and layer stacking.

2.2.4. Uniaxial in-plane ansitropy

In ultrathin magnetic films, often an unexpected uniaxial in-plane MA is observed. This MA usually is caused by geometrical factors such as the stepped surface of a vicinal substrate [110], a directed roughness in the magnetic layer induced by oblique-incidence deposition [111], or a ripple-like structure of the magnetic layer induced by post growth Ar^+-ion sputtering under oblique incidence [112]. Furthermore it is shown that a unidirectional orientation of dangling bonds at the substrate surface can lead to a uniaxial MA in the ferromagnetic layer [113]. The uniaxial in-plane MA in most cases is adequately described by the leading term

$$E_\mathrm{u}^{\|} = -K_\mathrm{u}^{\|} \frac{(\hat{n}\vec{M})^2}{M_\mathrm{s}^2}, \tag{2.19}$$

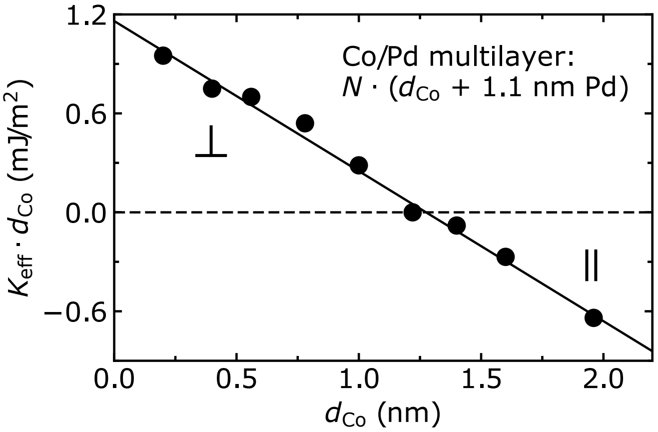

Figure 2.5.: $K_{\mathrm{eff}} \cdot d_{\mathrm{Co}}$ vs. d_{Co} plot (d_{Co} is the Co layer thickness) for a Co/Pd multilayer. At a d_{Co} of 1.3 nm, a transition from in-plane to out-of-plane orientation of magnetization with respect to the sample surface takes place. Data taken from Broeder et al. [85].

where $K_{\mathrm{u}}^{||}$ is the uniaxial in-plane MA constant, $\vec{M}$ is the magnetization vector with saturation magnetization M_{s} and $\hat{n}$ is a normal vector pointing along the easy axis for $K_{\mathrm{u}}^{||} > 0$.

In case of a thin film of cubic or tetragonal structure, the uniaxial in-plane MA usually is written as

$$E_{\mathrm{u}}^{||} = -K_{\mathrm{u}}^{||} \cos^2(\phi_M - \phi_{\mathrm{u}}), \tag{2.20}$$

where ϕ_M is the azimuthal angle of the magnetization vector and the [100] crystal axis and ϕ_{u} is the angle between the easy axis and the [100] crystal axis.

2.2.5. Perpendicular magnetic anisotropy

Samples which are said to possess PMA have their magnetization aligned along the sample surface normal, even without applied external field. This alignment is rather surprising in view of the large demagnetizing field that has to be overcome. The out-off-plane MA of samples with PMA can usually be described quite well by a uniaxial term:

$$E^{\perp} = -K_{\mathrm{eff}} \cos^2\theta, \tag{2.21}$$

where K_{eff} is the effective out-of-plane MA constant and θ is the angle between the sample surface normal and the magnetization. K_{eff} is called *effective* as it sums up the contributions arising from MSA, MCA and MEA. Experimentally a plot of $K_{\mathrm{eff}} \cdot d$ versus d, where d is the magnetic layer thickness, usually reveals a linear relationship. Eventually, $K_{\mathrm{eff}} \cdot d$ versus d changes its sign below a certain thickness, the spin reorientation thickness d_{SRT}, which means that PMA is induced in the sample. Figure 2.5 shows an example of such a plot for Co/Pd multilayers, taken from a publication of Broeder et al. [85]. In a phenomenological manner, K_{eff} is usually separated into a volume anisotropy constant K_{v} and an interface anisotropy constant K_i according to:

$$K_\mathrm{eff} = K_\mathrm{v} + K_\mathrm{i}/d. \tag{2.22}$$

Then the $K_\mathrm{eff} \cdot d$ versus d plot is used to extract K_v and K_i. For the exemplary plot shown in figure 2.5, we obtain a K_v of $-0.91\,\mathrm{MJ/m^3}$ from the slope of the curve and a K_i of $1.19\,\mathrm{mJ/m^2}$ from the y-axes intercept. Below the d_SRT of 1.27 nm , the negative K_i can overcome the positive K_v and induce the PMA in the Co7Pd multilayer.

Table 2.1 summarises K_v, K_i and d_SRT evaluated for different material systems. However, one should be careful taking K_i and K_v literally. As shown in the previous sections, MSA, MCA and MEA can contribute to both K_i and K_v. The main contribution to K_v is usually the MSA. However, both the MCA and the MEA can contribute to K_v. The main contribution to K_i is usually the interface MCA. However, both MSA and MEA can lead to a (pseudo) K_i term. It has even been shown that in some cases the MEA can be the main factor determining the PMA. K_i and K_v written in table 2.1 differ significantly even for nominally identical systems. This variation shows the strong dependence of the thin film MA on the exact growth conditions, which may be hard to reproduce experimentally.

2.3. Magnetic anisotropy extraction from magnetization curves

The MA can be deduced from the area enclosed by the magnetization curves measured where the magnetic field is aligned along the easy and hard axes of the system, respectively [50]. This procedure is called the area method and can be understood from magnetostatic principle which states that the work needed to change the magnetization of a sample by $\mathrm{d}M$ is given by $\mu_0 H \mathrm{d}M$ [107].

In the following the area method is explained by extracting K_eff from the in- and out-of-plane magnetization curves of an 0.5 nm thin epitaxial Fe film, shown in figure 1.6. The curves are measured by means of MOKE and are normalized to the value one at saturation. M' stands symbolically for the in- and out-of-plane[2] magnetization component. The in-plane curve is measured along the Fe[100] direction and clearly shows the easy axes of the system. The out-of-plane curve on the other hand shows the hard axes of the system. With respect the area method one can write [107]

$$K_\mathrm{eff} = -\mu_0 M_\mathrm{s} \int_0^1 (H^\perp \mathrm{d}z^\perp - H^\parallel \mathrm{d}z^\parallel), \tag{2.23}$$

where $dz^{\perp,\parallel} = dM^{\perp,\parallel}/M_\mathrm{s}$ and $H^{\perp,\parallel} = H^{\perp,\parallel}(M^{\perp,\parallel}/M_\mathrm{s})$. The symbols $\perp$ and $\parallel$ indicate the in- and out-of-plane orientation of the field. The hysteresis observed here in the in-plane magnetization curve does not allow to define a distinct function of $H^\parallel$ on $M^\parallel/M_\mathrm{s}$. Practically one circumvents this problem by averaging this part of the curve [107]. Here

---

[2] The out-of-plane orientation presumes that the field is oriented perpendicular to the sample surface.

Layer structure	K_v (MJ/m^3)	K_i (mJ/m^2)	d_SRT (nm)	PMA	Reference
MgO/CoFeB/W	-1.59	1.19	0.75	✓	[41]
MgO/CoFeB/Ir	-1.1	1.9	1.7	✓	[43]
MgO/CoFeB/Ta	-0.993	1.39	1.40	✓	[5]
MgO/FeCo/Au		0.94		✓	[9]
MgO/FeCo/Au		0.82		✓	[9]
MgO/FeCo/Au	-1.12	0.65	0.58	✓	[7]
MgO/FePd/Pd	0.6	-1.0	1.7	✓	[11]
MgO/Fe/Cr	- 2.5	2.1	0.85	✓	[46]
MgO/Fe/Cr		2.01		✓	[3]
MgO/Fe/Cr		0.86		✓	[3]
MgO/Fe/Cr		2.01		✓	[1]
MgO/Fe/Cr		1.19		✓	[1]
MgO/Fe/Cr	-1.78	1.00	0.56	✓	[2]
MgO/Fe/V	-1.78	1.00	0.56	✓	[2]
MgO/Fe/Au	-1.414	0.58			[6]
Au/Fe/Au			0.3	✓	[114]
Ag/Fe/Ag		1.62			[81]
Au/Fe/Ag		1.28			[81]
Ag/Fe/Ag		1.27			[115]
UHV/Fe/Ag		1.60			[115]
Au/Fe/Ag		0.78			[115]
Ag/Fe (bulk)		0.79			[116]
Au/Fe (bulk)		0.54			[116]
UHV/Fe/Cu				✓	[117]
UHV/Fe/Ru				✓	[117]
UHV/Fe/Pd				✓	[117]
UHV/Fe/Au				✓	[117]
$(\mathrm{Co/Pd})_\mathrm{m}$	-0.91	1.48	1.63	✓	[85]
$(\mathrm{Co/Pd})_\mathrm{m}$	-0.91	1.16	1.27	✓	[85]
$(\mathrm{Co/Pt})_\mathrm{m}$	-0.7	1.16	1.66	✓	[85]
$(\mathrm{Co/Pt})_\mathrm{m}$	-1.0	1.00	1.0	✓	[85]
$(\mathrm{Co/Au})_\mathrm{m}$	-0.70	1.16	1.66	✓	[85]

Table 2.1.: Table of K_v, K_i and d_SRT (if given in the article), for a selection of different magnetic material systems. If PMA could be observed, the corresponding column is denoted with a check mark. The layer structure only includes the magnetic and the two adjacent materials. The layer on the left corresponds to the upper side of the sample. UHV means that the samples where not covered and measured in-situ. The subscript "m" denotes multilayer samples.

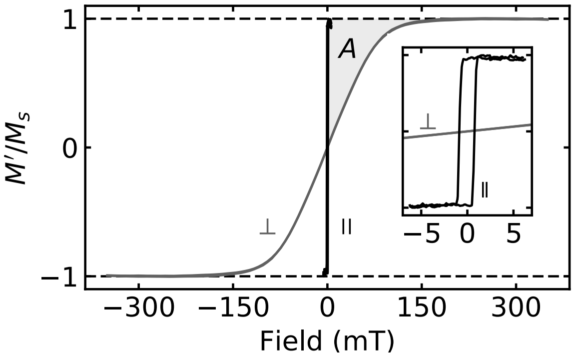

Figure 2.6.: Normalized in- and out-of-plane magnetization curves of a 0.5 nm thin Fe film measured by means of MOKE. The in-plane curve is measured with a magnetic field orientation along Fe[100] direction. The inset shows a magnified view of the curves. The MA of the film is directly related to the area A. Details on extracting the MA by the area method are described in the text.

averaging the hysteresis yields $H^{\parallel}(M^{\parallel}/M_\mathrm{s}) = 0$. Inserting this relation into equation 2.23 leads to

$$K_\mathrm{eff} = -\mu_0 M_\mathrm{s} \int_0^1 H^{\perp} \mathrm{d}z^{\perp} = -\mu_0 M_\mathrm{s} A, \tag{2.24}$$

where A is the area between the out-of-plane magnetization curve and the y-axis of the coordinate system (gray area in figure 2.6). Inserting A determined from the out-of-plane magnetization curve shown in figure 2.6 and bulk Fe M_s (1720 kA/m [73]) into equation 2.24, one yields a K_eff of $-95\,\mathrm{kJ/m^3}$.

2.4. Voltage control of magnetism

The first report of the VCM dates back to 2000. In this year Ohno et al. published their experiment on the voltage control of $\mathrm{M_s}$ and the Curie temperature in the magnetic semiconductor (In,Mn)As [118]. This experimental finding triggered an immense effort to explore and conquer this new exciting effect. A successive milestone was reported in 2007 where Weisheit et al. showed that the coercivity of an FePt layer could be controlled in a reversible manner through ionic liquid gating [119]. This experiment proves that VCM in ferromagnetic metals is possible, which was long believed to be hard to achieve due to the short screening length [120].

The VCM is a very active field of research. Figure 2.7 shows the publications per year on the topic from 2006 to 2015 [121]. The research field is usually classified with respect to the material of the magnetic layer in which the VCM is explored: ferromagnetic metals (e.g., Fe, Ni, Co, FeCo, CoFeB), semiconductors (e.g. (In,Mn)As, (Ga,Mn)As) and complex oxides (e.g. LSMO). A further classification is then conducted with respect to the bilayer structure the magnetic layer is embedded in. For metals the different bilayer structures are: ferroelectric/ferromagnet metal bilayers (e.g. BTO/Ni, BFO/CoFeB), ox-

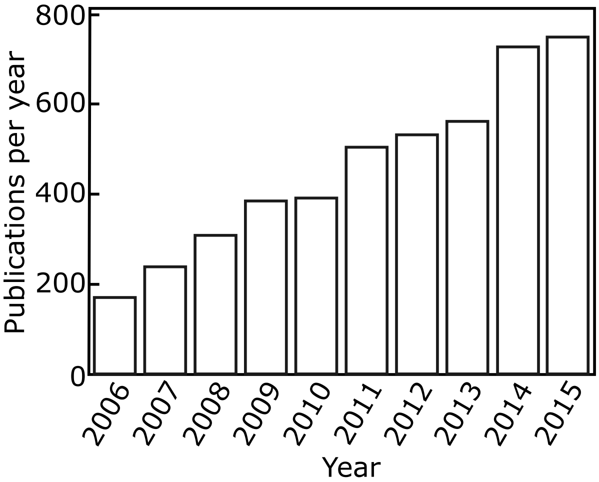

Figure 2.7.: Publications per year on the VCM, taken from reference [121].

ide/ferromagnet metal bilayers (e.g. MgO/CoFeB) and oxide ion conductor/ferromagnet metal bilayers (e.g. GdO/CoFeB). The properties which are controlled in these systems are: M_s, the curie temperature and the MA. In each material system the effect is usually linked to one main physical mechanism: strain alteration (ferroelectric/ferromagnet metal bilayers), charge accumulation at the bilayer interface (oxide bilayers/ferromagnet metal) and interface chemistry alteration (ion conductor/ferromagnetic metal). A very recent review on the VCM in ferromagnetic metals, semiconductors and oxides, embedded in various bilayer structures, is given by Song et al. [121].

Voltage control of magnetic anisotropy in MgO/Fe(CoB) bilayers

This thesis focuses on the oxide/ferromagnet metal, in particular MgO/Fe(Co), bilayer system. Extensive experimental investigations have been conducted on the voltage control of MA (VCMA) in this material class [6–52]. Most exciting results, like the voltage induced coherent magnetization switching [15, 18] and voltage driven FMR [22, 26], have been reported. Theoretically the VCMA can be explained reasonably well based on spin dependent charge screening [54, 55, 60] which mainly leads to a change of the d-orbital occupation of the transition metal atoms at the bilayer interface. This pure electronic effect is widely accepted to explain the voltage induced magnetization dynamics which take place on the sub nanoseconds timescale [15, 18, 22, 26]. However, a range of experiments show a VCMA which deviates from the behaviour expected from the theoretical models.

Several experiments report a strong unidirectional [30, 46, 52, 61] or hysteretic [6, 47] voltage dependence of the VCMA. In the experiments showing the unidirectional dependence, the VCMA is more or less non existent for one voltage polarity. In contrast, for the opposing polarity extremely high VCMA coefficients ξ[3] ranging from 290 fJ/Vm [46] to 1150 fJ/Vm [30] are observed. These values clearly exceed the theoretical predicted value

---

[3] In experiments the VCMA is measured in capacitor devices. The quantity used to compare the effect

of 100 fJ/Vm [58]. Two different possible explanations are usually given: charge trapping in the dielectric layer [17] or magneto ionic effects [62]. Magneto ionic effects refer to voltage induced O^- migration through the dielectric barrier, which then induces a reduction or oxidation of the transition metal at the bilayer interface. This mechanism itself is an exciting field of research with extraordinarily high values of ξ ~5000 fJ/Vm being reported [62, 122]. Magneto ionics are usually observed in oxide ion conductor/metal structures [61, 62, 122, 123]. Typically GdO is employed as oxide layer due to its anticipated high ionic conductivity. In systems which utilize an MgO barrier contradicting results exist regarding the voltage induced change of the interface chemistry. Both Bonel et al. [63] and Miwa et al. [37] investigated the oxidation state of a transition metal layer covered by MgO through X-ray absorption spectroscopy and magnetic circular dichroism measurements. Here Bonell et al. investigate MgO/Fe(O) structures and clearly show the reversible alteration of the Fe oxidation state with an applied gate voltage. Miwa et al. on the other hand could not detect any signs of oxidation state alteration in MgO/ FeCo tunnel structures.

A VCMA which is only at the interface of the oxide/magnet bilayer structure leads to a "Néel-type" thickness dependence of the VMCA. A decrease of ΔK_{eff} proportional to the inverse of the magnetic layer thickness and a constant ξ independent of the magnetic layer thickness are expected. Such dependency has been reported by Okada et al. who investigates the voltage control of the FMR position in MgO/CoFeB/Ta capacitor devices with a CoFeB thickness ranging from 1.4 nm to 1.8 nm. Another experiment confirming the interface origin of the VCMA is reported by Nawaoka et al. [39]. They investigate the thickness dependence on the MgO/Fe/Au structures with d_{Fe} ranging from 2 nm to 23 nm by measuring the gate voltage impact on the spin wave resonance frequency. In contrast to this finding stands the publication of Lau et al. [49]. They investigate the VCMA thickness dependence in MgO/CoFeB/Ta multilayer structures. By the area method applied to out- and in-plane magnetization curves they extract a ξ which increases with increasing CoFeB thickness by approximately a factor of two. As explanation they propose a thickness dependent film strain as origin of this most interesting observation. The alteration of strain is argued to lead to a modification of the electronic system at the MgO/CoFeB interface. A thickness dependent strain thus should translate into a thickness dependency of the VCMA. Following a phenomenological model proposed by Gotham et al. [106] they are able to fit their data through a voltage dependent MEA contribution. Within this

---

magnitude is the VCMA coefficient ξ, which is written as

$$\xi = \frac{\Delta K_{\text{eff}} \cdot d}{E}, \tag{2.25}$$

where E is the electric field inside the dielectric layer ΔK_{eff} is the electric field induced change of the effective MA constant and d is the thickness of the magnetic layer. In equation 2.25 a linear relation between ΔK_{eff} and gate voltage is assumed. Some confusion can arise as for capacitor devices with multiple dielectric layers it is not evident where E is measured. The material class of interest here all employ a MgO dielectric grown on top of the magnetic layer. For this kind of structures throughout the literature an agreement exists to use the electric field inside the MgO layer. The quantity ξ allows to compare various experimental results on the VCMA measured in different experiments.

model both thickness dependent magneto elastic constants (of higher order) and thickness dependent strain are assumed. The magneto elastic constants are extracted from a fit in the non-linear region of the $K_{\text{eff}} \cdot d_{\text{CoFeB}}$ vs. d_{CoFeB} plot (d_{CoFeB} is the CoFeB layer thickness). The fit to the VCMA data is then conducted by assuming that all magneto elastic contributions are affected by the gate voltage. In order to verify this procedure a theoretical substantiation is highly desirable. An experiment published by Naik et al. [35] could explain the linear increase of ξ with increasing thickness through an alteration of film strain with U_{g}. In their experiment they prove the inverse piezoelectric effect in thin film MgO layers by piezoelectric force measurements. If indeed such effect persists, it seems reasonable that a voltage induced strain in the MgO layer should be fully translated into the magnetic layer of a ferromagnet/MgO bilayer structure. As a result the VCMA originates in the volume of the magnetic layer. This effect then naturally leads to an linear increase of ξ with thickness.

Table 2.2 summarizes the magnitude of the maximum VCMA coefficient $|\xi_{\text{max}}|$ found in the magnetic layer of MgO/Fe(Co) based multilayers, relevant to this thesis. In this table only the materials in which the magnetic layer is embedded in are written. In case where several samples with different thickness of the magnetic layer are investigated only the maximum value magnitude of the VCMA coefficient $|\xi_{\text{max}}|$ is given. The column “lin. U_{g}” is denoted with a checkmark if the linear relationship between ξ and the gate voltage is observed. Interestingly, if this relationship is confirmed, a rather modest ξ ranging from 4 fJ/Vm to 100 fJ/Vm is reported. The high values observed are almost always linked to some peculiar voltage dependency where the electronic VCMA most likely is superimposed by charge trapping or magneto ionic effects. Please note that in case of Miwa et al. the column is denoted by “-”. Here the voltage dependency was not explored.

2.5. Ferromagnetic resonance

Ferromagnetic resonance (FMR) describes the resonant excitation of the magnetization by an electromagnetic microwave field. Measuring the FMR field (H_{FMR}) and lineshape allows to extract MA constants, g-factor and Gilbert damping of magnetic samples with very high accuracy [124].

The following discussion has four parts. In part one the macrospin approximation is introduced. Within this approximation the magnetic moments of a thin film layer can be described by one single magnetization vector, what greatly facilitates the mathematical description of the FMR. The equation by which the FMR is governed is called Landau-Lifschitz-Gilbert equation (LLG). The LLG equation is discussed in the second part. In the third part the LLG equation is solved for the case of a thin film with tetragonal lattice symmetry with additional uniaxial in-plan MA. The solution yields H_{FMR} and the FMR lineshape. In part four a method introduced by Smit, Beljer and Suhl is discussed. This methods allows to derive the FMR field in a very convenient way.

Layer structure	$\lvert\xi_{\mathrm{max}}\rvert$ (fJ/Vm)	lin. U_{g}	Reference
MgO/CoFeB/Ir	100	✓	[43]
MgO/Mg/CoFeB/Ta	100	✓	[51]
MgO/CoFeB/Ta	60	✓	[33]
MgO/CoFeB/Ta	29	✓	[31]
MgO/CoFeB/Ta	28	✓	[49]
MgO/CoFeB/Ta	11	✓	[19]
MgO/CoFeB/W	50	✓	[41]
MgO/CoFeB/W	14	✓	[49]
MgO/CoFeB/Mo	50	✓	[42]
MgO/CoFeB/Ru	18	✓	[31]
MgO/CoFeB/Ru	14	✓	[36]
MgO/CoFeB/Pt	4.2		[47]
MgO/FeCo/Au	38.5	✓	[15]
MgO/FeCo/Au	37.5	✓	[10]
MgO/FeCo/Au	30	✓	[14]
MgO/FeCo/Au	13	✓	[22]
MgO/Fe/Cr	370		[52]
MgO/Fe/Cr	290		[46]
MgO/Fe/Cr	100	✓	[46]
MgO/Fe/V	1150		[30]
MgO/Fe/V	23	✓	[44]
MgO/Fe/V	23	-	[37]
MgO/Fe/Ag	944		[17]
MgO/Fe/Au	93		[6]
MgO/Fe/Au	48	✓	[40]
MgO/Fe/Au	26	✓	[39]

Table 2.2.: Magnitude of the maximum VCMA coefficient $\lvert\xi_{\mathrm{max}}\rvert$ found in different MgO/Fe(CoB) based multilayers. The column “lin. U_{g}” is denoted by a checkmark if a linear relationship between U_{g} and the VCMA is measured.

2.5.1. Macrospin approximation

Within the macrospin approximation, the magnetic moments inside a thin film layer are represented by one magnetization vector $\vec{M}$. This approximation is justified whenever a uniform motion of the single magnetic moments can be assumed. The uniform alignment of the single moments is favored by the exchange interaction. This energy contribution is objected by the dipol-dipol interaction. The dipol-dipol interaction leads to the demagnetizing field whenever the the magnetic moments have a component pointing perpendicular to the sample surface. In order to reduce the energy costs of the resulting stray fields the magnetic moments will brake with their parallel alignment. The exchange interaction is the dominating energy contribution within the exchange length l_{ex}. This length is written as [124]

$$l_{\mathrm{ex}} = \sqrt{\frac{A}{\mu_o M_{\mathrm{s}}^2}}, \tag{2.26}$$

where A is the exchange constant. Thin films with a thickness smaller than l_{ex} are called ultrathin and in such layers the macrospin approximation is valid. For Fe equation 2.26 yields a l_{ex} of 3.3 nm [124].

2.5.2. Landau-Lifshitz-Gilbert equation

The dynamics of $\vec{M}$ is described by the Landau-Lifshitz-Gilbert (LLG) equation [78]:

$$\frac{\mathrm{d}\vec{M}}{\mathrm{d}t} = -\gamma_{\mathrm{g}} \vec{M} \times \mu_0 \vec{H}_{\mathrm{eff}} + \frac{\alpha}{M_{\mathrm{S}}} \vec{M} \times \frac{\mathrm{d}\vec{M}}{\mathrm{d}t}, \tag{2.27}$$

where γ_{g} is the gyromagnetic ratio, α is a dimensionless damping parameter and $\vec{H}_{\mathrm{eff}}$ is the effective field. The first term of the LLG equation 2.27 describes the precession of $\vec{M}$ around $\vec{H}_{\mathrm{eff}}$. The second term describes the damping of $\vec{M}$, which leads to an alignment of $\vec{M}$ along $\vec{H}_{\mathrm{eff}}$, if the excitation field is turned off. The gyromagnetic ratio is written as

$$\gamma_{\mathrm{g}} = g \frac{\mu_{\mathrm{B}}}{\hbar}, \tag{2.28}$$

where g is the g-factor, μ_{B} is the Bohr magneton and $\hbar$ is the reduced Planck constant. The g-factor for transition metal ferromagnets is quite close to 2, as the magnetic properties of these materials are mainly governed by their spin momentum. In case of Fe g is 2.09 [125]. The effective field sums up all field contributions relevant to the magnetic systems. According to reference [78] it is derived by

$$\vec{H}_{\mathrm{eff}} = -\frac{1}{\mu_0} \frac{\partial E_{\mathrm{tot}}}{\partial \vec{M}}, \tag{2.29}$$

where E_{tot} is the total magnetic energy of the system. The contributions entering E_{tot} are the MA and the Zeeman energy E_{Z}. The Zeeman energy describes the interaction of $\vec{M}$ with the external field $\vec{H}_{\mathrm{ext}}$ and is written as

$$E_{\mathrm{Z}} = \mu_0 \vec{H}_{\mathrm{ext}} \vec{M}. \tag{2.30}$$

The external field is composed of the static field $\vec{H}$ and the oscillating microwave field $\vec{h}(t)$. In total thus $\vec{H}_{\mathrm{eff}}$ is written as

$$\vec{H}_{\mathrm{eff}} = \vec{H}_{\mathrm{ani}} + \vec{H} + \vec{h}(t), \tag{2.31}$$

where $\vec{H}_{\mathrm{ani}}$ is the field arising from the MA contributions and can be calculated with equation 2.29.

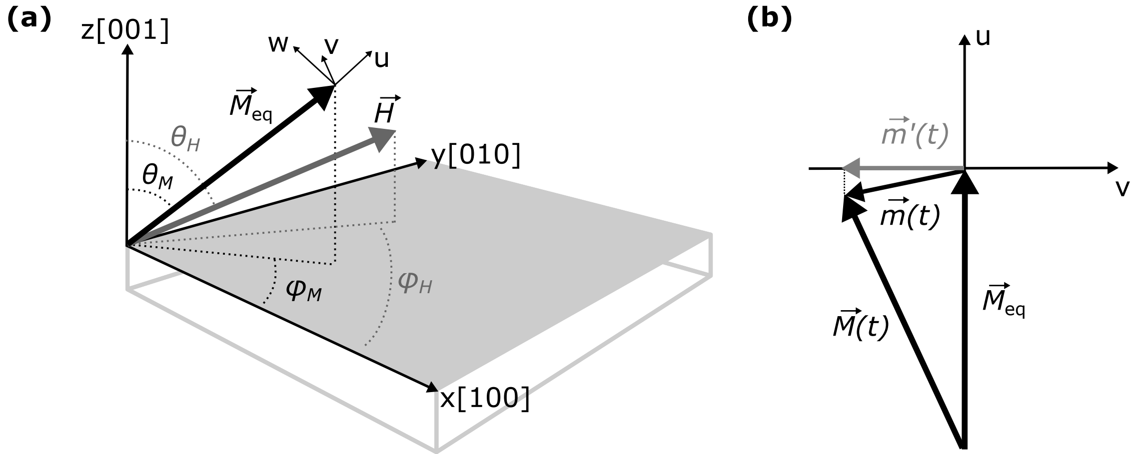

Figure 2.8.: (a) Illustration of the global (x,y,z) and local (u,v,w) coordinate systems which are involved in solving the LLG equation. The global coordinate system is fixed to the sample structure. The local coordinate system is defined by $\vec{M}_{\text{eq}} \parallel \hat{u}$. If a microwave field is applied, $\vec{M}(t)$ will precess around $\vec{M}_{\text{eq}}$. The precessing vector $\vec{M}(t)$ can be decomposed into an dynamic component $\vec{m}(t)$ and $\vec{M}_{\text{eq}}$ as shown in (b). For small amplitudes $\vec{m}(t)$ is approximated by $\vec{m}'(t)$, neglecting all changes along $\vec{M}_{\text{eq}}$.

2.5.3. Solving the Landau-Lifshitz-Gilbert equation

The FMR field and linewidth of a system with tetragonal MCA with additional in-plane uniaxial MA are derived by solving the LLG equation. In the derivation $\vec{h}(t)$ is assumed to oscillate perpendicular to the sample plane. In the following the equilibrium magnetization vector $\vec{M}_{\text{eq}}$ is defined as the magnetization vector where no $\vec{h}(t)$ is applied. The orientation of $\vec{M}_{\text{eq}}$ is assumed to be in the sample plane.

Solving the LLG is highly facilitated by a coordinate transformation from the global coordinate system (x,y,z) which is fixed to the sample structure, into a local coordinate system (u,v,w), defined by $\vec{M}_{\text{eq}} \parallel \hat{u}$. An illustration of these two coordinate systems and the variables involved in the LLG equation are shown in figure 2.8(a). The precessing magnetization vector $\vec{M}(t)$ in the global system can be decomposed according to

$$\vec{M}(t) = \vec{M}_{\text{eq}} + \vec{m}(t), \tag{2.32}$$

where $\vec{m}(t)$ is the dynamic component of $\vec{M}(t)$. For $|M(t)| >> |\vec{m}(t)|$, i.e. small precession amplitude, the precessing magnetization in the local is system $\vec{M}^{\text{loc}}(t)$ can be written as

$$\vec{M}^{\text{loc}}(t) \approx \hat{\text{u}} M_{\text{s}} + \vec{m}'(t) = \hat{\text{u}} M_{\text{s}} + \hat{\text{v}} m_{\text{v}}(t) + \hat{\text{w}} m_{\text{w}}(t) \tag{2.33}$$

where $\vec{m}'(t)$ is the dynamic component of $\vec{M}^{\text{loc}}(t)$ with the vector components $m_{\text{v}}(t)$ and $m_{\text{w}}(t)$. Figure 2.8(b) illustrates the relationship between $\vec{M}(t)$, $\vec{M}_{\text{eq}}$, $\vec{m}(t)$ and $\vec{m}'(t)$. At this point it becomes clear why the local coordinate system is introduced. The small angel approximation allows to describe the full precession motion by only two vector components in the local system. The microwave field in the local system is written as

$$\vec{h}(t)^{\mathrm{loc}} = \hat{w}he^{\mathrm{i}\omega t}, \tag{2.34}$$

where ω is the microwave field angular frequency[4] and h is the microwave field amplitude. As ansatz for $\vec{M}^{\mathrm{loc}}(t)$ a harmonic oscillator is chosen

$$\vec{M}^{\mathrm{loc}}(t) = \hat{\mathrm{u}}M_{\mathrm{s}} + \hat{\mathrm{v}}m_{\mathrm{v}}e^{\mathrm{i}wt} + \hat{\mathrm{w}}m_{\mathrm{w}}e^{\mathrm{i}wt}, \tag{2.35}$$

where $m_{\mathrm{v,w}}$ are the oscillation amplitudes along the v- and w-axis, respectively. Next, the expression of the anisotropy field and the static field in the local system, $\vec{H}^{\mathrm{loc}}_{\mathrm{ani}}$ and $\vec{H}^{\mathrm{loc}}$, have to be derived. This derivation is quite lengthy, especially in case of $\vec{H}^{\mathrm{loc}}_{\mathrm{ani}}$ where direction cosines of fourth order are involved, but can be conducted in a straight forward manner. In order to keep the discussion more well arranged this derivation is not shown here. Inserting $\vec{H}^{\mathrm{loc}}_{\mathrm{ani}}$, $\vec{H}^{\mathrm{loc}}$, $\vec{h}(t)^{\mathrm{loc}}$ and $\vec{M}^{\mathrm{loc}}(t)$ into the LLG and neglecting all higher order terms leads to a system of two linearly coupled equations which in the matrix notation are written as

$$\begin{pmatrix} m_{\mathrm{v}} \\ m_{\mathrm{w}} \end{pmatrix} = \begin{pmatrix} \chi_{\mathrm{vv}} & \chi_{\mathrm{vw}} \\ \chi_{\mathrm{wv}} & \chi_{\mathrm{ww}} \end{pmatrix} \begin{pmatrix} 0 \\ h \end{pmatrix}, \tag{2.36}$$

where χ_{ij} are the susceptibility tensor elements which are given by

$$\begin{pmatrix} \chi_{\mathrm{vv}} & \chi_{\mathrm{vw}} \\ \chi_{\mathrm{wv}} & \chi_{\mathrm{ww}} \end{pmatrix} = \frac{\mu_0 M_{\mathrm{s}}}{N} \begin{pmatrix} \mathcal{B}_{\mathrm{eff}} + \frac{i\omega\alpha}{\gamma} & \frac{\mathrm{i}\omega}{\gamma} \\ -\frac{\mathrm{i}\omega}{\gamma} & \mathcal{H}_{\mathrm{eff}} + \frac{\mathrm{i}\omega\alpha}{\gamma} \end{pmatrix}, \tag{2.37}$$

where

$$N = \left(\mathcal{H}_{\mathrm{eff}} + \frac{\mathrm{i}\omega\alpha}{\gamma}\right)\left(\mathcal{B}_{\mathrm{eff}} + \frac{\mathrm{i}\omega\alpha}{\gamma}\right) - \left(\frac{\omega}{\gamma}\right)^2, \tag{2.38}$$

and

$$\mathcal{H}_{\mathrm{eff}} = \mu_0 H \cos(\phi_H - \phi_M) + \frac{2K_4^{\parallel}}{M_{\mathrm{s}}}\cos(4\phi_M) + \frac{2K_{\mathrm{u}}^{\parallel}}{M_{\mathrm{s}}}\cos(2\phi_M - 2\phi_{\mathrm{u}}), \tag{2.39}$$

and

$$\mathcal{B}_{\mathrm{eff}} = \mu_0 H \cos(\phi_H - \phi_M) - 2\frac{K_{\mathrm{eff}}}{M_{\mathrm{s}}} + \frac{K_4^{\parallel}}{2M_{\mathrm{s}}}\Big(\cos(4\phi_M) + 3\Big) + \frac{K_{\mathrm{u}}^{\parallel}}{M_{\mathrm{s}}}\Big(\cos(2\phi_M - 2\phi_{\mathrm{u}}) + 1\Big), \tag{2.40}$$

where $\mathcal{B}_{\mathrm{eff}}$ and $\mathcal{H}_{\mathrm{eff}}$ are the effective magnetic induction and the effective magnetic field [126]. At this point often the effective magnetization $M_{\mathrm{eff}} = -2K_{\mathrm{eff}}/M_{\mathrm{s}}$ is introduced. M_{eff} is a convenient quantity as it usually directly gives the saturation field of a sample magnetized perpendicular to its surface. Here M_{eff} is not introduced. Instead K_{eff} is remained, which is the common quantity for describing the MA contributions favoring PMA in ultrathin Fe(CoB) films.

---

[4] Often the microwave field frequency f is used which is simply defined by $f = \omega/2\pi$

Ferromagnetic resonance field

The FMR field (H_{FMR}) is directly related to the maximum of the susceptibility tensor elements described by equation 2.37. This maximum occurs where N equals zero, see equation 2.38. Ignoring the damping, which is very small compared to $\mathcal{B}_{\mathrm{eff}}$ and $\mathcal{H}_{\mathrm{eff}}$ [127], N being zero leads to:

$$\left(\frac{\omega}{\gamma}\right)^2 = \mathcal{H}_{\mathrm{eff}}\mathcal{B}_{\mathrm{eff}}\Big|_{H_{\mathrm{FMR}}}. \tag{2.41}$$

which is the famous Kittel formula by which H_{FMR} in dependence of the excitation conditions and the MA landscape is derived.

For the standard experimental conditions it is common that $\vec{H}_{\mathrm{ani}}$ is of the same magnitude as H_{FMR}. In this case, ϕ_M (strongly) deviates from ϕ_H, whenever $\vec{H}$ is not aligned with the easy axes of the system. This leads to the so called "magnetization dragging". In order to fit data to the Kittel equation the equilibrium position of ϕ_M has to be calculated first. The equation relating ϕ_M and ϕ_H is derived by the torque condition which in equilibrium demands

$$\vec{M}_{\mathrm{eq}} \times \vec{H}_{\mathrm{eff}} = 0. \tag{2.42}$$

Inserting all variables into equation 2.42 leads to

$$\mu_0 H \sin(\phi_H - \phi_M) - \frac{K_4^{\|}}{2M_S}\sin(4\phi_M) - \frac{K_U^{\|}}{M_s}\sin(2\phi_M - 2\phi_{\mathrm{u}}) = 0. \tag{2.43}$$

Experimental data has to be fitted self consistently to the Kittel equation 2.41, where magnetization dragging described by equation 2.43 is taken into acount. This method allows to extract all MA constants and the g-factor of a magnetic thin film structure by measuring the H_{FMR} vs. ϕ_H relationship at two different (far apart) excitation frequencies [78].

Ferromagnetic resonance lineshape

The FMR lineshape is derived from the susceptibility tensor elements. The FMR spectra discussed in this thesis are measured in the TR-MOKE setup in polar configuration, where only the out-of-plane magnetization component is probed. Thus the FMR lineshape is yielded by χ_{ww} which, according to equation 2.36, is written as

$$\chi_{\mathrm{ww}} = \frac{m_{\mathrm{w}}}{h} = \frac{\mu_0 M_{\mathrm{s}}(\mathcal{H}_{\mathrm{eff}} + \frac{\mathrm{i}\omega\alpha}{\gamma})}{\left(\mathcal{H}_{\mathrm{eff}} + \frac{\mathrm{i}\omega\alpha}{\gamma}\right)\left(\mathcal{B}_{\mathrm{eff}} + \frac{\mathrm{i}\omega\alpha}{\gamma}\right) - \left(\frac{\omega}{\gamma}\right)^2}. \tag{2.44}$$

It can be shown that χ_{ww} can be expressed by an almost perfect Lorentzian function [127]:

$$\chi_{\mathrm{ww}} = M_{\mathrm{s}}\frac{\mathcal{H}_{\mathrm{eff}}}{\mathcal{B}_{\mathrm{eff}} + \mathcal{H}_{\mathrm{eff}}}\Bigg|_{H_{\mathrm{FMR}}}\frac{(H - H_{\mathrm{FMR}}) - \mathrm{i}\Delta H}{(H - H_{\mathrm{FMR}})^2 + \Delta H^2}, \tag{2.45}$$

where ΔH is the FMR linewidth, her defined as the half width at full maximum, which is written as

$$\Delta H = \frac{\omega\alpha}{\gamma}. \tag{2.46}$$

The real part of equation 3.13 described a perfect antisymmetric and the imaginary part a perfect symmetric Lorentzian function. Deviations from this perfect Lorentzian form have to be considered whenever H_{FMR} becomes comparable to ΔH [127].

2.5.4. The Smit and Beljer equation

According to Smit and Beljer [128] and Suhl [129], H_{FMR} can be directly calculated by

$$\left(\frac{\omega}{\gamma}\right)^2 = \frac{1}{M_{\mathrm{s}}^2 \sin^2\theta_M} \left[\frac{\partial^2 E_{\mathrm{tot}}}{\partial\theta_M^2}\frac{\partial^2 E_{\mathrm{tot}}}{\partial\phi_M^2} - \left(\frac{\partial^2 E_{\mathrm{tot}}}{\partial\theta_M \partial\phi_M}\right)^2\right]\Bigg|_{H_{\mathrm{FMR}}}, \tag{2.47}$$

as long as θ_M is not zero. Deriving H_{FMR} from equation 2.47 is very convenient. This method can be used whenever the lineshape is not of interest. Furthermore equation 2.47 allows to interpret the FMR spectra as representative of the MA landscape curvature. This insight explains why the minimum of the H_{FMR} vs. ϕ_H plot in general does not coincide with the easy axis of the system.

2.6. Magneto-optic Kerr effect

The magneto-optic Kerr[5] effect (MOKE) induces a rotation of linear polarized light upon reflection from a magnetic sample. This rotation is quantified by the angle θ_{K}. Furthermore the reflected light beam will in general be of elliptical shape, characterized by the Kerr ellipticity ϵ_{K}. In certain configurations θ_{K} and ϵ_{K} are linearly dependent on a samples magnetization, which allows to determine magnetization curves by measuring the field dependent Kerr response.

The MOKE is well described by macroscopic theory, i.e. solving the Maxwell equations with proper boundary conditions. Here the off-diagonal elements of the perimittivity tensor induce the Kerr effect. The change of θ_{K} and ϵ_{K} are a direct consequence of the different propagation velocities and absorption coefficients of right- and left-hand circular polarized light components in a magnetic medium. A detailed description of the MOKE in macroscopic theory is given for example in the reference [71]. The true microscopic origin can only be understood in the frame of quantum mechanics, where it is shown that the alteration of lights polarization upon reflection from a magnet is caused by exchange interaction and spin-orbit coupling.

In particular one distinguishes in between three different Kerr effects: the polar MOKE (PMOKE), the longitudinal MOKE (LMOKE) and the transversal MOKE (TMOKE). A

---

[5] The effect is name after John Kerr who first reported on it in 1877 [130, 131].

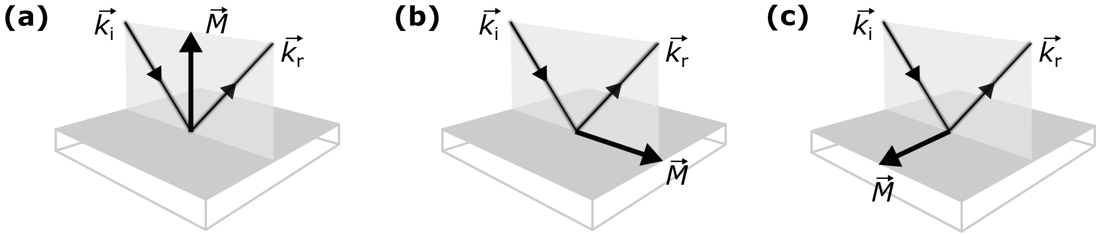

Figure 2.9.: Illustration of the geometrical configuration where the (a) PMOKE (b) LMOKE and (c) TMOKE is observed upon reflection of a linear polarized light beam from a magnetic sample surface. $\vec{k}_\mathrm{i}$ and $\vec{k}_\mathrm{r}$ are incoming and reflected light beam vector, respectively.

schematic representation of the geometrical configurations where PMOKE, LMOKE and TMOKE are observed is given in figure 2.9(a), (b) and (c), respectively. The geometrical configuration is defined by the relative orientation between the samples magnetization and the light beam plane of incidence. The PMOKE is observed where the samples magnetization is oriented out-of-plane and furthermore is in the plane of incidence. The LMOKE is observed where the samples magnetization again is in the plane of incidence and furthermore in the samples plane. Finally the TMOKE is observed where the magnetization is in the sample plane and furthermore oriented perpendicular to the plane of incidence. For both PMOKE and LMOKE an alteration of θ_K and ϵ_K is observed in the reflected part of linear polarized light. In case of metals the saturation Kerr rotation $\theta_\mathrm{K,s}$ and saturation Kerr ellipticity $\epsilon_\mathrm{K,s}$ are quite small, i.e. in the order of 1 mdeg, because of the short skin depth (~10 nm for light in in the visible spectrum) which limits the penetration depth of the impinging light beam. The TMOKE only induces a reduction of intensity in the reflected light beam. Usually the PMOKE is the biggest effect (usually ten times larger than the LMOKE). The smallest effect is in general is the TMOKE (orders of magnitudes smaller than the PMOKE and LMOKE).

The separation in PMOKE, LMOKE and TMOKE should not be confused with the geometrical configuration of a MOKE setup which is used to measure magnetization curves. A description of the MOKE setup in polar and longitudinal configuration is given in section 3.5. For example in the longitudinal configuration the measured signal might be induced by both the LMOKE and the PMOKE. In particular this is the case for sample with PMA. Here, the PMOKE might even dominating the signal and extracting the true in-plane magnetization curve in general is quite cumbersome [132].

One disadvantages of measuring magnetization curves by MOKE is that $\theta_\mathrm{K,s}$ and $\epsilon_\mathrm{K,s}$ crucially depend on the magnetic film thickness [133–138], the wavelength of the light source [136, 137, 139] the angle of incidence [140] and furthermore the substrate and capping layer [134, 137, 139, 141]. Thus it is very cumbersome, if not impossible, to extract M_s from the measured $\theta_\mathrm{K,s}$ or $\epsilon_\mathrm{K,s}$. If one wants to measure M_s, magnetometric methods like alternating gradient magnetometry, vibrating sample magnetometry or superconducting quantum interference device magnetometry have to be employed.

3. Experimental methods

This chapter covers the experimental setups employed in the sample growth, microfabrication, magnetic characterization and measurement of the VCMA. The chapter has seven parts. The first part addresses the ultrahigh vacuum (UHV) molecular beam epitaxy (MBE) system where the epitaxial layers are prepared. The second part discusses the reflection high-energy electron diffraction (RHEED) system utilized to investigate the crystalline quality of the epitaxial films. Part three and four cover the metallization and atomic layer deposition (ALD) system, respectively. In part five the MOKE system utilized to measure static in- and out-of-plane magnetization curves is described. The modifications of this system, which allow to measure the VCMA, are discussed in the sixth part. In the final part the TR-MOKE setup is described which is utilized to measure the FMR.

3.1. Molecular beam epitaxy system

The investigated ultrathin epitaxial magnetic layers are grown in a MBE system which was built up from scratch as part of this thesis. A 3D computer aided design (CAD) drawing of the system is shown in figure 3.1. The system consists of three interconnected chambers: the MBE, the sputter and the load-lock chamber. The individual chambers are described in detail in the following.

Load-lock chamber

The load-lock is pumped by a 68 l/s turbomolecular pump backed by a 1.4 l/s rotary vane pump. The pressure (p) is monitored through a full range (combination of magnetron and thermal) gauge. The base pressure (p_b) of the load-lock chamber is approximately 5×10^{-8} mbar. After a pumping time of 30 minutes p reaches a value of approximately 5×10^{-6} mbar. At this p and below the sample transfer does not affect p_b of the sputter chamber. After 12 h, p drops to approximately 2×10^{-7} mbar. At this p the sample transfer does not affect p_b of the MBE chamber. The load lock chamber p_b is approximately 5×10^{-8} mbar.

Figure 3.2(a) and (b) show 3D CAD drawings of the systems sample holder from two different perspectives. The sample holder body is made of a stainless steel. Substrates of dimension of up to 10 mm × 10 mm can be clamped onto the sample mount made of molybdenum. The substrates can be heated through radiation as illustrated in figure 3.2(c). The sample temperature is estimated from a thermocouple pressed onto the backside of the

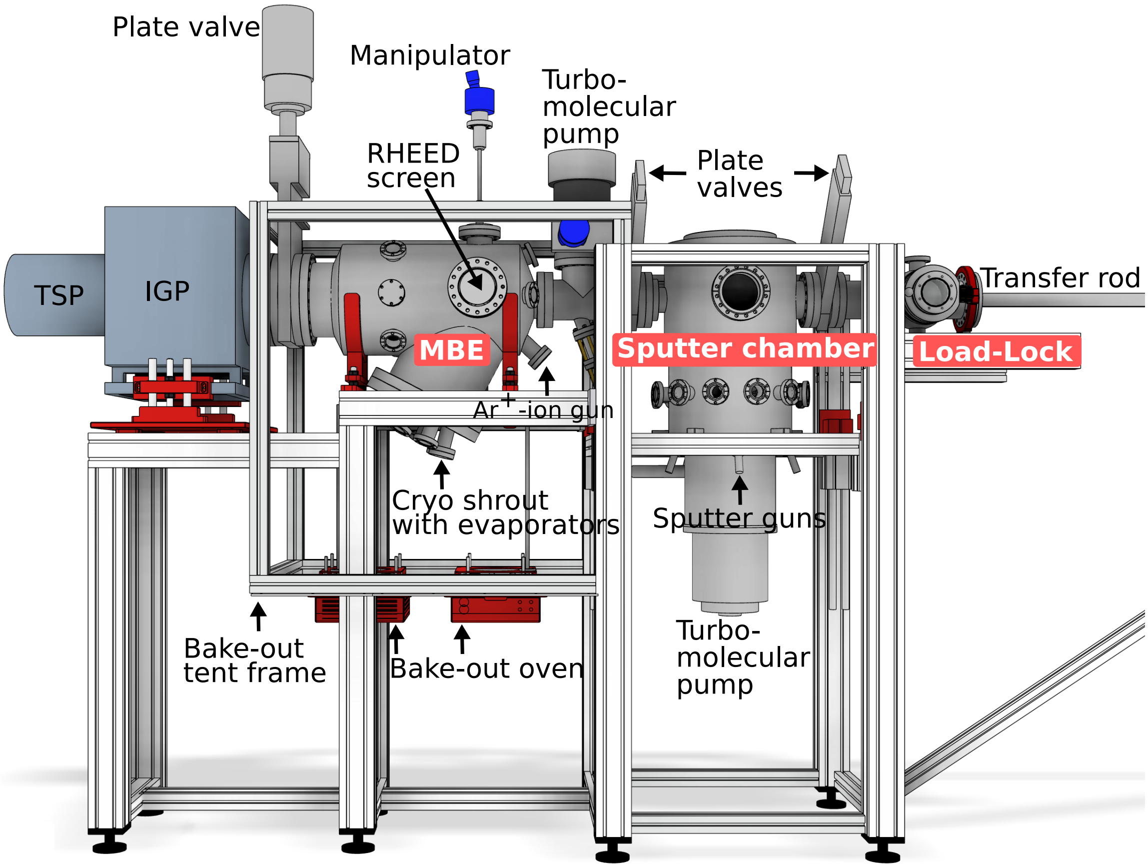

Figure 3.1.: 3D CAD drawing of the (UHV) MBE system which was developed and built up during this thesis. The system consists of three interconnected chambers: the MBE, the sputter and the load-lock chamber.

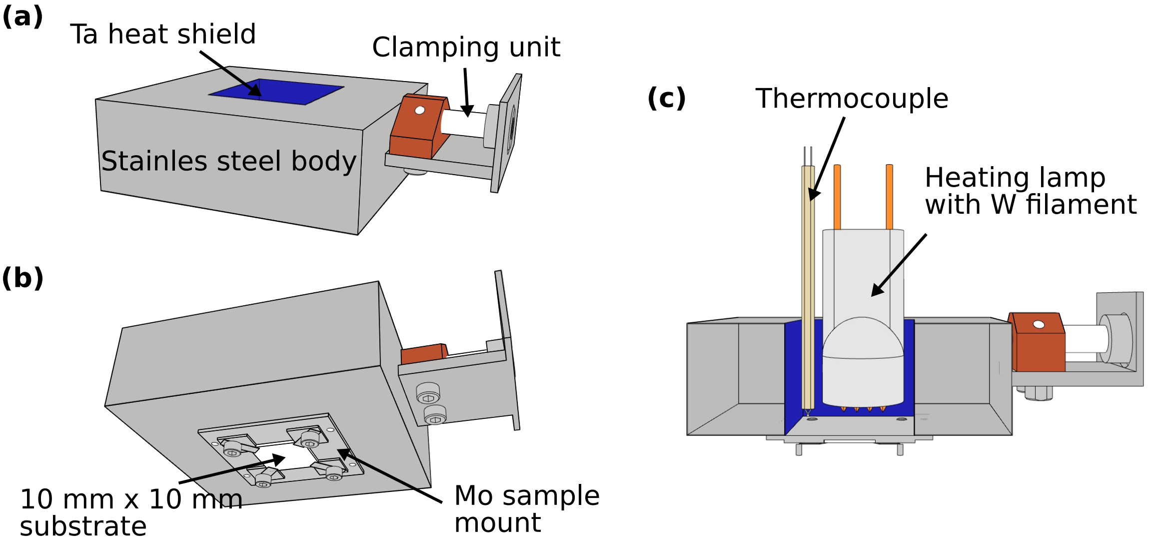

Figure 3.2.: CAD technical drawings of the MBE sample holder. The sample holder is shown from two different angles in figure (a) and (b). In figure (c) the sample heating is illustrated.

mounting plate. In order to improve the reliability of the temperature estimation the following calibration procedure is conducted: A thermocouple is directly fed into to the load-lock chamber and connected to the front side of a MgO substrate clamped onto the molybdenum sample mount. The temperature reading of the filament connected to the MgO substrate is recorded in dependence of the heating filament power. This temperature Mvs. power dependence is then used to calibrate the temperature reading of the permanently mounted thermocouple. It is well known that the estimation of the sample temperature via thermocouple is not very reliable and is the main reason why often growth recipes cannot simply be transferred from one system to another [142]. In principle more sophisticated methods like pyrometry or using optical detectable band transitions exist and it would be a useful addition to the system in future.

Sputter chamber

The sputter chamber is pumped by 690 l/s turbomolecular pump backed by a 2.2 l/s rotary vane pump. The chamber pressure is monitored through a full range (combination of magnetron and thermal) gauge. The sputter chamber p_b is approximately 3×10^{-8} mbar.

Five 2 inch DC magnetron sputter sources are installed. As sputter gas argon of purity 6 N is used. A computer regulated mass flow controller is employed to control the Ar gas flow into the chamber. The system is fairly easy to vent, as no bake out procedure is employed to lower p_b, which allows for a quick exchange of sputter targets. Typical metal targets installed in the chamber are Au, Ag, Pt, Ta, W, Py, Cr, Cu and Co. The sputter deposition is conducted at an Ar background p of 4×10^{-3} mbar with an acceleration voltage of 500 V. The sample-source distance is approximately 80 mm. Depending on the exact Ar background p, the acceleration voltage and the sputter material deposition rates ranging from 0.1 Å/s to 3 Å/s are commonly achieved. The growth rate during sputter deposition can be monitored by a quartz crystal microbalance (QCM).

MBE chamber

The MBE chamber is pumped by a combination of lubricant-free pumps, which ensures a carbon free vacuum environment, vital for reaching UHV. The employed pumps are a 270 l/s magnetically beared turbomolecular pump with drag stage, backed by a lubricant free 3.2 l/s scroll pump, a 200 l/s ion getter pump and a titanium sublimation pump embedded in a liquid N_2 cryo shroud which, whenever cooled down, further enhances the combined pumping speed. Even such a powerful combination of pumps would take an infinitely long timespan to remove all water from the chamber walls due to the unfavorable desorption rate of water at room temperature [143]. The p_b of an unbaked system thus usually is restricted to around 1×10^{-8} mbar. In order to reach UHV it is essential that the whole system can be heated up to temperatures where the residue water inside the chamber can be effectively removed from the system within a couple of days. The MBE system has a custom made

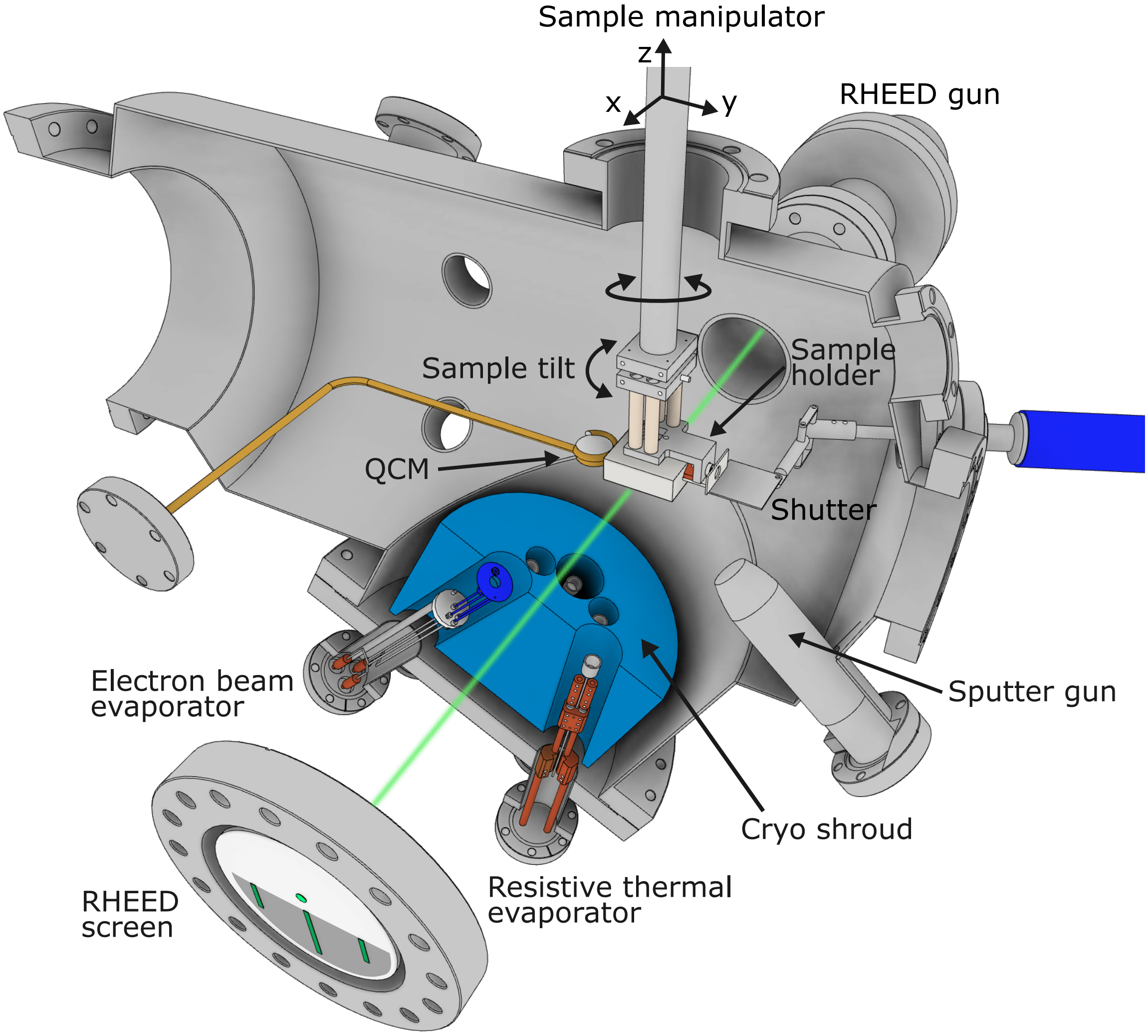

Figure 3.3.: Cross sectional 3D CAD drawing of the MBE chamber.

bake-out tent made out of fireproof tarp which can be easily mounted on a MiniTec frame surrounding the MBE chamber, see figure 3.1. Two oven heaters are installed in the bottom of the bake out tent as well as two PT 100 sensors for temperature monitoring. A bake-out procedure sufficient to remove all residue water is conducted at a temperature of 150 °C for 3 days. After this procedure the MBE chamber reaches a p_b better than 5×10^{-11} mbar. The pressure inside the MBE chamber is measured by a hot cathode gauge. Next the main components installed inside the MBE chamber are described.

A cross sectional 3D CAD drawing of the MBE chamber is shown in figure 3.3. The sample manipulator allows a linear translation of the sample holder along all three (x, y and z) directions in space. Furthermore the sample can be rotated around the z-axes and tilted such that the glancing angle between the electron beam of the RHEED gun and the sample surface can be adjusted. A Staib RHEED system operating at an acceleration voltage of 10 kV is installed in the system, allowing to observe the surface quality of the prepared epitaxial layer structures. A detailed description of RHEED is given in section 3.2. In total eight deposition sources are embedded in a liquid N_2 cryo shroud. All sources can be closed individually by a shutter placed right at the shroud opening (not shown in the CAD technical drawing). Two types of deposition sources are installed in the system: resistive thermal evaporators (RTE) and electron beam (e-beam) evaporators. Both RTE and e-beam evaporator where completely developed and manufactured in the frame of this thesis. A detailed description can be found in the appendix A. In the following only the main features are described: The RTE is used for the deposition of low vapor pressure metals like Au, Ag, Co, Fe, Py, Ni, Cr and Pd. The e-beam evaporators are used to deposit oxides like MgO and Al_2O_3. The sample-source distance inside the MBE chamber is approximately 170 mm. Typical growth rates which are achieved with the RTE are in the order of 1 ML/min to 3 ML/min, strongly depending on material and heating power. For example, 200 W of power yields a deposition rate of 2 ML/min during Fe deposition. The pressure during the Fe deposition typically stays in the low 1×10^{-10} mbar region, as the 200 W heating power are effectively absorbed by the liquid N_2 cryo shroud. The growth rate is measured by QCM (whenever RHEED oscillations cannot be observed). The MBE is furthermore connected to a O_2- and Ar-gas minican of 6 N purity (not shown in the 3D CAD drawing). The gas flow of both gases is adjusted by a mechanical leak valve. Finally, an Ar^+-ion sputter gun is installed in the MBE chamber. The angle between the Ar-ion beam and the sample surface normal is 43° and the distance between the gun opening and the sample surface is approximately 73 mm. The gun typically is operated at an Ar background p of 5×10^{-5} mbar.

3.2. Reflection high-energy electron diffraction

RHEED is a non destructive surface analysis tool widely employed in the MBE film preparation. In comparison to other surface analysis methods like low-energy electron diffraction, scanning tunneling microscopy or atomic force microscopy, the RHEED apparatus does not disturb the growth process and thus can be used to monitor the epitaxy in real time.

Figure 3.4 shows a 3D CAD drawing of the RHEED setup installed in the MBE chamber built up during this thesis, which, without further restriction, can be used as model for the typical RHEED setup. The general operation principle of a RHEED setup is as follows: An electron beam with an energy between 8 keV and 20 keV [144] is focused on the surface of a sample under grazing incidence (angle between sample surface normal and electron beam not bigger than a couple degree). A crystalline sample surface effectively acts like a diffraction grating on the electron beam leading to constructive interference along directions which are specified below. The diffracted beams and the so called through beam (caused by part of the electron beam missing the sample) are focused on a phosphoric screen leading to the RHEED pattern of the sample. The grazing incidence and the strong sample-electron beam interaction leads to a very short effective penetration depth of the electron beam into

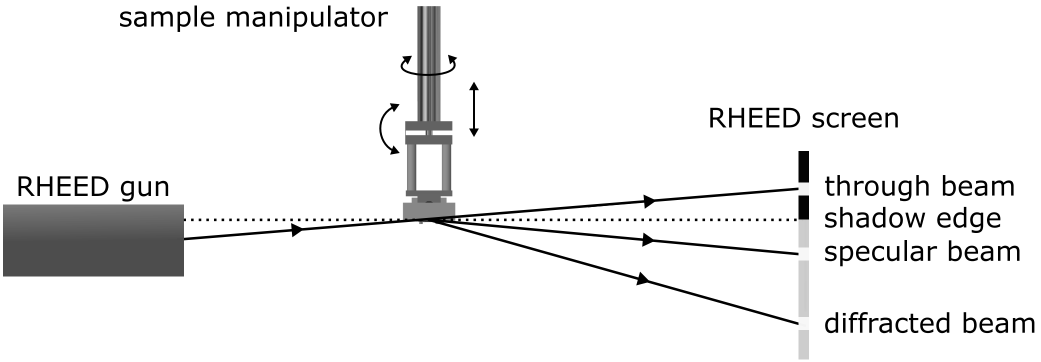

Figure 3.4.: 3D CAD drawing of the RHEED setup installed in the MBE chamber.

the volume of the sample. Thus the RHEED pattern is regarded to (mainly) reflect the crystalline arrangement of the sample surface atoms .

In the following two parts a description of RHEED patterns in terms of kinematic scattering is given, followed by a discussion of RHEED oscillations.

RHEED patterns

The main RHEED pattern features can be understood in terms of kinematic theory assuming elastic scattering by means of Ewald's sphere construction in reciprocal space [124, 142, 144].

As starting point of the discussion an ideally flat crystal surface, where the respective reciprocal space consists of infinitely long rods, is considered. The conditions for constructive interference in this case are written as

$$\vec{G} = \vec{k}_0 - \vec{k}', \tag{3.1}$$

and

$$|\vec{k}_0| = |\vec{k}'| = k, \tag{3.2}$$

where $\vec{G}$ is a reciprocal lattice vector, $\vec{k}_0$ is the incident wave vector and $\vec{k}'$ is the diffracted wave vector. The wave vector magnitude is described by k. The Ewald sphere is defined as a sphere in reciprocal space with radius k. The condition for constructive interference is then obtained by the intersection points of the Ewald sphere and the reciprocal lattice rods. An illustration of the Ewald sphere construction is shown in figure 3.5. A cubic crystal surface with lattice constant a is assumed where the respective reciprocal lattice rods are placed on a cubic mesh with lattice spacing $2\pi/a$. Please note that for reasons of visual clarity only the first two rows of reciprocal lattice rods intersecting the Ewald sphere and only incoming and specular beam are illustrated. Furthermore the scale does not represent true experimental conditions properly, which will be addressed later. From figure 3.5 one can see that the RHEED pattern of a perfectly flat crystal surface of cubic

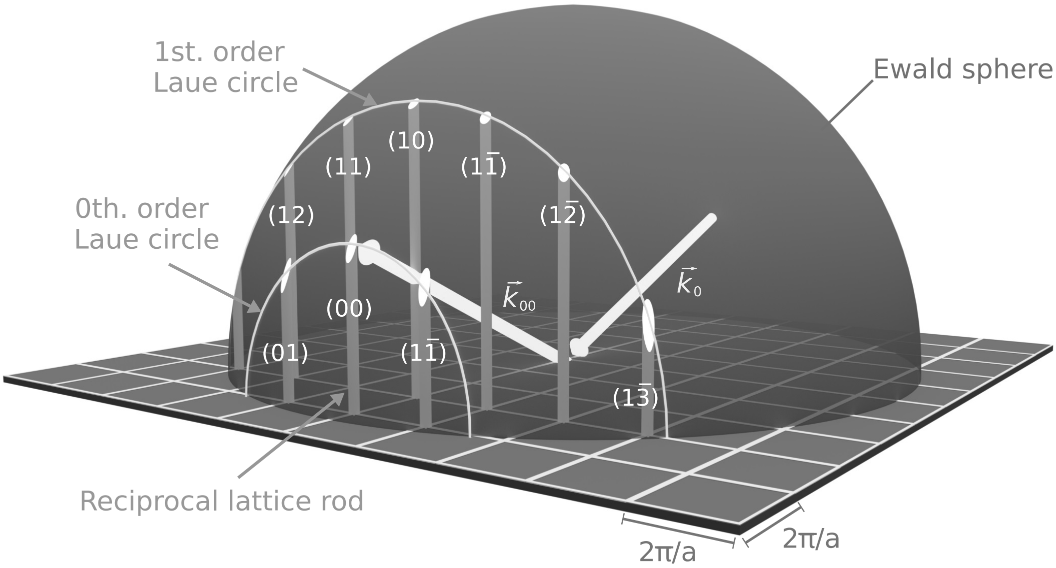

Figure 3.5.: Ewald sphere construction in reciprocal space used to derive the RHEED pattern of a cubic crystal surface. $\vec{k}_0$ and $\vec{k}_{00}$ are the incident and the specular beam. The conditions for constructive interference are fulfilled at the intersection of Ewald sphere and reciprocal lattice rods. The diffraction spots are labeled with respect to the reciprocal lattice rod index (hk). For visual clarity only the reciprocal lattice rods causing the diffraction spots on the zeroth and first order Laue circle and the zeroth order diffracted beam are shown. Further explanations are given in the text.

symmetry consist of discrete diffraction spots arranged on the so-called Laue circles. The diffraction spots and beams are labeled with respect to the reciprocal lattice rod index (hk). Per definition, the (00) diffraction spot is caused by the specular beam. As already mentioned, the scaling used in the Ewald's sphere illustration shown in figure 3.5 does not represent the true experimental conditions. For example, for bcc Fe the reciprocal lattice spacing is $2.2\,\text{Å}^{-1}$ and an electron beam accelerated by 10 keV has a k of $50\,\text{Å}^{-1}$. The Ewald's sphere radius thus is far bigger than illustrated in figure 3.5. As a consequence, the Ewald's sphere intersects the reciprocal lattice rods almost perpendicularly. Any thickening of the reciprocal lattice roads or Ewald's sphere thus leads to streaks rather than discrete spots observed in the RHEED pattern. A thickening of the lattice rods generally occurs whenever the surface roughness increases, for example by surface steps or misfit dislocations [124]. The Ewald's sphere on the other hand always has a certain thickness caused by the uncertainty in the electron beams energy distribution. In the following, typical RHEED patterns observed in experiment are described and related to the sample surface morphology.

The RHEED pattern of a slightly stepped surface is similar to that of a perfectly flat surface, where the diffraction spots are arranged on the Laue circles. However, the diffraction spots will be slightly blurred and elongated along the direction perpendicular to the sample surface. With increasing step density, the RHEED pattern will more and more transform into long streaks. Long sharp streaks, with a low diffuse background, are still considered

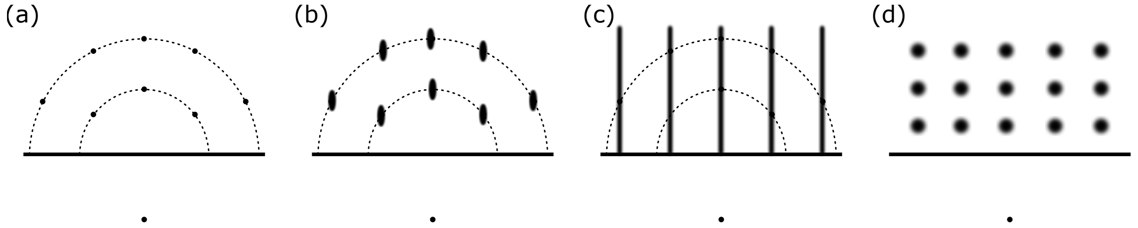

Figure 3.6.: Illustration of typical RHEED patterns observed in experiment. The pattern shown in figure (a), (b), (c) and (d) indicate a perfectly flat, slightly stepped, moderately stepped and 3D surface, respectively. The horizontal line in each figure is the shadow edge. The spot in the lower part of each figure is corresponds to the through beam. The dotted circles in figure (a), (b) and (c) illustrate the Laue circle of 0th. and 1st. order.

as indication of a “good” epitaxial surface with moderate surface step density [124]. In the extreme case of a 3D surface the electron beam is diffracted from several atomic steps with strongly varying hight. Effectively this corresponds to a volume diffraction process and the reciprocal lattice rods are replaced by the reciprocal lattice grid. The RHEED pattern in this case will appear as spots reflecting the reciprocal lattice grid symmetry. Due to the rough surface of a 3D configuration the RHEED spots are furthermore blurred. The above described RHEED patterns which indicate a perfectly flat, slightly and moderately stepped, and a 3D surface are illustrated in 3.6(a), (b), (c) and (d), respectively.

Further features encountered in RHEED patterns can be explained in terms of kinematic scattering theory. Surface reconstructions for example lead to additional streaks appearing in between the main diffraction streaks [29]. Spot splitting is associated with vicinal surfaces [145]. A rectangular network of misfit dislocations leads to additional sheet formation in reciprocal space which appear as fan-out streaks in the RHEED pattern [146, 147].

RHEED oscillations

RHEED oscillations are referred to oscillations in the intensity of a diffraction spot occurring during epitaxial growth. It is well accepted that RHEED oscillations are induced by a periodic surface morphology change, where the growth of 1 ML of material corresponds to one full RHEED oscillation [148]. Thus, whenever RHEED oscillations are measured during epitaxy the growth is thought to occur in the LBL mode and consequently one talks about “good” epitaxial growth.

The simplest explanation of RHEED oscillations is given in terms of Bragg scattering. In this model the electron scattering is assumed to only take place on the topmost atomic layer. Setting the incident angle to the anti-Brag condition then leads to a minimum of the RHEED intensity for a half filled layer (where the electron beam scattered from the bottom and top layer interfere destructively) and a maximum of the RHEED intensity for full layer coverage. The RHEED intensity then oscillates in between its maximum value for full coverage and minimum value for half filled coverage. However, in experiment strong oscillations can be observed even in case where the incident beam angle does not fulfill the anti-Bragg condition [142]. Furthermore it is shown, that the RHEED oscillation phase has no clear correlation with the layer roughness [142], which also cannot be explained by the simple Bragg model. The RHEED oscillations phase and incidence angle dependencies can be described by taking into account variations of the step-edge density and dynamic theory [124, 142, 144].

The damping of RHEED oscillations usually indicates a roughening of the sample surface. This can be caused by low deposition temperatures, where the surface mobility of the adatoms is not sufficient to reach already existing nucleations sites. Instead, they stick to the site of arrival. Furthermore roughness can be caused by the formation of misfit dislocations. Misfit dislocations are commonly formed during pseudomorphic growth with increasing film thickness in order to relieve the increasing film stress. However, RHEED damping does not always indicate a surface roughening. RHEED oscillations damping can also be caused by an increase of long-range roughness [148, 149] due to the formation of terraces similar in size to the mean nucleation range of the atoms. At this point the growth will take place in the step-flow-mode and RHEED oscillations are not observed anymore. This is often the case for homo epitaxial growth where the RHEED oscillations are only slightly damped [142].

3.3. Metallization system

The metallization system is used to prepare thin metallic films whenever the highest UHV standard of the MBE chamber is not needed. The system is not baked-out, which makes it fairly easy to maintain. This and the advantage that samples are loaded very quickly makes the system an essential tool for the microfabrication of devices. The metallization system was completely built from scratch as part of this thesis.

Figure 3.7(a) shows an image of the metallization chamber system. The system consists of two interconnected chambers: the fast entry load-lock and the main chamber. The fast entry load lock is pumped by 70 l/s turbomolecular pump, which is roughed by a 0.4 l/s rotary vane pump. Approximately five minutes of pumping time is enough to reach a pressure in the 1×10^{-5} mbar region. This pressure is good enough for transferring the sample into the main chamber. The main chamber is pumped by a 360 l/s turbomolecular pump, which is backed by a 2.8 l/s roughing pump. The pressure of the main chamber is measured by a cold cathode gauge. In full operation, the base pressure is approximately 5×10^{-8} mbar.

Next the main components of the metallization chamber are discussed. Figure 3.7(b) shows a 3D CAD drawing of the chambers interior. The sample is mounted on a manipulator allowing to rotate and translate the sample along the z-axes of the system. A mechanical shutter is installed below the sample holder. Low vapor pressure metals are deposited by RTEs. Eight fully homebuilt RTE are mounted on the system. A detailed description of the

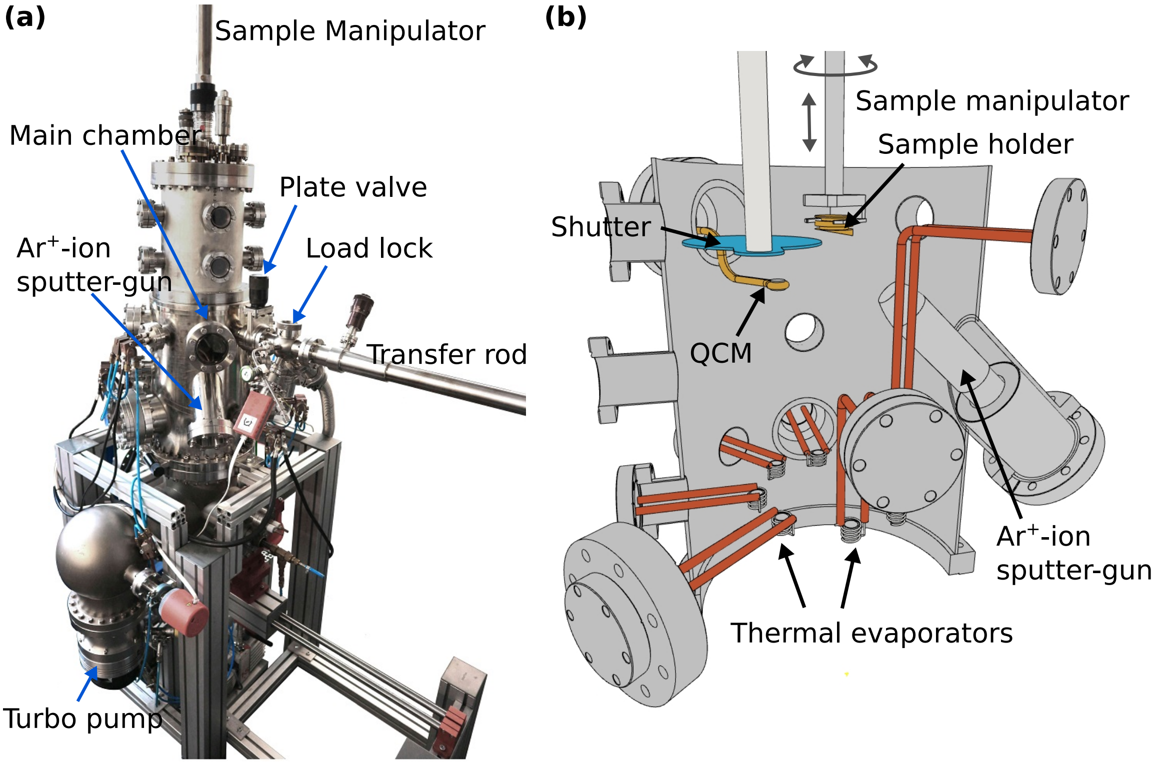

Figure 3.7.: (a) Picture of the metallization system. The system consists of a fast entry load-lock interconnected to the main chamber. (b) Technical drawing showing the interior of the metallization system main chamber. Here a variety of low vapor metals can be deposited through thermal evaporation. The film thickness is measured by means of QCM during deposition. Surface cleaning is done through Ar^+-ion milling.

RTE employed in the metallization chamber is given in the appendix A. These evaporators allow to deposit a variety of low vapor pressure metals, like Au, Ag, Cu, Fe, Py, Al, Co, Pb, Cr. Typical growth rates achieved in the system are in the order of 1 Å/min. The systems pressure during deposition usually does not rise above 1×10^{-6} mbar. The growth rate is monitored by means of QCM. Substrate cleaning can be conducted by Ar^+-ion milling system similar to the one installed in the MBE chamber. Two minicans with O_2- and Ar-gas (with purity 6N) are connected to the chamber (not shown in the drawing).

3.4. Atomic layer deposition system

The capacitor devices in which the VCMA is measured by means of MOKE in this thesis have and gating area in the order of 1 mm^2. For these type of devices it is crucial to have a transparent dielectric layer which allows for leakage-current-free gating. Al_2O_3 layers are used which are grown by the Savannah 100 ALD system. This system was commercially purchased and its installation was conducted in the frame of this thesis.

Images of the Savannah 100 system and its reactor are shown in figure 3.8(a) and (b). The system is equipped with a heatable manifold, where six different precursor gases can

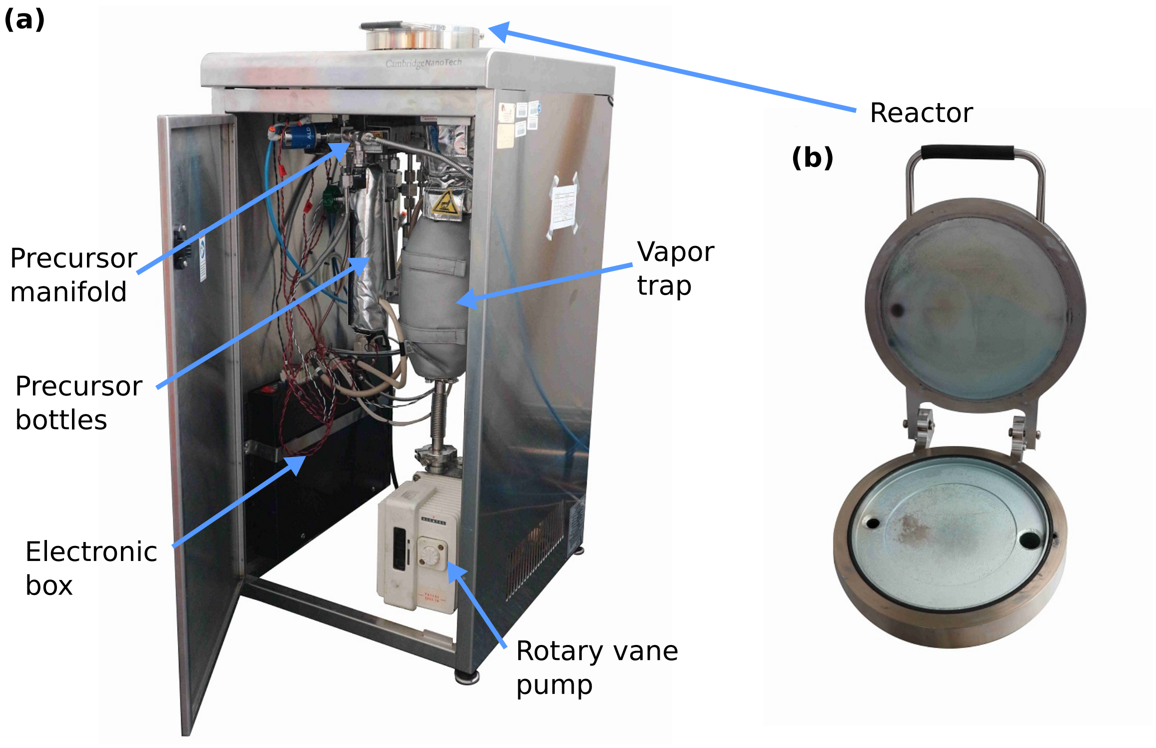

Figure 3.8.: Image of the Savannah 100 ALD (a) system and (b) reactor.

be attached to. The vacuum in the reactor chamber is produced by a rotary vane pump. Computer-controlled high speed valves are used to insert the precursor gases into the systems reactor. The reactor itself is capable of loading samples of wafers with a diameter of up to 100 mm. N_2 purging gas is introduced to the chamber via a computer controlled MFC.

In the following a typical ALD growth cycle is exemplified by the deposition of one layer of Al_2O_3:

1. The sample is loaded into the reactor which is then pumped down. The sample surface is already covered by OH groups formed by hydroxylation, which happens naturally while the sample is exposed to atmosphere.

2. Trimethylaluminium (TMA) precursor is pulsed into the reaction chamber where it reacts with the OH groups on the sample surface. This process forms a self passivating $AlO(CH3)_2$ layer.

3. Unreacted TMA and methane reaction product are pumped from the system.

4. Water is pulsed into the reaction chamber. The water removes all CH_3 groups on the sample surface and leaves a Al-OH layer. Between the Al atoms Al-O-Al bridges are introduced. Thus a self passivating layer of Al_2O_3 has been formed.

5. Unreacted water and methane reaction product are pumped from the system.

By successively repeating steps one to four, Al_2O_3 is grown in a LBL fashion. In contrast to sputter deposition or chemical vapor deposition (CVD), there is no need of constantly monitoring the film thickness during growth, as the ALD process is a self-limiting chemical reaction which forms one monolayer for each process cycle. The total Al_2O_3 thickness can be simply evaluated by counting the cycle numbers, if the cycle thickness is known. Here the thickness of one cycle step is calibrated by microfabricating an Al_2O_3 step by means of e-beam lithography and lift-off and subsequently measuring its height by atomic force microscopy. For Al_2O_3 grown at 80 °C a calibration factor of 1.25 Å/cycle is yielded. The growth speed depends mainly on the transient time in between steps three/four and four/five. In order to increase the growth speed the reactor temperature can be heated up to 400 °C.

The breakdown field dependence on growth temperature, barrier thickness, gating area, and electrode material of Al_2O_3 layers prepared by the Savannah 100 system has been investigated by the precursor manufacturer [150], and furthermore in the frame of a Bachelor [151] and Diploma thesis [152]. These investigations show that the Savannah 100 system is capable of producing highly insulating Al_2O_3 barriers even in laterally extended capacitor devices. Following general advices for the fabrication of such barriers can be given:

- The growth temperature only has a small impact on the electric breakdown field [150, 151].
- Using a contact material with a thermal expansion coefficient which is matched to Al_2O_3 leads to barriers with slightly enhanced electric breakdown fields [151].
- The risk of an immediate electric short-curt depends on the cross sectional gating are and dielectric layer thickness [151, 152]. For an Al_2O_3 barrier embedded in Au contacts, with a gating area of 250 µm × 250 µm, the risk of an immediate short-cut is almost zero, if the barrier thickness exceeds 40 nm [151].
- The electric breakdown field slightly depends on the cross sectional gating area [151]. For insulating barriers embedded in Au contacts a breakdown field of approximately 0.5 V/nm can be expected for a barrier with an gating area of 250 µm × 250 µm [151]. For a barrier with an gating area of 50 µm × 50 µm an electric breakdown field in the area of approximately 0.7 V/nm is expected [151].

3.5. Magneto-optic Kerr effect setup

The magnetization curves discussed in this thesis are measured by means of MOKE. The basic measurement principle is as follows: A linear polarized laser beam is reflected from the surface of a magnetic sample. Due to the MOKE the polarization state of the reflected light beam is altered. By plotting this change versus an external magnetic field the in-plane or out-of-plane magnetization curves are yielded. What kind of magnetization curve

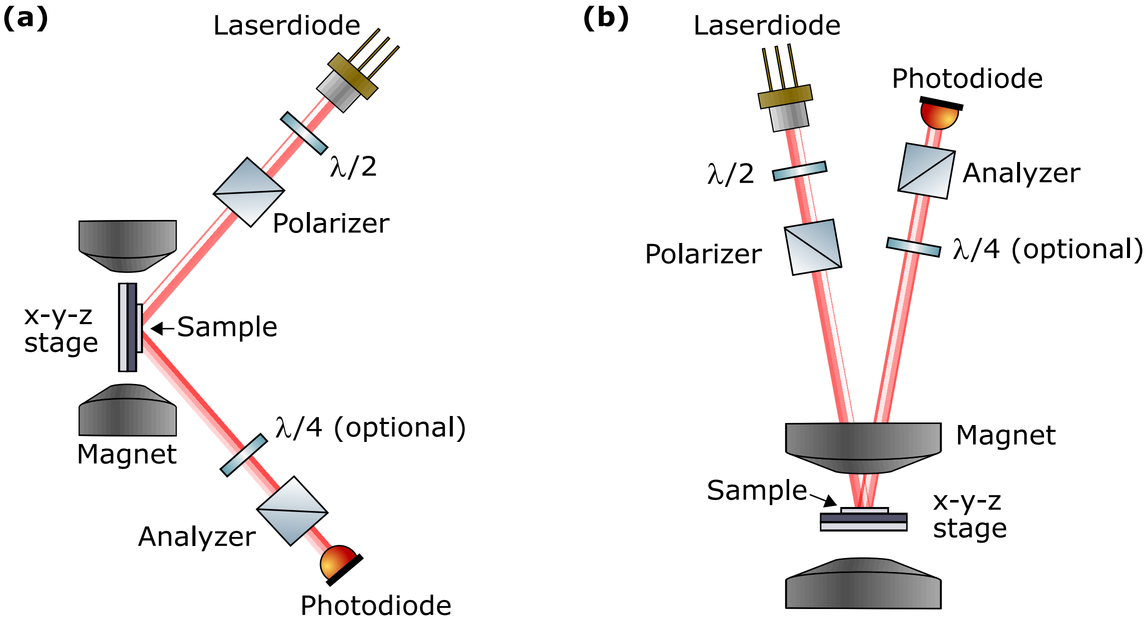

Figure 3.9.: Illustration of the MOKE setup in (a) longitudinal and (b) polar configuration, respectively.

is obtained depends on the geometrical configuration of the setup and the equilibrium magnetization orientation of the sample. These conditions are specified in the ongoing text. As the lateral resolution of the MOKE setup is only restricted by the spot size of the laser beam (which in principle is only diffraction limited), this technique allows to investigate thickness dependent magnetic properties on wedge type samples.

An illustration of the MOKE setup in longitudinal and polar configuration, used to measure the in- and out-of-plane magnetization curves discussed in this thesis, is shown in figure 3.9(a) and (b), respectively. As light source a 671 nm laser diode with an spectral density of 10 nm is used. The polarizer and analyzer are both Glan-Thompson type. A $\lambda/2$-waveplate in combination with the Glan-Thompson polarizer is used as beam attenuator. The (optional) $\lambda/4$-waveplate allows to measure both θ_K and ϵ_K [153]. The intensity of the reflected light beam I passing the analyzer is measured by an amplified semiconductor photodiode as voltage $U^\mathrm{pd} \sim I$. The magnetic field is provided by an electromagnet with Fe yoke which is supplied by a Kepco power supply. The field is measured by a Hall sensor mounted on one of the Fe pole pieces. In both configurations, depending on the pole pieces separation, field values of up to 2 T can be generated.

The setup in longitudinal configuration is used to measure the in-plane magnetization curves. Here the magnetic field is parallel to both the sample surface and the plane of incidence of the laser beam. The angle of incidence is 45° with respect to the sample surface. In this configuration in principle both the LMOKE and PMOKE contribute to U^pd measured in dependence of an external field. Thus only for an in-plane equilibrium magnetization the U^pd vs field plot reveals the in-plane magnetization curve of the sample.

For samples with PMA the U^{pd} vs field plot is a combination of both the in- and out-of-plane magnetization components and untangling this signal is a cumbersome task [132, 154].

In polar configuration the magnetic field is aligned perpendicular to the sample surface and the angle of incidence is close to normal (below 4°). In this configuration in any case (both in- or out-of-plane equilibrium magnetization orientation) the PMOKE dominates the measured signal [140] and thus the U^{pd} vs. field plot always yields the out-of-plane magnetization curve.

Quantitative measurement of the Kerr rotation and ellipticity

The magnetization curve in principle is given by the U^{pd} vs field plot. However, in some cases it is valuable to quantitatively measured the MOKE, i.e. determine the θ_{K} (or ϵ_{K}) vs. field plot. By properly setting the experiment conditions, θ_{K} (or ϵ_{K}) can be calculated from U^{pd}. This procedure is explained in the following.

It is assumed that the incoming light beam is s-polarized. The MOKE then induces a small p-polarized field component E_{p} in the reflected light beam. The analyzer and polarizer are set at a small angle δ away from full extinction. In the small angle approximation I arriving at the setup photodiode is written as

$$I = |E_{\mathrm{s}}\mathrm{sin}\delta + E_{\mathrm{p}}\mathrm{cos}\delta|^2 \approx |E_{\mathrm{s}}\delta + E_{\mathrm{p}}|^2. \tag{3.3}$$

Inserting $E_{\mathrm{p}}/E_{\mathrm{s}} = \theta_{\mathrm{K}} + i\epsilon_{\mathrm{K}}$ [153] into equation 3.3, leads to

$$\theta_{\mathrm{K}} = \left(\frac{I}{I_0} - 1\right)\frac{\delta}{2}, \tag{3.4}$$

where $I_0 = |E_{\mathrm{s}}|^2\delta^2$, is the intensity at the photodiode where no magnetic field is applied. Under experimental conditions U^{pd} is affected by incoherent contributions $U^{\mathrm{pd}}_{\mathrm{b}}$. Thus I described by equation 3.3, which is considered to yield only the variations induced by the MOKE, is related to U^{pd} via

$$I = U^{\mathrm{pd}} - U^{\mathrm{pd}}_{\mathrm{b}}, \tag{3.5}$$

The incoherent contribution $U^{\mathrm{pd}}_{\mathrm{b}}$ is experimentally determined from the photodiode signal measured where the setup analyzer and polarizer are set to extinction. Inserting equation 3.5 in equation 3.4 leads to

$$\theta_{\mathrm{K}} = \left(\frac{U^{\mathrm{pd}} - U^{\mathrm{pd}}_{\mathrm{b}}}{U^{\mathrm{pd}}_0 - U^{\mathrm{pd}}_{\mathrm{b}}} - 1\right)\frac{\delta}{2} \tag{3.6}$$

where U^{pd}_0 is the photodiode amplifier voltage measured at zero field. It is shown, that by inserting a $\lambda/4$-waveplate into the optical path of the MOKE setup before the analyzer, ϵ_{K}

instead of θ_K is yielded by the right side of equation 3.6, for otherwise identical experimental conditions [153].

3.6. Modified magneto-optic Kerr effect setup in polar configuration

The modified MOKE setup in polar configuration allows to measure the VCMA in two different manners. In a static manner, the change of the effective out-of-plane MA constant ΔK_{eff} is extracted from the area enclosed by the out-of-plane magnetization curves measured for two different gate voltages U_g. In the second manner, a technique is employed which is first described by Maruyama et al. [6]: The gate voltage U_g is modulated by a frequency generator with the frequency f_M and the VCMA induced change of the MOKE signal is measured by lock-in amplifier. Sweeping an external magnetic field and plotting it versus the lock-in signal yields the *modulation curves.* Here this technique is refined to measure the difference in Kerr rotation $\Delta\theta_K$ (or ellipticity $\Delta\epsilon_K$). It will be shown that ΔK_{eff} can be extracted from the $\Delta\theta_K$ vs field plot.

Setup and sample layout

A scheme of the modified MOKE setup in polar configuration is shown in figure (a) where the modification used to measure the VCMA in a static manner are shown in figure 3.10(a') and the modification needed to measure the modulation curves are shown in figure (a").

Figure 3.10(b) shows a scheme of the sample layout. The key element of this design is the use of a semi-transparent top gate which allows to measure the MOKE response while gating. The top gate layer is contacted by means of a needle probe tip with a tip diameter of 2 µm. The bottom electrode is common to all devices and is contacted by wire bonding. More details on the sample microfabrication and electrical contacting are given in section 4.2. In the following U_g is defined with respect to the top gate, i.e. negative voltages cause electron depletion in the magnetic layer at the magnet/dielectric interface.

Quantitatively measurement of the voltage induced change in Kerr rotation and ellipticity

Figure 3.10(c) illustrates out-of-plane magnetization curves measured at a positive and negative U_g, respectively, assuming that the sample is in-plane magnetized at equilibrium and that electron depletion in the magnetic layer at the magnet/dielectric interface leads to an increase of PMA. In figure 3.10(d) the modulation curve is illustrated which is measured on the same sample while modulating the gate voltage in between $\pm U_g$. It is further assumed that the phase relation at the lock-in amplifier sets the initial state at U_g. The photodiode

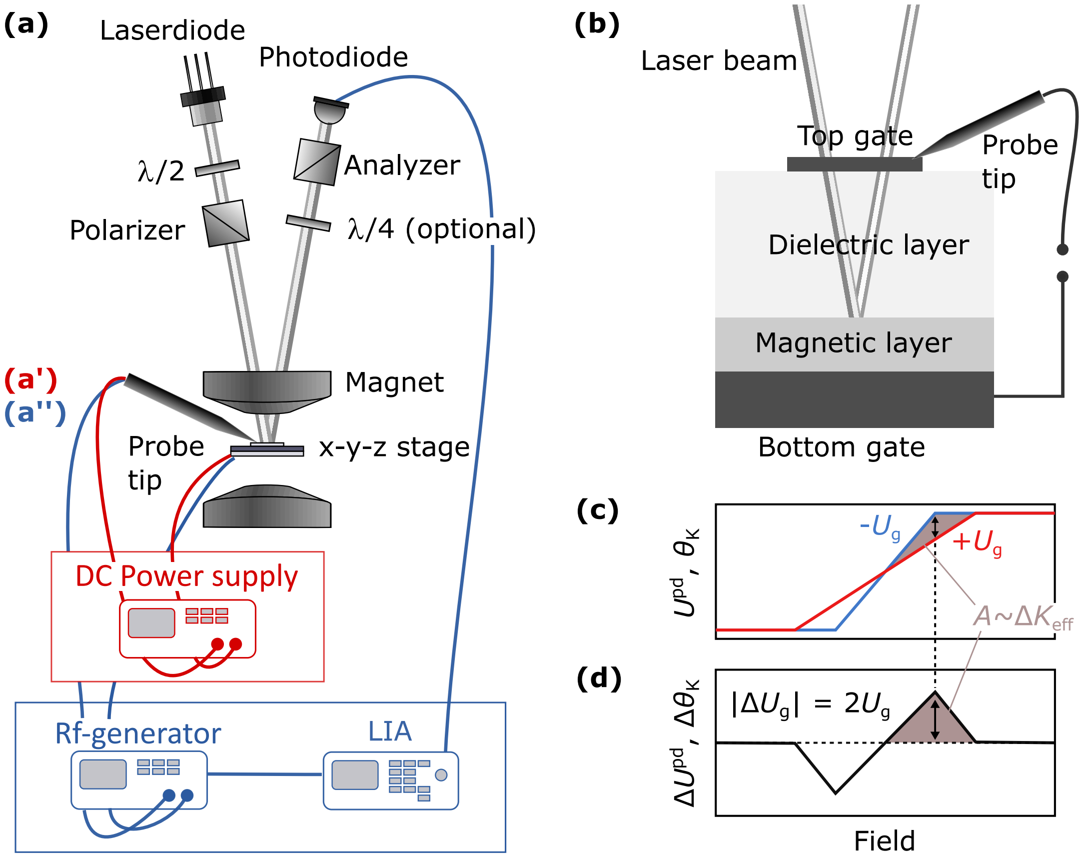

Figure 3.10.: (a) Illustration of the modified MOKE setup in polar configuration where the VCMA is measured employing two different methods. The measurement scheme for static measurements of VCMA is indicated by (a') whereas for modulated measurements (a'') is used. In both cases U_g is applied to the capacitor devices by a needle probe tip with a tip diameter of 2 µm. (b) Illustration of the capacitor devices. Figure (c) shows a schematic representation of the expected out-of-plane magnetization curves for positive and negative U_g applied to a magnetic film with in-plane equilibrium magnetization orientation. Figure (d) shows the curve which is expected to be measured by the modulation technique while modulating the gate voltage in between positive and negative U_g.

signal ΔU^{pd} measured via the lock-in amplifier is then written as

$$\Delta U^{pd} = U^{pd,-} - U^{pd,+}, \tag{3.7}$$

where $U^{pd,\pm}$ is the photodiode signal measured in a static fashion where positive and negative U_g are apllied, respectively. Inserting equation 3.6 into equation 3.7 one gets

$$\Delta\theta_K = \frac{\Delta U^{pd}}{U_0^{pd} - U_b^{pd}} \frac{\delta}{2}. \tag{3.8}$$

It is assumed that the same experimental conditions are employed which are used to measure the θ_K vs field plot in the static setup (see section 3.5). Equation 3.8 allows one to calculate the $\Delta\theta_\mathrm{K}$ vs. field relation from the ΔU^pd vs. field relation. The quantities U_0^pd and U_b^pd hereby have to be measured in a static fashion, as described in section 3.5. It is important that the exact same experimental conditions are employed in both the static determination of U_0^pd and U_b^pd and the actual modulation measurements, as deviations of the experimental conditions can impact $\theta_\mathrm{K,s}$, see section 2.6. By inserting a $\lambda/4$-waveplate into the optical path of the setup prior to the analyzer, $\Delta\epsilon_\mathrm{K}$ is determined by the right side of equation 3.8 [153].

Measuring the voltage induced change of the out-of-plane effective MA constant via the modulation technique

According to the area method the change in effective MA constant ΔK_eff is directly related to the area A, as shown in figure 3.10(c) and (d). In the following it is shown that extracting the area A from the $\Delta\theta_\mathrm{K}$ (or $\Delta\epsilon_\mathrm{K}$) versus field plot measured with the modulation technique allows to quantitatively determine ΔK_eff.

In this thesis ΔK_eff is defined by:

$$\Delta K_\mathrm{eff} = K_\mathrm{eff}^\mathrm{f} - K_\mathrm{eff}^\mathrm{i} \tag{3.9}$$

Where $K_\mathrm{eff}^\mathrm{f,i}$ are the effective MA constant in the final and initial gating state, respectively. Equation 3.9 yields positive ΔK_eff if the initial U_g is higher than the final U_g for systems where electron depletion in the magnetic layer at the magnet/dielectric interface leads to an increase in PMA (typically observed in Fe/MgO bilayers [6]). Inserting equation 2.24 into equation 3.9 one gets

$$\Delta K_\mathrm{eff} = \mu_0 M_\mathrm{s}\left(\frac{1}{\theta_\mathrm{K,s}^+}\int_0^{\theta_\mathrm{K,s}^+} H^+\mathrm{d}\theta_\mathrm{K} - \frac{1}{\theta_\mathrm{K,s}^-}\int_0^{\theta_\mathrm{K,s}^-} H^-\mathrm{d}\theta_\mathrm{K}\right). \tag{3.10}$$

Here "±" symbolizes that the quantities are measured at positive and negative U_g. Under the assumption, that the U_g dependence of $\theta_\mathrm{K,s}^\pm$ is negligible[1] and thus setting $\theta_\mathrm{K,s}^+ \approx \theta_\mathrm{K,s}^- := \theta_\mathrm{K,s}$ in equation 3.10, one writes

$$\Delta K_\mathrm{eff} = \mu_0 \frac{M_\mathrm{s}}{\theta_\mathrm{K,s}}\int_0^{\theta_\mathrm{K,s}} (H^+ - H^-)\mathrm{d}\theta_\mathrm{K} = \frac{M_\mathrm{s}}{\theta_\mathrm{K,s}} A. \tag{3.11}$$

Equation 3.11 states that ΔK_eff can be calculated by extracting the area A from the $\Delta\theta_\mathrm{K}$ vs field plot measured with the modulation technique by normalizing it to $\theta_\mathrm{K,s}$. Here $\theta_\mathrm{K,s}$ has to be determined from the static out-of-plane magnetization curve. The derivation of equation 3.11 can be conducted in the same manner by interchanging θ_K and ϵ_K.

---

[1] Indeed a small dependence of $\theta_\mathrm{K,s}^\pm$ on U_g is found in the samples investigated in this these. Details are discussed in section 4.5. However, the effect is very small, such that the here made assumption is justified.

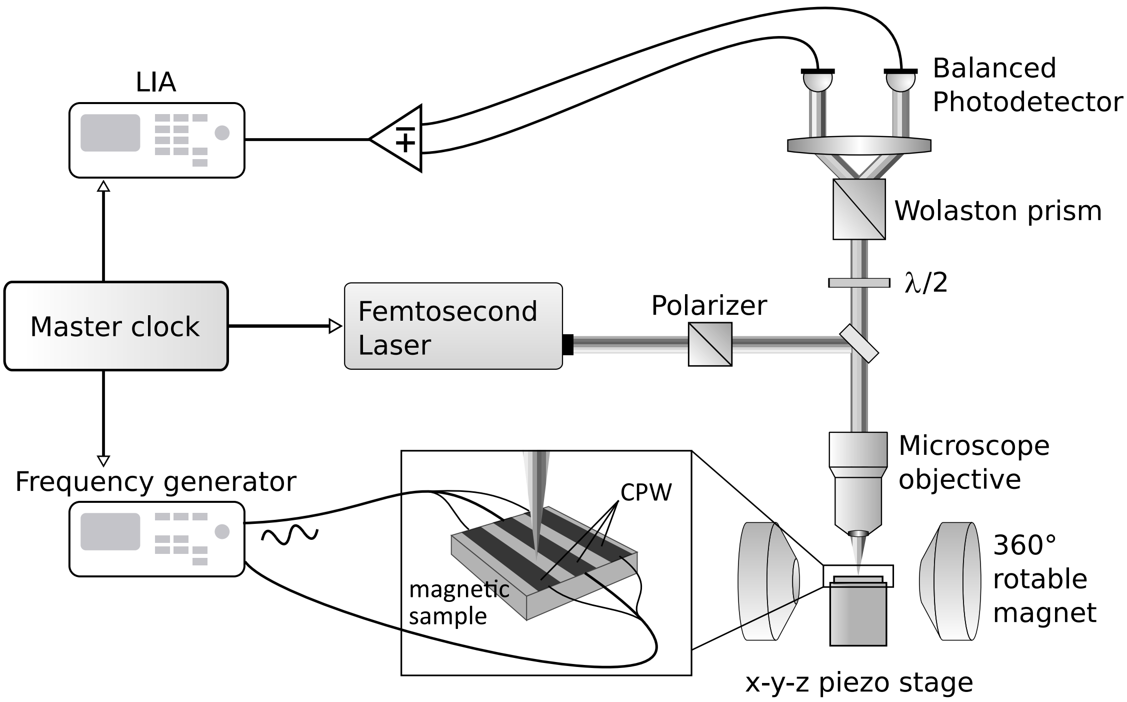

Figure 3.11.: Schematics of the scanning TR-MOKE setup used to measure FMR.

3.7. Time-resolved MOKE setup

In the time-resolved MOKE (TR-MOKE) setup the FMR of a ferromagnetic film excited by a microwave field can be measured by probing the magnetization precession amplitude in a stroboscopic manner via the MOKE while sweeping an external (static) magnetic field.

An illustration of the TR-MOKE setup utilized to measure the FMR spectra discussed in this thesis is shown in figure 3.11. In this setup the out-of-plane component of the magnetization vector is probed via the PMOKE by a linear polarized light pulse with a wavelength of 510 nm and a pulse duration of 100 fs, working at a repetition rate of 80 MHz, which is focused onto the sample surface through a high numeric aperture objective microscope. The magnetization dynamics of the ferromagnetic sample is excited by a microwave field generated by a microfabricated CPW, see figure 3.11. A well defined phase relation between microwave field and the laser probe pulse is ensured by the master clock which synchronizes both the frequency generator (connected to the CPW) and the laser repetition rate[2]. Static magnetic fields of up to 300 mT can be applied inside the sample plane at arbitrary azimuthal angles.

After reflection from the sample, the laser pulse passes a Wollaston prism which splits the beam into two orthogonal polarized components. The magnitude of these two components is then detected as voltage U_A and U_B by a balanced photodetector. With a $\lambda/2$-plate

---

[2] The repetition rate of the laser is continuously monitored internally by means of a fast photoswitch and compared to the master clock. Any drift in the repetition rate is countered by adjusting the cavity length of the laser.

installed prior to the Wollaston prism the polarization of the reflected light beam is adjusted such that the difference signal $U_\mathrm{A} - U_\mathrm{B}$ is zero whenever the sample has no out-of-plane magnetization component. The difference signal is normalized to the sum signal $U_\mathrm{A} + U_\mathrm{B}$, which makes the TR-MOKE signal

$$A_\mathrm{TM} = \frac{U_\mathrm{A} - U_\mathrm{B}}{U_\mathrm{A} + U_\mathrm{B}}, \tag{3.12}$$

independent of any variations in the laser intensity. The A_TM vs. field plot, measured at fixed microwave field frequency f and field orientation then in principle yields the FMR spectra.

In order to improve the signal to noise ratio the so called undersampling or Super-Nyquist sampling method is employed. With this technique f is set such, that it deviates by a small frequency ϵ from being an integer multiple of the 80 MHz laser repetition rate. Consequently A_TM oscillates slowly with an oscillation frequency of exactly ϵ and can be detected via a LIA. The correct phase relation between the LIA detection frequency and ϵ is ensured by synchronizing the LIA with the master clock.

The A_TM vs. field relation measured at a fixed f (and field orientation) in general is a mixture of the real and imaginary part of the susceptibility tensor element χ_ww (see section 2.5). Thus, the function used to fit the A_TM vs. field dependency is given by the sum of a symmetric and anti-symmetric Lorentzian, and a constant and linear term:

$$A_\mathrm{TM}(H)\Big|_{f=\mathrm{const.}} = A\frac{(H - H_\mathrm{FMR})\cos(\Theta) + \Delta H \sin(\Theta)}{(H - H_\mathrm{FMR})^2 + \Delta H^2} + C_1 H + C_2, \tag{3.13}$$

Here A is the FMR spectra amplitude, Θ is the mixing angle and $C_{1,2}$ are the constants describing the erroneous contributions to the measured signal. The contribution linear in field, $C_1 H$, can be caused for example by a field dependent drift of the sample holder, or field dependent strain in the objective lens which, due to birefringences rotates the polarization plane of the reflected laser pulse. The constant term C_2 is caused by microwave field induced non-magnetic contributions to the TR-MOKE signal. The mixing angle Θ depends on the phase relation between the laser pulse and the microwave excitation field [155].

4. Voltage control of magnetic anisotropy in MgO/Fe/Au

In this chapter the results on the VCMA investigated in epitaxial MgO/Fe/Au structures with Fe thickness d_{Fe} ranging from 0 nm to 1 nm are presented. The chapter has six parts. In the first part the epitaxial growth of the multilayers is described. From the prepared structures two type of devices are microfabricated. These devices allow to investigate the magnetic and VCMA properties of the ultrathin Fe layers in the modified MOKE setup and in the TR-MOKE setup. The microfabrication is presented in the second part of this chapter. In the third part the magnetic properties of the Fe layers are discussed. Then the VCMA properties of the Fe layers are presented. In particular the dependence of the VCMA on the gating time, the U_{g} magnitude and d_{Fe} is investigated. The results of these investigation are discussed in the fourth, fifth and sixth part of this chapter, respectively. Finally, in part seven the VCMA induced modification of the FMR position is discussed.

4.1. Epitaxial growth

Figure 4.1 shows a cross sectional carton of the prepared epitaxial multilayer structures. Two samples with nominal same layout are grown by MBE in the UHV system described in section 3.1. In the first sample the Fe layer is a continuous wedge (CW) sample with d_{Fe} ranging from 0 nm to 1 nm. In the second sample, the Fe layer consists of a step wedge (SW) sample with two plateaus where d_{Fe} is 0.55 nm and 0.40 nm, respectively. In the following six parts of this subsection the substrate preparation and the epitaxial growth of each layer is described in detail. The quality of the epitaxial preparation is discussed with respect to the RHEED observations.

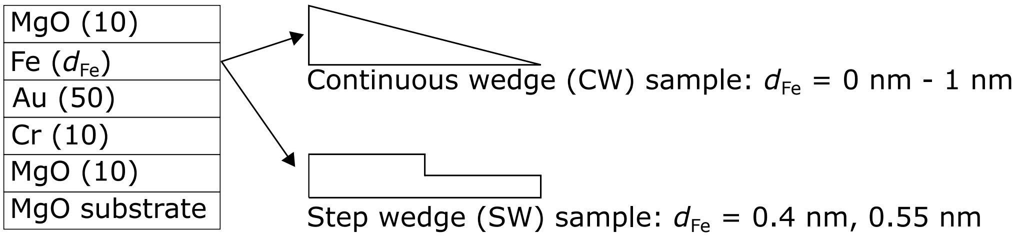

Figure 4.1.: Cross sectional cartoon of the epitaxial multilayer structure grown by MBE. The numbers in brackets are thicknesses in nanometres.

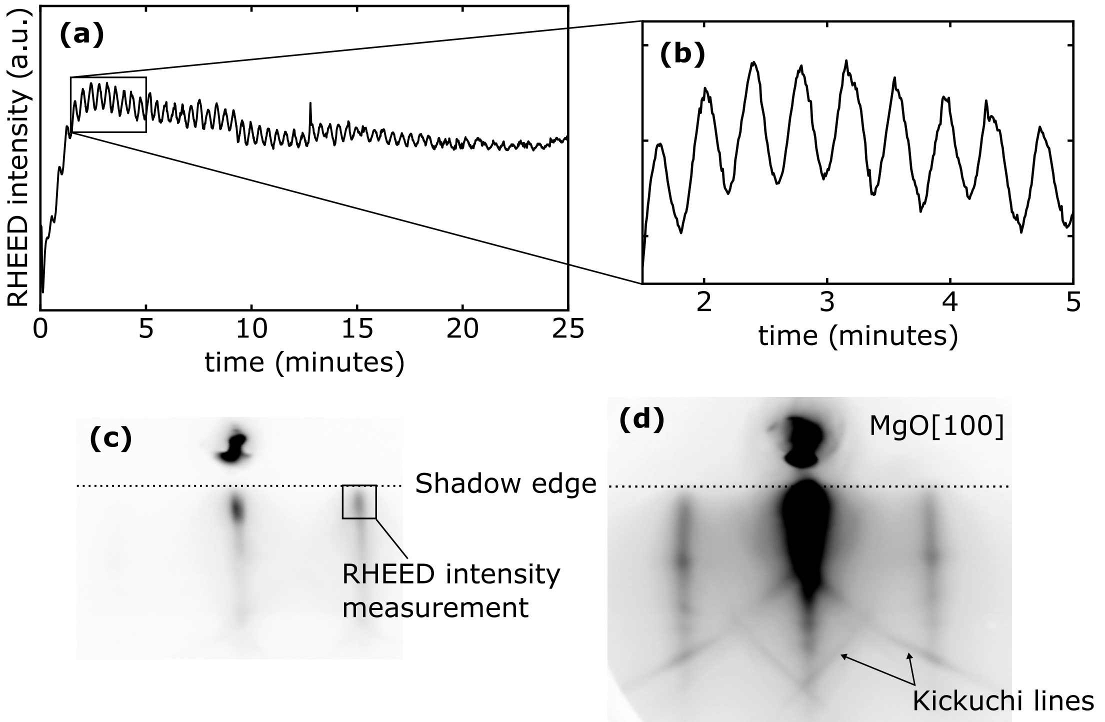

Figure 4.2.: RHEED analysis of the MgO buffer layer growth. (a) RHEED intensity oscillation. (b) Magnified view on the RHEED oscillations. (c) RHEED pattern of the MgO(001) surface before growth. Here the electron beam is slightly misaligned from the MgO[100] direction in order that the specular and (01) spot are aligned on a horizontal line. In this configuration RHEED oscillations are observed by measuring the intensity of the (01) diffraction spot. (d) RHEED pattern of the 10 nm MgO buffer layer where the electron beam is oriented along the [100] direction.

4.1.1. MgO(001) substrat preparation

Commercial available MgO crystals with a (001) surface orientation are used as substrates. The substrate area is 5 mm × 10 mm and the thickness 0.5 mm. Two of these substrates are prepared at the same time.

As a first step, the substrate is outgassed in the load lock of the MBE system where all water accumulated in the hygroscopic MgO is desorbed [1, 3, 156, 157]. Here the heating filament power is set to 100 W yielding an estimated sample temperature of 650 °C. After annealing, the transfer into the MBE chamber is conducted. The annealing step alone is not sufficient in order to prepare a clean MgO surface as carbon impurities can still be present [156, 158]. Thus a 10 nm thick MgO buffer layer is deposited next. The growth is conducted by electron evaporation at a rate of 2.5 ML/min where the substrate is held at room temperature. During the deposition p rises to 2×10^{-9} mbar. Most likely this increase in p is caused by an increase in molecular oxygen [4, 159, 160] which is formed at the steel walls of the vacuum system [160] through a recombination of atomic oxygen, which is part of the molecular flux emitted from the electron beam evaporator. During the

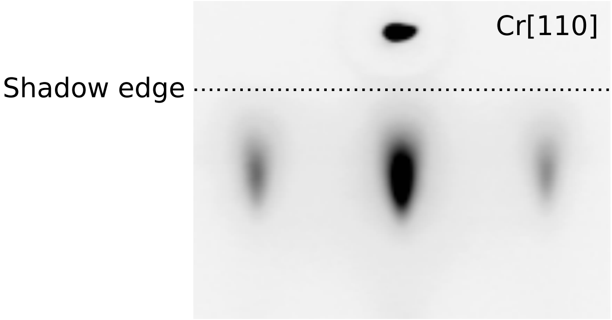

Figure 4.3.: RHEED pattern of 10 nm Cr grown on the MgO buffer layer. The electron beam is oriented along the Cr[110] direction.

buffer preparation around 50 RHEED oscillations are observed, see figure 6.2(a) and (b). The oscillations are recorded by measuring the intensity of the (01) diffraction spot, where the sample is slightly rotated from the exact MgO[100] orientation, making specular and (01) spot parallel to the shadow edge. Furthermore the angle between incident electron beam and sample surface is set to the first anti-Bragg condition at 0.83°. An image of the respective RHEED pattern is shown in figure 6.2(c). The here observed pronounced oscillations indicate the excellent LBL growth where the damping most likely is not related to surface roughening. For the homoepitaxial growth of MgO no lattice relaxation transition should occur. Thus the oscillation damping is attributed to a transition from the LBL to the step flow growth mode [148, 149], resulting in a perfectly flat MgO buffer surface. Figure 6.2(d) shows the RHEED pattern of the 10 nm thick MgO buffer where the electron beam is oriented along the [100] direction. The streaky 1×1 pattern confirms the smooth MgO surface. The Kikuchi lines visible here are a common feature observed in the RHEED pattern of crystal surfaces and are attributed to inelastic scattering events [124, 142, 144].

4.1.2. Cr seed layer

The direct growth of Au onto a MgO(001) surface usually leads to a polycrystalline ordering with preferentially (111) surface orientation [161]. The LBL growth of Au has been reported by using the (001) surface of an in-situ cleaved MgO crystal as template [161, 162]. However, no apparatus which allows for in-situ cleaving of crystals is installed in the used MBE system and thus the above described method is not applicable here. Instead a 10 nm thick Cr seed layer is employed which is also reported to lead to the LBL growth of subsequently deposited Au [82, 158].

The crystal structure of MgO is face centered cubic (fcc) with a lattice constant of 4.22 Å. Cr has a body-centered cubic (bcc) lattice structure with a lattice constant of 2.89 Å. The expected epitaxial relation between a Cr film prepared onto a MgO surface is Cr[100]||MgO[110]. In this configuration η is 2.9 %. The 10 nm thick Cr layer is deposited by RTE at a growth rate of 2 ML/min where the sample is held at room temperature. During growth p is $\sim 5 \times 10^{-10}$ mbar. Figure 4.3 shows the RHEED pattern of the 10 nm

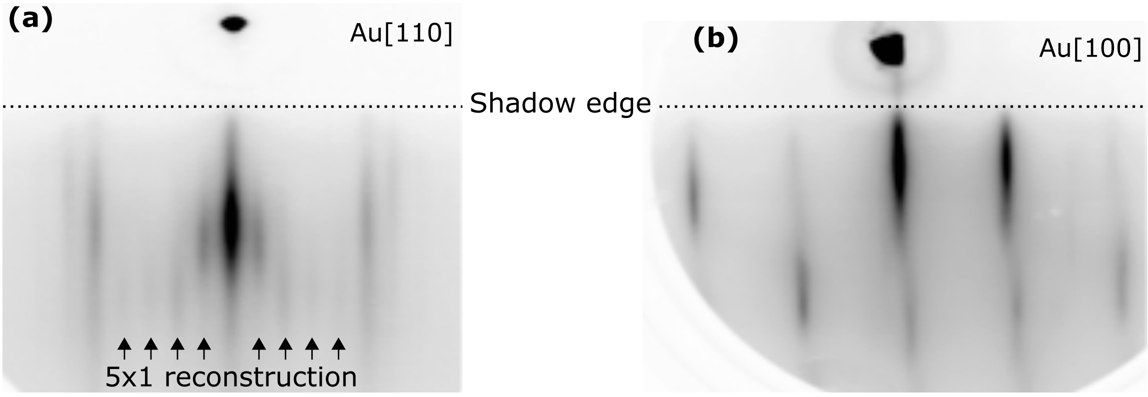

Figure 4.4.: RHEED pattern of 50 nm Au where the electron beam is (a) oriented along the Au[110] and (b) along the Au[100] direction.

thick Cr film surface where the electron beam is oriented along the [110] direction. The spotty pattern indicates a mono crystalline but rather rough 3D surface. In principle, one could would expect an improved surface morphology of the Cr layer for a deposition at elevated temperatures or by the conduction of a post deposition annealing step [1, 2, 29, 163]. However, the surface properties of the Cr seed layer achieved here are sufficient to produce a high quality, flat Au surface with (001) orientation as shown in the following.

4.1.3. Au buffer layer

Next the 50 nm thick Au buffer layer is prepared. The almost perfect surface of this layer is later used as template for the ultrathin Fe films. Furthermore the relatively thick Au buffer ensures a good electrical conductivity of the bottom electrode which is needed for the VCMA experiments.

Au has fcc structure with a lattice constant of 4.08 Å. The resulting epitaxial relation during preparation upon the Cr(001) surface is Au[100]$\|$Cr[110] [82, 158]. In this configuration an almost perfect lattice matching is yielded with an η of only 0.2 %. The Au film is prepared at a growth rate of 1.5 ML/min by RTE where the sample is at room temperature. The MBE chamber p rises to 2×10^{-9} mbar during deposition, probably caused by N_2 outgassing of the pyrolytic boron nitride crucibles. After growth an annealing step is conducted for 40 min. Here, the heating lamp power is set to 15 W which leads to an estimated sample temperature of 200 °C. Figure 4.4(a) shows the RHEED pattern of the Au surface after annealing, where the electron beam is oriented along the [110] direction. The four streaks appearing in between the main (1×1) pattern clearly show the Au (5×1) surface reconstruction [29, 158]. The observation of these reconstructions indicates that here a very good surface quality with low roughness is achieved.

Figure 4.4(b) shows the RHEED pattern where the electron beam is oriented along the Au[100] direction. A slight tilt and shift of the diffraction streaks is observed, as indicated by the dotted lines, indicating a vicinal sample surface [145]. The vicinal surface most

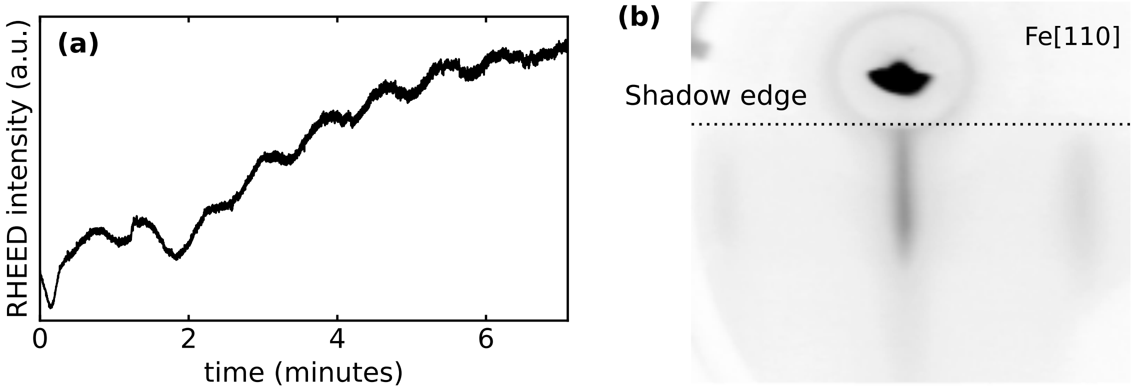

Figure 4.5.: (a) RHEED intensity oscillations recorded during the growth of the Fe marker area. (b) RHEED pattern of the Fe marker area recorded at a film thickness of 2 nm. Here, the electron beam has an energy of 10 keV and is oriented along the Fe[110] direction.

likely is attributed to the commercial purchased MgO substrates where such kind of surface configuration is expected from the polishing procedure [144].

4.1.4. Ultrathin Fe wedge

Next the ultrathin Fe wedge is prepared. The Fe wedges of both the CW and SW sample are prepared by moving a computer controlled shutter underneath the sample during the Fe evaporation. Prior to the wedge deposition, a marker area with a d_{Fe} of 5 nm is prepared at the edge of the sample. This area, visible by eye, is later used to determine the wedge starting point. The wedge slope is calculated from the ratio of shutter speed and growth rate.

Fe has bcc structure with a lattice constant of 2.87 Å. The resulting epitaxial relation upon growth on the Au(001) surface is Fe[100]||Au[110]. This configuration results in a very small η of only 0.6 %. The growth here is conducted by RTE at a growth rate of 1.4 ML/min where the sample is at room temperature. During evaporation the chamber pressure is in the (low) 1×10^{-10} mbar region. RHEED intensity oscillations are observed during the marker area deposition, see figure 4.5(a), showing the initial LBL growth. The oscillations are measured as intensity variations of the specular spot where the electron beam incident angle is set to the first anti Bragg condition at 1.2 %. The damping of the oscillations most likely is caused by a transition from the LBL towards the 3D growth mode with increasing d_{Fe} [164, 165]. However, the observation of RHEED oscillations clearly indicates a smooth Fe surface. This assumption is further confirmed by the streaky RHEED pattern observed on the marker where the Fe film thickness is 2 nm, see figure 4.5(b).

In any case it is quite surprising that the LBL growth of Fe on Au can be achieved. Despite the very good lattice matching, a clear 3D growth is expected from the relation of their γ_{s} values: $\gamma_{\mathrm{Fe}} = 2.9$ J/m^2 and $\gamma_{\mathrm{Au}} = 1.4$ J/m^2 [166]. It is well accepted that the LBL growth is promoted by a thin Au layer (in the order of 1 ML) which is known to segregate

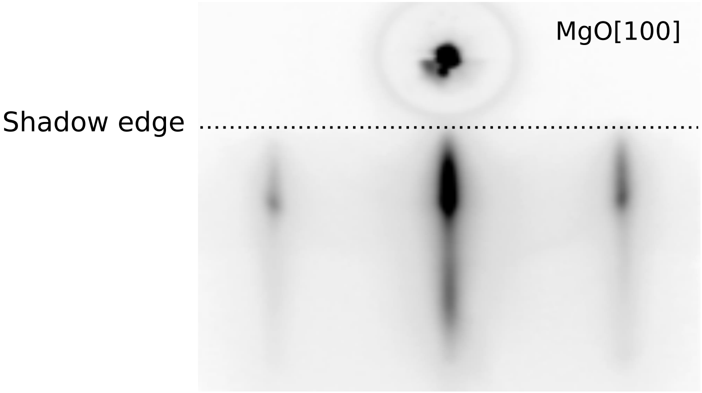

Figure 4.6.: RHEED pattern of the 10 nm thick top dielectric MgO layers surface where the electron beam is oriented along the MgO [100] direction.

to the surface of the growing Fe layer there acting as surfactant by lowering the total free energy of the system [167–171]. The exact amount of segregated Au has been reported to depend on d_{Fe} [172, 173] and the sample temperature during growth [174, 175]. An increasing amount of Au is reported for higher sample temperatures [174, 175]. Here room temperature growth is employed in order to reduce this effect. Any amount of Au located at the interface of the Fe/MgO bilayer is expected to significantly influence the VCMA in the metallic system due to its very short screening length [54, 58].

4.1.5. MgO dielectric layer

Finally, the 10 nm thick top dielectric MgO layer is prepared. This layer serves as primary dielectric in the later microfabricated capacitor devices, see section 4.2, where charging/discharging the Fe interface upon application of a gate voltage is expected to induce the VCMA.

The epitaxial relation of MgO prepared onto a Fe(001) surface is MgO[100]||Fe[110]. In this configuration the lattice mismatch is 3.8 %. The MgO layer here is deposited by electron beam evaporation where the sample is held at room temperature. The growth rate is set to 2.5 ML/min. During deposition the pressure rises to the low 10^{-9} mbar due to an increase of molecular oxygen in the vacuum chamber as already described in the section 4.1.1. Here no clear RHEED oscillations could be observed. In principle the LBL growth mode is expected for the preparation of a MgO film onto a Fe(001) surface at room temperature [4, 176–180]. This growth mode is favored by the relation of γ_{s}: $\gamma_{\mathrm{MgO}} = 2.9\mathrm{J/m}^2$ [166], $\gamma_{\mathrm{Fe}} = 1.1\mathrm{J/m}^2$ [181]. However, RHEED oscillations only have been reported for the deposition of MgO onto a Fe(001) surfaces of superior quality [176, 177, 179]. As described in the last section the ultrathin Fe layer already is slightly roughened. Thus it might be not too surprising that here the RHEED oscillations could not be observed. A relatively smooth MgO surface is indicated by the streaky RHEED pattern observed along the [100] direction, see figure 4.6.

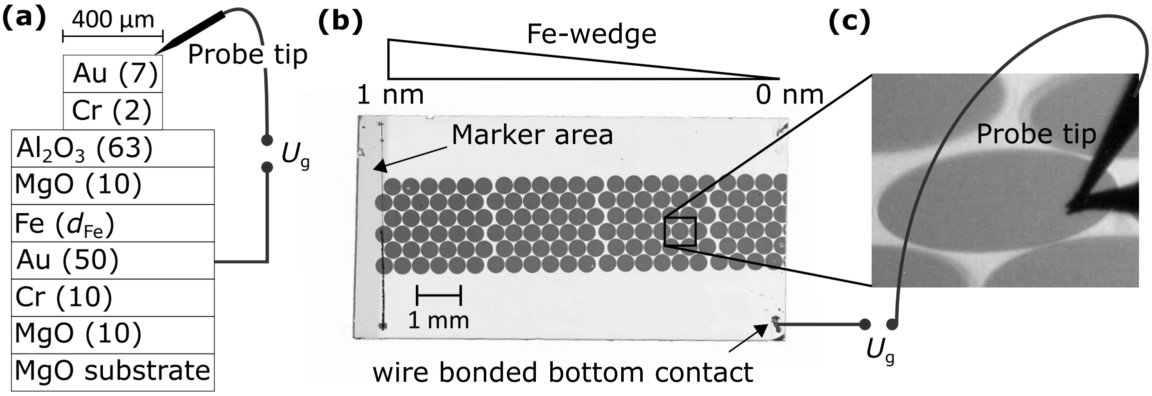

Figure 4.7.: MOKE (capacitor) devices used to measure the VCMA in the modified MOKE setup. (a) Cross-sectional cartoon showing the device layer structure. The numbers in brackets are thicknesses in nanometer. Top view optical microscope image of the CW sample with microfabricated devices. (c) Device with the probe tip in contact.

4.2. Sample devices

Two types of devices are microfabricated. The MOKE devices allows to measure the VCMA in the modified MOKE setup. The TR-MOKE devices allows to measure the FMR in the TR-MOKE setup, where optionally the VCMA can be probed. In the following two parts both devices are described in detail. The focus of this discussion lies on understanding the general device layout and functionality. A complete description of the devices microfabrication (by electron beam lithography, thermal deposition of metals, ALD, Ar^+-ion milling and lift-off technique) is given in the appendix B.

4.2.1. MOKE devices

The MOKE devices employed to measure the VCMA in the modified MOKE setup in principle are capacitors with semi-transparent top gate. A cross sectional cartoon of the capacitor layer structure is shown in figure 4.7(a). A Cr(2)/Au(7) bilayer, the number in brackets are thicknesses in nanometer, is used as top gates. Please note that the Cr is only employed as adhesion layer. The top gate bilayer thickness ensures a sufficiently high electric mobility while still being semi-transparent. The top gates are of circular shape with a diameter of 400 µm. The relatively large size of the capacitor devices needs for a further dielectric passivation. Even epitaxial grown MgO of superior crystalline quality is randomly peppered by pinholes which lead to shortening of capacitor or tunnel structures as soon as the gating area exceeds $\sim 1\,\mu m^2$ [182]. Here a 63 nm thick Al_2O_3 film placed in between the epitaxial MgO and the top gate layer is used as dielectric passivation layer.

Multiple capacitor devices are microfabricated on both the SW and CW sample. Figure 4.7(b) shows an optical microscope image giving a top view on the CW sample with microfabricated capacitor devices. The circles appearing in this image are the capacitors top gates. Here the capacitor structures are microfabricated along the Fe wedge. Thus the d_{Fe}

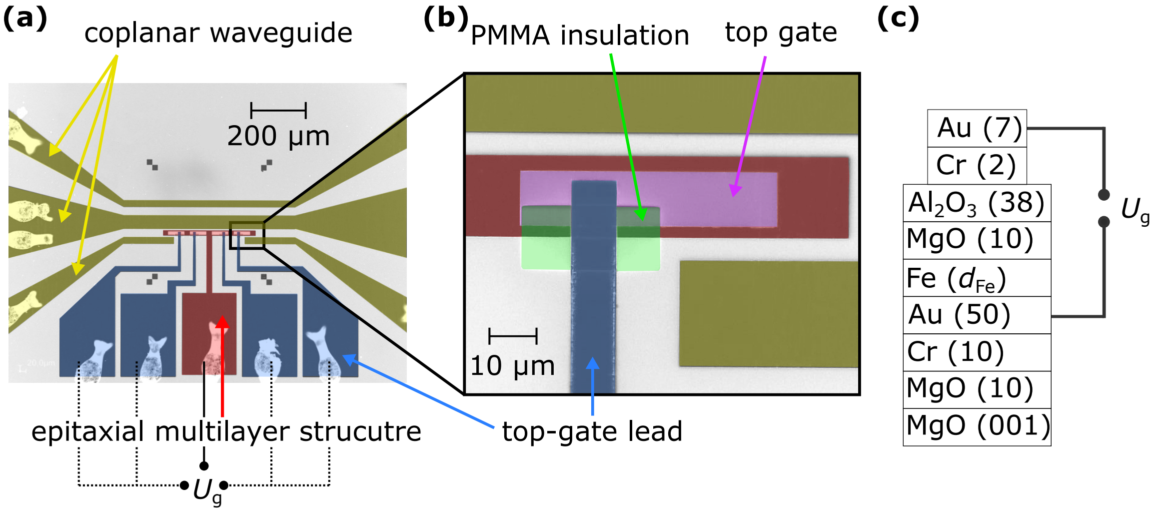

Figure 4.8.: (a) Top view optical microscope image of the microstructured TR-MOKE device. (b) Magnified view on the top gate area. (c) Cross sectional cartoon of the capacitor device layer structure. The numbers in brackets are thicknesses in nanometer.

dependence of the VCMA can be investigated. The electrical contacting of the samples is as follows.

A probe needle with tip diameter of 2 µm is placed on the top gate structure, as shown in figure 4.7(b). A common bottom contact is shared by all capacitor devices and is fabricated by Al wire bonding the sample at an area where no top gate is present. The Al wire passes through the dielectric MgO/Al_2O_3 bilayer and thus contacts the bottom Au buffer layer.

4.2.2. TR-MOKE devices

The TR-MOKE device in principle consists of a coplanar waveguide and an epitaxial multilayer structure which is placed in between the signal and the ground line. Four gates are microfabricated on top of the multilayer structure and allow to apply a U_g while measuring FMR. In total six TR-MOKE devices are microfabricated on the epitaxial grown CW sample where d_{Fe} is 0.40 nm, 0.51 nm, 0.61 nm, 0.72 nm, 0.83 nm and 0.94 nm. After fabrication these devices are separated by diamond saw cutting.

Figure 4.8(a) shows an optical microscope image of the 0.94 nm device where the coplanar waveguide (yellow), the epitaxial multilayer structure (red) and the top gate leads (blue) are visible. Figure 4.8(b) shows an optical microscope image of the area where one of the four top gates is placed. In this image the top gate (purple), the PMMA insulation structure (green) and the top gate lead (blue) are visible. Figure 4.8(c) shows a cross-sectional cartoon of the capacitor device layer structure. The layout is similar to the MOKE devices expect for a thinner Al_2O_3 passivation layer, as the effective gating area is smaller. The coplanar waveguide, the top gate and the bottom electrode are all contacted by Al-wire wedge bonding. All capacitor devices share a common bottom electrode, which is contacted

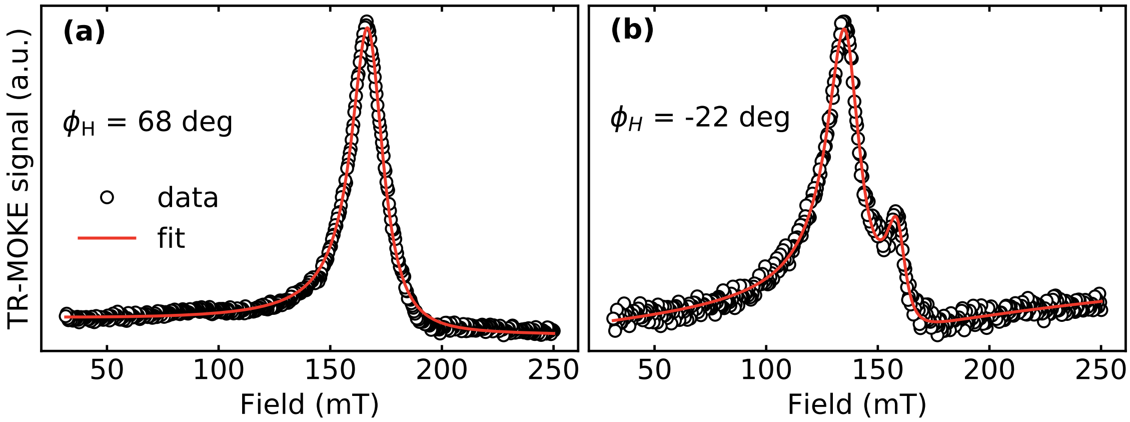

Figure 4.9.: FMR spectra measured on the 0.94 nm TR-MOKE device where the microwave frequency is 11.064 GHz and ϕ_H is (a) 68° and (b) $-22°$. The spectrum shown in figure (a) is well fitted by the Lorentzian function described by equation 3.13. The spectrum shown in figure (b) is fitted well by the sum of two such Lorentzian functions.

by bonding the device on the epitaxial multilayer structure, as illustrated in figure 4.8(a).

4.3. Magnetic characterization

A characterization of the basic magnetic properties is conducted on the CW sample, where d_Fe ranges from 0 nm to 1 nm by FMR measurements and magnetization curve analysis.

The FMR spectra are measured in a thickness range from 0.40 nm to 0.94 nm in the TR-MOKE setup. From the Kittel fit to the ϕ_H vs. H_FMR and f vs. H_FMR dependencies the samples MA constants and g-factors are extracted.

Magnetization curves are measured by MOKE in longitudinal and polar configuration in a d_Fe range from 0 nm to 1 nm. The qualitative analysis of the curves allows to classify the equilibrium magnetization orientation with respect to d_Fe. From the $K_\mathrm{eff} \cdot d_\mathrm{Fe}$ vs. d_Fe plot, extracted by the area method, K_i and K_v are determined.

4.3.1. Ferromagnetic resonance measurements

The FMR spectra of all six TR-MOKE samples (where d_Fe is 0.40 nm, 0.51 nm, 0.61 nm, 0.72 nm, 0.83 nm and 0.94 nm) are measured in the TR-MOKE setup where the static magnetic field is oriented in the sample plane at different angles ϕ_H with respect to the Fe[100] direction.

FMR spectra

The FMR spectra are of Lorentzian lineshape where depending on d_Fe, ϕ_H and f, single or multiple absorption peaks are observed. Figure 4.9 shows exemplary spectra measured on the 0.94 nm sample where f is 11.041 GHz and ϕ_H is (a) 68° and (b) $-22°$. The spectrum

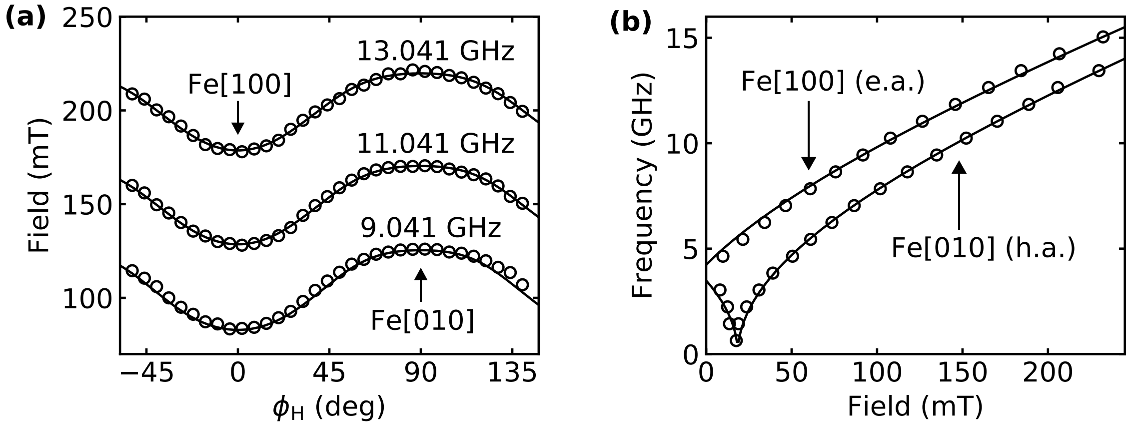

Figure 4.10.: Exemplary (a) angular and (b) frequency dependent FMR field measured on the on the 0.94 nm TR-MOKE device. The f and ϕ_H employed in the experiment are written in (a) and (b), respectively. The measured FMR fields are plotted as empty circles. The black solid lines are fits to the data conducted self consistently for all measurements, where magnetization dragging is taken into account. This procedure allows to extract all MA constants and the g-factor.

measured at 68° yields the typical FMR lineshape with one absorption peak. This spectrum is well fitted by equation 3.13 (sum of a symmetric and antisymmetric Lorentzian), red line in figure 4.9(b). In contrast, the spectrum measured at −22° has two absorption peaks. This spectrum can be well fitted by the sum of two functions described by equation 3.13, solid red line in figure 4.9(b).

The origin of the multiple absorption peaks is not understood and no clear dependence on d_{Fe}, ϕ_H, or the f could be identified. However, the H_{FMR} vs. ϕ_H and H_{FMR} vs. f dependencies (of all six TR-MOKE samples) can both be well fitted by the Kittel equation 2.41, if H_{FMR} is extracted from the main absorption peaks of the respective FMR spectra.

FMR angular and frequency dependence

Figure 4.10(a) shows the 0.94 nm samples H_{FMR} vs. ϕ_H dependencies extracted from the respective FMR spectra measured at an f of 9.041 GHz, 11.041 GHz and 13.041 GHz. Figure 4.10(b) shows the 0.94 nm samples H_{FMR} vs. f dependencies extracted from the respective FMR spectra measured for a field orientation along the Fe[100] and Fe[010] direction. In both figures the experimentally obtained data is plotted as open black circles. For all points H_{FMR} is extracted from the FMR spectrum main absorption peak.

The data shown in figure 4.10(a) and (b) is well fitted in a self consistent manner to the Kittel equation 2.41 describing a system with cubic MCA and additional in-plan uniaxial MA where magnetization dragging is taken into account, solid black line in both figures. Similar results are obtained for all other samples. The yielded MA constants and g-factors are discussed in the next part.

In order to extract the MA constants and the g-factor in principle it is sufficient to fit

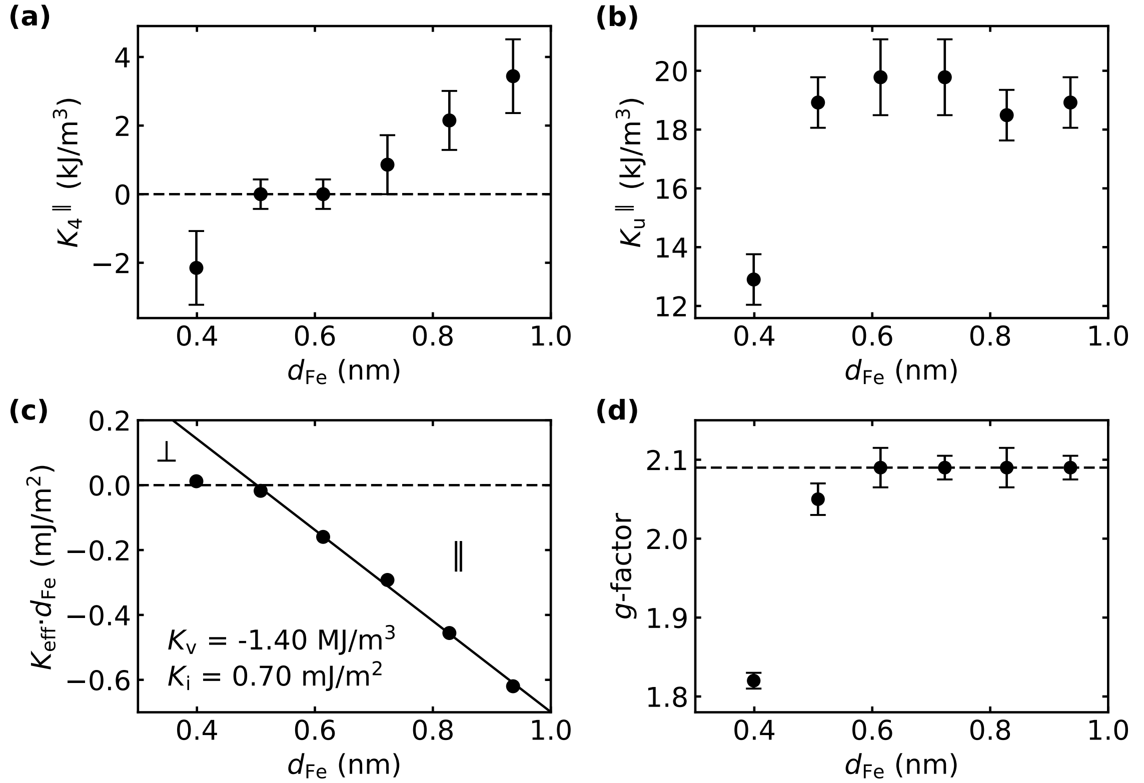

Figure 4.11.: MA constants and g-factor extracted by fitting self consistently the FMR field angular and frequency dependence of the six TR-MOKE samples where d_Fe is 0.40 nm, 0.51 nm, 0.61 nm, 0.72 nm, 0.83 nm and 0.94 nm, respectively. The dashed lines shown in figure (a), (c) and (d) are meant as visual aid. In (a) and (c) they mark the zero crossing point and in (d) the bulk Fe g-factor of 2.09.

the H_FMR vs. ϕ_H data measured at two different frequencies[1]. However, these frequencies have to be sufficiently far apart from each other in order for K_eff and g-factor extracted from the fitting procedure to be reliable. For ultrathin Fe films typically two measurements at ~10 GHz and ~40 GHz are conducted [124]. Here it is not possible to measure at high frequencies, as the TR-MOKE setups maximum field magnitude is restricted to approximately 300 mT. Thus for all samples data sets consisting of at least three H_FMR vs. ϕ_H and two H_FMR vs. f dependencies are fitted self consistently to the Kittel equation where magnetization dragging is taken into account. By this procedure the fitting error is minimized. The results of these fits is discussed in the following.

Magnetic anisotropy constants and g-factor

The d_Fe dependence of $K_4^\parallel$, $K_\mathrm{u}^\parallel$, $K_\mathrm{eff} \cdot d_\mathrm{Fe}$ and the g-factor are plotted in figure 4.11.(a), (b), (c) and (d), respectively. In the following the different MA constants and the g-factor are

---

[1] In order to extract the in-plane MA constants ($K_4^\parallel$ and $K_\mathrm{u}^\parallel$) it is even sufficient to fit the H_FMR vs. ϕ_H dependency measured at one frequency.

discussed.

The magnitude of $K_4^{||}$ is strongly reduced as compared to the bulk Fe value of $48\,\mathrm{kJ/m^3}$ [73]. In particular a linear decrease of $K_4^{||}$ from $3.4\,\mathrm{kJ/m^3}$ at a d_{Fe} of 0.94 nm to $-2.2\,\mathrm{kJ/m^3}$ at a d_{Fe} of 0.40 nm is observed. The change in sign occurs at a d_{Fe} of approximately 0.6 nm, showing the MCA easy axes transition from the Fe[100] to the Fe[110] direction. A similar behavior is documented in the literature [81, 82]. In these reports the d_{Fe} dependence of $K_4^{||}$ is found to be well described by a function $\sim 1/d_{\mathrm{Fe}}$. With respect to this phenomenological observation the decrease of $K_4^{||}$ is explained in terms of a Neél-type model. Within this model $K_4^{||}$ is composed of a volume and an interface contribution with competing easy axes. The volume term has its easy axis along the Fe[100] direction and the interface term along the [110] direction. For decreasing d_{Fe} then the interface contribution gains weight and eventually leads to the observed easy axes transition. This interpretation is reasonable as for pseudomorphicaly grown layers no alteration of the in-plane lattice constants is expected to occur. However, the here made observations rather indicates a linear dependence of $K_4^{||}$ on d_{Fe} what contradicts the interpretation in terms of an interface MCA and points to a d_{Fe}-dependent lattice relaxation, even in the ultrathin limit.

Surprisingly the Fe films are dominated by a (almost) d_{Fe}-independent in-plane uniaxial MA with easy axis along the Fe[100] direction. The average $K_{\mathrm{u}}^{||}$ is approximately $19\,\mathrm{kJ/m^3}$, except for the thinnest sample ($d_{\mathrm{Fe}} = 0.40\,\mathrm{nm}$) where $K_{\mathrm{u}}^{||}$ is $13\,\mathrm{kJ/m^3}$. The almost constant value of $K_{\mathrm{u}}^{||}$ clearly shows that it originates in the volume of the sample and not at its interface, as reported before [83]. The uniaxial in-plane MA observed here is attributed to a vicinal Fe surface [110]. This assumption is based on the RHEED pattern analysis which yields a vicinal Au surface, see section 4.1 for details, which is assumed to be adapted by the subsequently deposited Fe layer.

The $K_{\mathrm{eff}} \cdot d_{\mathrm{Fe}}$ vs. d_{Fe} plot reveals a linear relationship in the d_{Fe} region from 0.51 nm to 0.94 nm. This observation is attributed to interface MCA favoring PMA [97, 98]. The deviation of the linear dependency in the thinnest region is often encountered in experiment [6, 7, 100, 102, 106]. This deviation is either attributed to a thickness dependent MEA [100, 102, 106] or a decrease of the interface MCA or Curie temperature as the magnetic layer thickness approaches the inter-diffusion zone [107]. A fit is conducted in the linear region of the $K_{\mathrm{eff}} \cdot d_{\mathrm{Fe}}$ vs d_{Fe} plot and yields a K_{v} of $-1.40\,\mathrm{MJ/m^3}$ and a K_{i} of $0.70\,\mathrm{mJ/m^2}$. These values are in reasonable agreement with the ones previously reported for the similar material system ($K_{\mathrm{v}} = -1.53\,\mathrm{MJ/m^3}$ and $K_{\mathrm{i}} = 0.58\,\mathrm{mJ/m^2}$) [6]. The reduction of K_{v} as compared to the MSA of $-1.84\,\mathrm{MJ/m^3}$ has been attributed to a positive MEA originating from the Fe film strain [6]. It is interesting to note that for the 0.4 nm sample a K_{eff} of $30\,\mathrm{kJ/m^3}$ is yielded. Thus, the Fe film has PMA. The experimental observation of PMA in a Fe film grown on an Au buffer layer is regarded to be very hard to achieve and thus shows the superior quality of the investigated samples [114].

A bulk Fe g-factor of 2.09 is yielded for samples where d_{Fe} is thicker than 0.51 nm. The decrease of g-factor with decreasing d_{Fe} for the thinnest samples (0.40 nm and 0.51 nm) is attributed to the increasing contribution of the unquenched interface orbital momentum [183].

4.3.2. Magnetization curve analysis

In the first part of this section the magnetization curves measured on the CW sample are analyzed in a qualitative manner. This analysis allows to classify the magnetization equilibrium orientation in dependence of d_{Fe}. In the second part of this section, the $K_{\mathrm{eff}} \cdot d_{\mathrm{Fe}}$ vs d_{Fe} plot extracted by the area method from the out-of-plane curves is evaluated.

Magnetization equilibrium orientation versus iron thickness

Four regions with different equilibrium orientation of magnetization are classified on the CW sample in dependence of d_{Fe} by analyzing the magnetization curves measured by means of MOKE in polar and longitudinal configuration. The different equilibrium magnetization orientations are: (1) in-plane orientation (d_{Fe} ranging from 1 nm to 0.5 nm), (2) the spin reorientation transition (SRT) region where no clear easy axis exists (d_{Fe} ranging from 0.5 nm to 0.4 nm), (3) PMA (d_{Fe} ranging from 0.4 nm to 0.3 nm) and (4) a region of superparamagnetic (SPM) behavior (d_{Fe} ranging from 0.3 nm to 0.2 nm). Below a d_{Fe} of 0.2 nm no magnetic signal is detectable.

A schematic representation of the magnetization equilibrium orientation vs. d_{Fe} is given by the axis shown to the left of figure 4.12. Representative magnetization curves for each of the four regions are shown in figure 4.12(a)-(l). The plots are arranged in four rows, and three columns. Inside each row, all presented curves are measured on a d_{Fe} region with same equilibrium magnetization orientation. The curves arranged in the same columns are measured in the same MOKE configuration: first column ⇔ polar configuration, second column ⇔ longitudinal configuration (field along Fe[100]) and, third column ⇔ longitudinal configuration (field along Fe[010]). The numbers in the legend of each plot give the exact d_{Fe} in nanometer. In the following, each of the four regions is discussed in detail.

The magnetization curves measured in the first region, where d_{Fe} is in between 1 nm and 0.5 nm, can be understood assuming a cubic system with additional uniaxial in-plane MA with easy axis along the Fe[100] direction. Typical square hysteresis loops are measured along the Fe[100] direction showing the easy axis of the system. The magnetization curves measured along the Fe[010] direction reveals a hard axis where the complicated details of the curves qualitatively follow the form expected from a system with cubic MCA dominated by a superimposed uniaxial MA where both contributions have their easy axis along the Fe[100] direction [110]. The out-of-plane magnetization curves measured in the polar configuration are typical hard-axes loops showing that the equilibrium orientation of magnetization is in the Fe film. The decrease of saturation field with decreasing d_{Fe} is typical for ultrathin Fe layers with strong interface MCA [97, 98]. The magnitude of the interface MCA is discussed in the second part of this section.

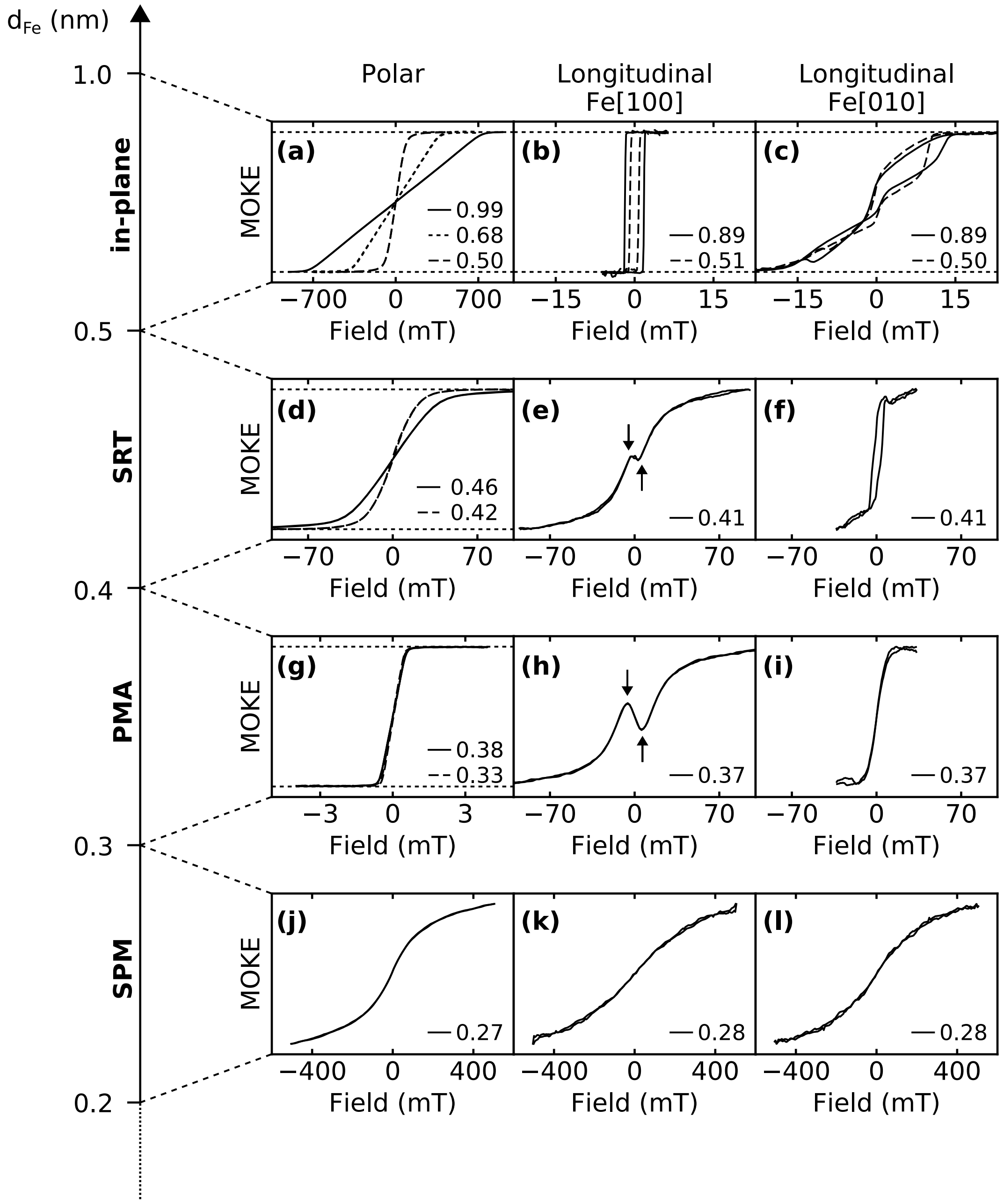

Figure 4.12.: Classification of the CW samples equilibrium magnetization orientation in dependence of d_{Fe}, conducted by qualitatively analyzing the magnetization curves measured by MOKE in polar and longitudinal configuration. Four different equilibrium states are differentiated, i.e. the in-plane magnetization orientation, the SRT, the PMA and the SPM state. The magnetization state and the corresponding d_{Fe} region is written on the schematic axis shown to the left of the figure. Figure (a)-(l) show representative magnetization curves, where each row corresponds to a d_{Fe} range where similar magnetic behavior is observed. Curves shown in the first column are measured in polar configuration. The curves shown in the second and third column are measured in longitudinal configuration, where the field is applied along the Fe[100] and Fe[010] direction, respectively. The numbers written inside the plots are d_{Fe} in nanometer.

The magnetization curves measured in polar and longitudinal configuration where d_{Fe} is in between 0.5 nm and 0.4 nm are all hard-axes-like. This behavior indicates a SRT region where no clear in- or out-of-plane orientation of magnetization in equilibrium exists. This assumption is further confirmed by the in-plane curves measured along the Fe[100] direction. The tilted magnetization orientation here leads to both L- and PMOKE contributing to the measured signal, what explains the peculiar features of the curve, which are marked by arrows in the plot.

The magnetization curves measured where d_{Fe} is in between 0.4 nm and 0.3 nm strongly suggest that here the sample has PMA. The curves measured in longitudinal configuration, along both field directions, are clearly hard-axes-like. Furthermore, along the Fe[100] direction clear PMOKE contributions are observed (by arrows in the plot). In contrast, the curves measured in polar configuration are almost rectangular with a saturation field well below 1 mT. The lack of hysteresis in the out-of-plane curves is attributed to the formation of a stripe domain configuration, which minimizes the energy costs of stray fields and is quite commonly observed in thin film systems with PMA.

The curves measured in a d_{Fe} region in between 0.3 nm and 0.2 nm quite clearly show SPM behavior. Here the magnetization curves shape is virtually independent of the field orientation. Furthermore the sample is not saturated for the here applied fields of over 400 mT. In the SPM state the film is thought to consist of several small Fe islands distributed over the sample surface which weakly interact with each other and thus yield the here observed magnetization reversal.

No MOKE signal is detectable for a d_{Fe} below 0.2 nm.

Volume and interface magnetic anisotropy

Figure 4.13(a) shows the $K_{\mathrm{eff}} \cdot d_{\mathrm{Fe}}$ vs. d_{Fe} plot extracted by the area method from the out-of-plane magnetization curves. The data is plotted as full black circles where d_{Fe} is above 0.5 nm. In this d_{Fe} region square in-plane easy axes are measured and thus K_{eff} can be determined from the out-of-plane curves alone. For a d_{Fe} smaller than 0.5 nm this treatment is not valid anymore (indicated by plotting the data points as gray full circles). In this d_{Fe} region one has to extract K_{eff} from the area enclosed by both the in-plane and out-of-plane curve. However the in-plane curve cannot be measured by means of MOKE as the signal is composed of both PMOKE and LMOKE contributions and untangling these components is a very cumbersome task [132, 154].

A linear fit to the $K_{\mathrm{eff}} \cdot d_{\mathrm{Fe}}$ vs. d_{Fe} plot (solid black line in figure 4.13(a)) yields a K_{v} of $-1.23\,\mathrm{MJ/m^3}$ and a K_{i} of $0.59\,\mathrm{mJ/m^2}$. These values are slightly reduced as compared to the ones extracted by the FMR. For comparison, the $K_{\mathrm{eff}} \cdot d_{\mathrm{Fe}}$ vs. d_{Fe} data extracted by both FMR and MOKE measurements are plotted in figure 4.13(b). The deviation is attributed to an underestimation of K_{eff} determined by the area method from the magnetization curves measured by MOKE. It is well known that such an underestimation can occur whenever the

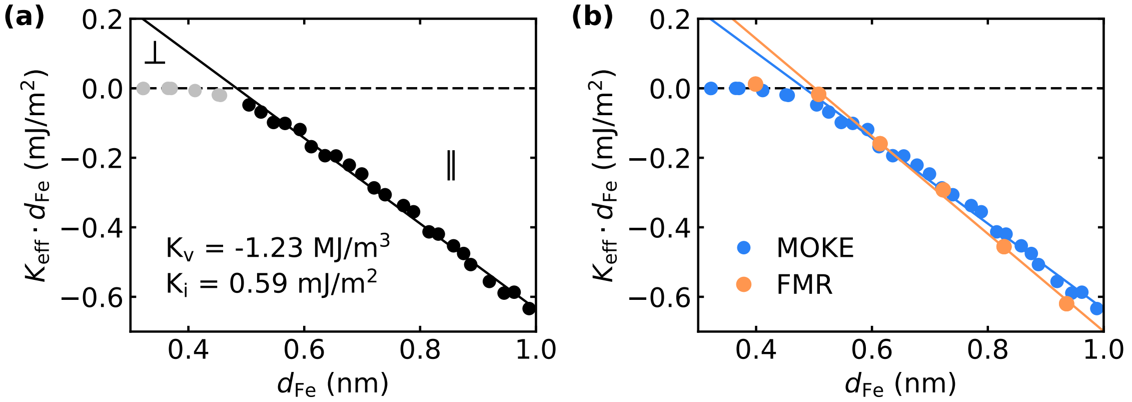

Figure 4.13.: (a) $K_{\text{eff}} \cdot d_{\text{Fe}}$ vs. d_{Fe} plot measured on the CW sample by means of MOKE. K_{eff} is extracted from the out-of-plane magnetization curves via the area method. The data is plotted as black circles where d_{Fe} ranges from 0.5 nm to 1 nm. In this thickness region the extraction of K_{eff} from the out-of-plane curves alone is valid, as the easy axis of the system is in the sample plane. The data points are plotted gray in the region where d_{Fe} is smaller than 0.5 nm. In this d_{Fe} region a deviation of the magnetization equilibrium from the in-plane orientation occurs and thus the data points cannot be quantitatively evaluated. Further explanations are given in the text. The black solid line is a linear fit to the data where d_{Fe} ranges from 0.5 nm to 1 nm by which K_v and K_i are determined. In (b) the $K_{\text{eff}} \cdot d_{\text{Fe}}$ vs. d_{Fe} data (and respective fits) obtained by both FMR and MOKE are shown for comparison.

saturation field of the curve is not known and thus is estimated in the raw data processing, as it is here the case [107].

4.4. Gating time dependence

A decrease of ΔK_{eff} with decreasing gating time is found. The results suggest that the electronic VCMA is superimposed either by magneto ionic, or charge trapping effects. By reducing the gating time below 1.3 ms most likely only the electronic VCMA contributes to the observed effect.

Static method versus modulation technique

Figure 4.14(a) shows the out-of-plane magnetization curves measured by MOKE in polar configuration on the CW sample where d_{Fe} is 0.46 nm with a U_g of ±10 V, respectively. The time needed to measure each of the two curves is approximately 10 min. An increase of PMA is observed for negative U_g what is in accordance with previous reports on the VCMA in the Fe/MgO bilayer system [6]. Assuming an initial gating state at 10 V, a ΔK_{eff} of 1.65 kJ/m^3 extracted by the area method. The respective ξ is 2.8 fJ/Vm.

On the same sample ΔK_{eff} is measured with the modulation technique. Here U_g is modulated in between 0 V and −10 V, where the initial gating state is set at 0 V. A

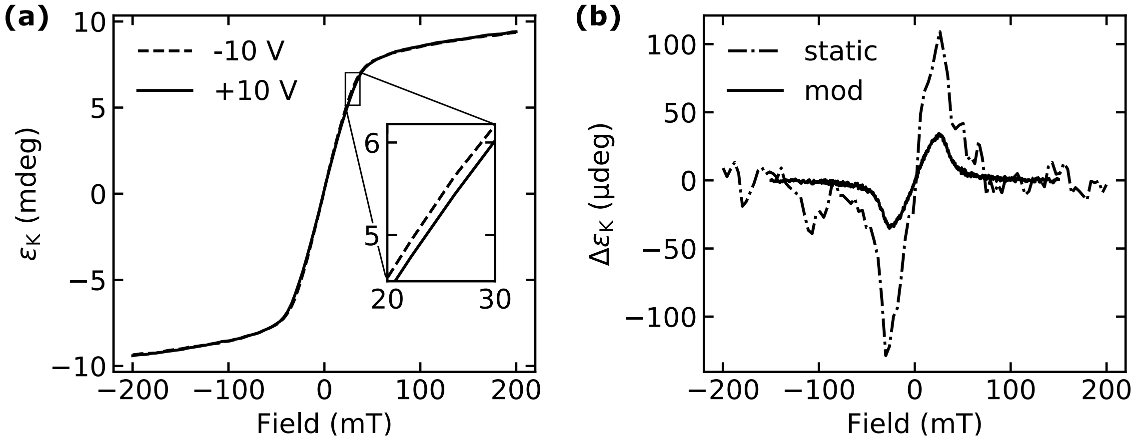

Figure 4.14.: Comparison between the VCMA extracted in a static fashion and via the modulation technique. (a) Static out-of-plane magnetization curves measured on the CW sample where d_{Fe} is 0.46 nm and a top gate voltage of ±10 V is applied. (b) Modulation curve (solid black line) measured on the same sample where U_{g} is modulated in between 0 V and −10 V at a sinusoidal f_{m} of 37 Hz, and the initial state is set at 0 V. The dashed dotted line is the difference between the out-of-plane magnetization curves shown in (a), where the resulting curve is divided by two. Further explanations are given in the text. The static measurement yields a ξ of 2.8 fJ/Vm and the modulation measurement a ξ of 0.8 fJ/Vm.

sinusoidal modulation f_{m} of 37 Hz is employed resulting in an effective gating time for each voltage polarity below 27 ms. The modulation curve is plotted in figure 4.14(b) as black solid line. With the area method (see section 3.6) a ΔK_{eff} of 0.25 kJ/m^3 is extracted. The respective ξ is 0.9 fJ/Vm.

The VCMA measured with the static technique yields a magnitude around 300 % larger than the value obtained by the modulation technique. In order to visually back this finding, the difference of the static out-of-plane curves, divided by two, is plotted as dash-dotted line in figure 4.14(b). The division by two is conducted as the magnitude of the difference in applied U_{g} in the static measurement (20 V) is twice as large as in the modulation technique measurement (10 V). The observed strong reduction of ΔK_{eff} extracted via the static method as compared to the value obtained by modulation technique is attributed to the difference in the effective gating times employed with the two techniques. As discussed in the following the here observed VCMA most likely is superimposed by other effects than the pure electronic VCMA.

The electronic VCMA [54, 55, 60] relies on the charge mobility at the Fe/MgO bilayer interface and has been shown to induce magnetization dynamics [15, 18, 22, 26] occurring on the sub nanosecond timescale. In case where only the electronic VCMA is probed a constant ΔK_{eff} vs. gating time dependency is expected, at least for effective gating times well above the sub nanosecond timescale (as employed here). The significant reduction of ΔK_{eff} with decreasing gating time thus strongly suggest that the electronic VCMA is superimposed by contributions with long transition times. Two types of such effects are

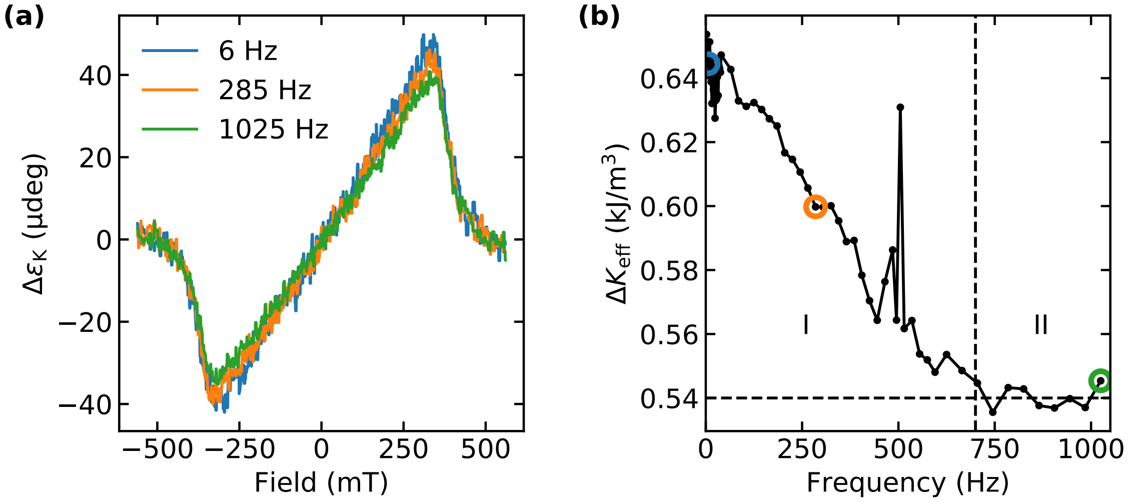

Figure 4.15.: Modulation frequency dependence of the VCMA measured by the modulation technique on the SW sample where d_{Fe} is 0.55 nm. (a) Modulation curves measured at a f_{m} of 6 Hz, 285 Hz and 1025 Hz. (b) ΔK_{eff} vs. frequency plot extracted from the curves.

known: charge trapping in the dielectric layer [17] and the magneto ionic VCMA [62, 122], where in both cases transient times of several minutes (up to one hour [122]) are reported. The measurement time of the static curves used here is approximately 10 min. In contrast, the effective gating time in the modulation measurement (where a sinusoidal f_{m} of 37 Hz is employed) is well below 27 ms. Thus it seems very likely that an increase of either charge trapping or magneto ionic contributions explains the observed strong increase of ΔK_{eff} by nearly 300 %, where the gating time is increased from below 27 ms to approximately 10 min.

In the following the dependence of ΔK_{eff} on f_{m} (and thus the effective gating time in the sub second regime) is investigated.

Frequency dependence of modulation curves

The dependence of ΔK_{eff} on the modulation f_{m} is investigated on the CW sample where d_{Fe} is 0.55 nm. Here the modulation curves are measured with a rectangular modulation f_{m} ranging from 2 Hz to 1025 Hz. Thus f_{m} can be directly associated with a respective gating time. Here U_{g} is modulated in between −5 V and 5 V, where the initial gating state is set at 5 V. Figure 4.15(a) shows representative modulation curves measured at a f_{m} fo 6 Hz, 285 Hz and 1025 Hz. Here already a slight decrease of the curves amplitude is visible. The dependence of the VCMA reduction becomes more apparent with respect to the ΔK_{eff} vs. f_{m} plot shown in figure 4.15(c). The values of ΔK_{eff} are found to decrease from 0.64 mJ/m^3 to 0.54 mJ/m^3 where f_{m} increases from 2 Hz to 700 Hz, respectively. This decrease corresponds to a reduction of ΔK_{eff} by approximately 16 %. For a f_{m} higher than 700 Hz no further change of ΔK_{eff} is observed. The spike in ΔK_{eff} observed at a f_{m} of 500 Hz cannot be explained and thus the following discussion is treated as measurement artefact.

As stated before, both charge trapping [17] and ionic effects [62, 122] are usually expected to have transition times in the order of several minutes. Thus the magnitude of these effects is expected to drastically diminish with decreasing gating time. The comparison of the VCMA evaluated by the static and modulation technique yields a reduction of ΔK_{eff} of around 75 % where the effective gating time is decreased from approximately 10 min to well below 27 ms. Here, a reduction in ΔK_{eff} of 16 % is yielded for a decrease in gating time from 500 ms (where f_{m} is 2 Hz) to 1.3 ms (where f_{m} is 700 Hz). This observation leads to the conclusion that charge trapping or magneto ionic effects are still present in the VCMA measured by the modulation technique, where the effective gating time is above 1.3 ms. Indeed it has been shown that both charge trapping and magneto ionics can occur at relatively short timescales: charge trapping in defect states of thin MgO layers has been reported to occur at $\sim$100 ns [184], and transient times of the magneto ionic VCMA in GdO/Fe structures could be reduced to $\sim$1 µs [62]. The observations made here conclude that magneto ionic or charge trapping superimposes the measured VCMA up to an effective gating time of 1.3 ms. In case where the effective gating time is below 1.3 ms only the electronic VCMA contributes to the measured signal. Please note, that the here observed reduction of ΔK_{eff} by “only” 16 %, where f_{m} is increased from 2 Hz to 700 Hz, shows with the modulation technique in any case mainly the electronic VCMA is probed.

4.5. Gate voltage dependence

The dependence of ΔK_{eff} on U_{g} is investigated by both the static method and the modulation technique. The K_{eff} vs. U_{g} dependence extracted from the static curves yields a hysteresis. In contrast a linear relationship is extracted by the modulation technique. The results further confirm the assumption that with increasing gating time the VCMA is strongly superimposed with magneto ionic or charge trapping effects.

The U_{g} dependence of K_{eff} in a voltage range between $\pm 45\,\mathrm{V}$[2] is measured in a static manner on the SW sample where d_{Fe} is 0.4 nm. Figure 4.16(a) shows representative out-of-plane magnetization curves where U_{g} is ± 30 V. Electron depletion at the Fe/MgO bilayer interface causes a decrease of the saturation field by around 10 mT, i.e. the MA contributions favoring PMA are increased. This observation is in accordance with previous reports on the VCMA in MgO/Fe structures [6, 37, 39]. The out-of-plane curves are measured while U_{g} is swept in a full cycle from 45 V to -45 V and back again. Figure 4.16(b) shows the resulting K_{eff} vs. U_{g} plot. Here K_{eff} is extracted via the area method

---

[2] The U_{g} applied to the capacitor structures here yield extremely high electric fields in the sample dielectric layer. For example, the application of 45 V leads to an electric field in the MgO layer of 0.6 V/nm. This electric field value is close to the breakdown field of the dielectric layer. In contrast to the breakdown field measurement here the voltage is applied over a time span of several minutes which further enhances the stress. Thus the experimental results shown in figure 4.16 are very hard to obtain from a technological point of view.

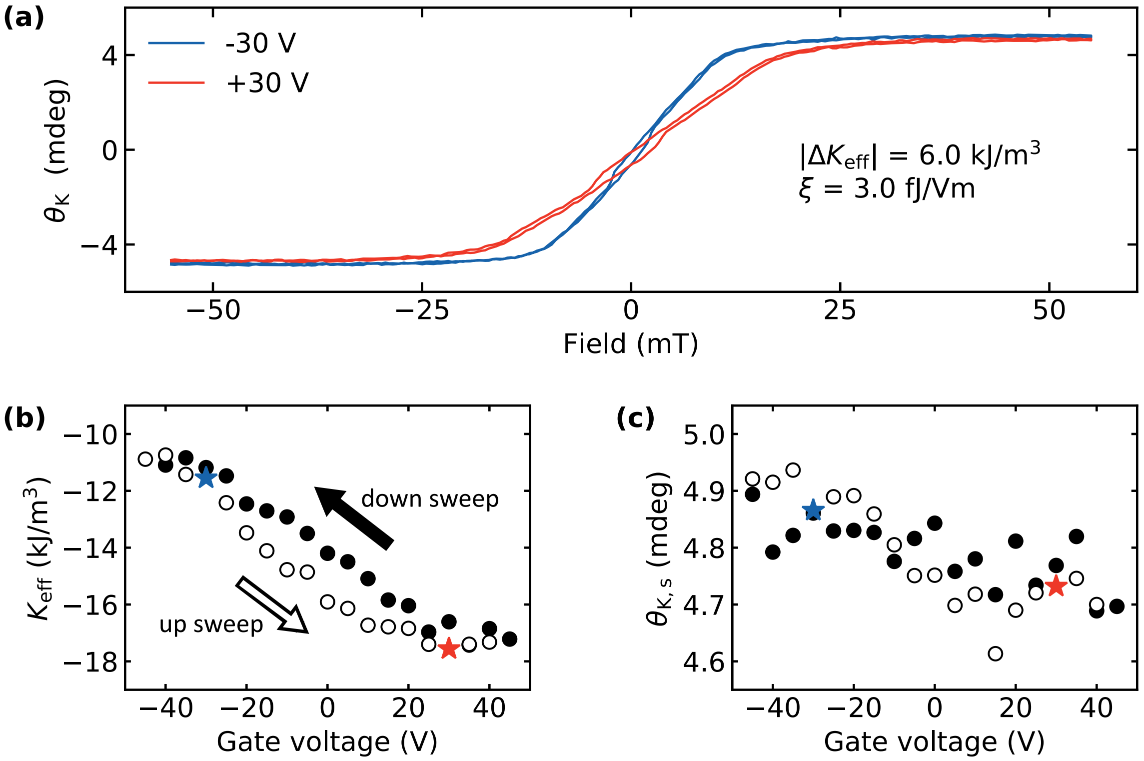

Figure 4.16.: VCMA determined from the out-of-plane magnetization curves measured by means of MOKE in polar configuration on the SW sample where d_{Fe} is 0.4 nm. (a) Out-of-plane magnetization curves where a U_g of ±30 V is applied, respectively. (b) K_{eff} vs. U_g dependency, determined via the area method where U_g is cycled between ±45 V. (c) Respective change of $\theta_{K,s}$. Star markers highlight the values obtained from the curves shown (a).

from the respective out-of-plane magnetization curves. A hysteresis is obtained where U_g is in between ±20 V. A slight reversible change of $\theta_{K,s}$ with U_g is observed, see figure 4.16(c). However, $\theta_{K,s}$ changes by only (2.4 ± 3.2) µdeg/V, which corresponds to change of only 0.05 %/V.

The U_g dependence of the VCMA is furthermore investigated with the modulation technique on the CW sample, where d_{Fe} is 0.46 nm. Here U_g is modulated in between 0 V and the modulation voltage which is cycled in between ±10 V. The initial state is always set at 0 V. A sinusoidal f_m of 37 Hz is employed. Figure 4.17 shows exemplary curves taken from the up sweep, where the modulation voltage is swept from −10 V to 10 V. In consistence to the static measurements shown in figure 4.16 a negative U_g (electron depletion at the Fe/MgO interface) leads to an increase in K_{eff} which is in accordance to previous reports on the VCMA in the Fe/MgO system [6, 37, 39]. In figure 4.17(b) the full ΔK_{eff} vs. modulation voltage plot is shown. In contrast to the hysteretic dependence yielded by the static measurements, here a linear dependency is found.

A hysteresis in the U_g dependence of the VCMA has been suggested before to be induced by either magneto ionic or charge trapping effects [6, 47]. Those effects naturally explain

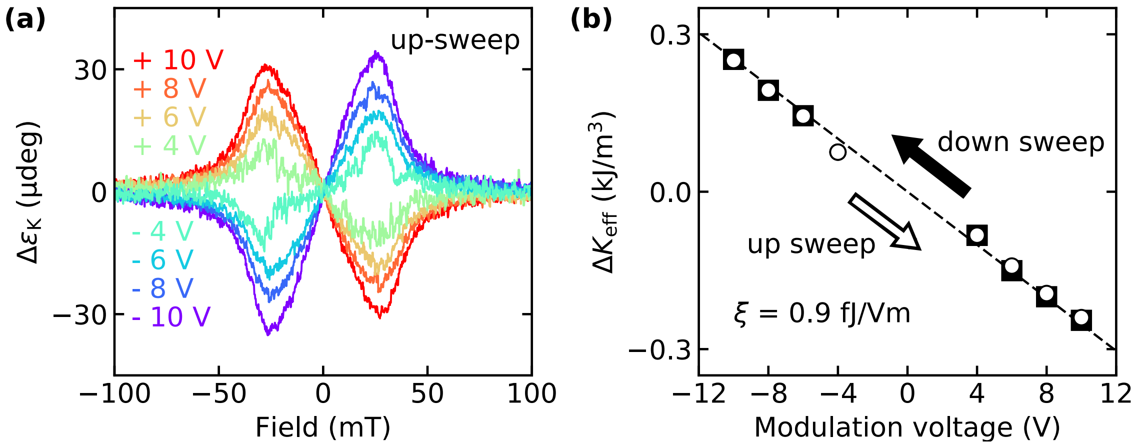

Figure 4.17.: Voltage dependence of the VCMA measured by means of the modulation technique on the CW sample where d_{Fe} is 0.46 nm. (a) Exemplary curves taken from the up sweep where the modulation voltage is sweeped from −10 V to 10 V. (b) ΔK_{eff} extracted via the area method from the curves measured where the modulation voltage is cycled in between ±10 V. From the slope of the linear fit (dashed) line here a ξ of 0.9 fJ/Vm is extracted.

a hysteresis in the VCMA vs U_{g} dependence due to their non-volatile character [17, 32, 122, 185]. The gating time dependency of the VCMA investigated in this thesis shows that the VCMA extracted in a static manner is dominated by magneto ionic or charge trapping effects. In contrast, it has been shown that the VCMA measured by the modulation technique is mainly of electronic nature. With respect to these results it makes sense that a hysteresis is observed in the K_{eff} vs. U_{g} dependence measured in the static fashion and a linear relation of the ΔK_{eff} vs. U_{g} dependence measured with the modulation technique.

Whether the here measured contributions superimposing the electronic VCMA are by nature charge trapping or magneto ionic effects, remains an open question. Both mechanism seem to be possible. Clear evidence for charge trapping in both MgO [184] and Al_2O_3 [186] layers have been reported. Magneto ionic VCMA is normally only observed in systems employing a high ionic conductance dielectric layer, like GdO [32, 122, 185]. However, Bonell et al. [63] has shown by XAS and MCD measurements that the Fe oxidation state in MgO/FeCo based multilayer structures can be manipulated by a gate voltage. Thus further experiments illuminating the true physical mechanism behind the here measured VCMA are highly desirable.

4.6. Iron thickness dependence

The d_{Fe} dependence of ΔK_{eff} and ξ is investigated on the CW sample by the modulation technique. At each d_{Fe} two modulation curves are measured with a modulation voltage of ±10 V, respectively. In any case the initial gating state is set at 0 V. A sinusoidal f_{m} of 37 Hz is employed. Figure 4.18(a) shows representative curves where the modulation

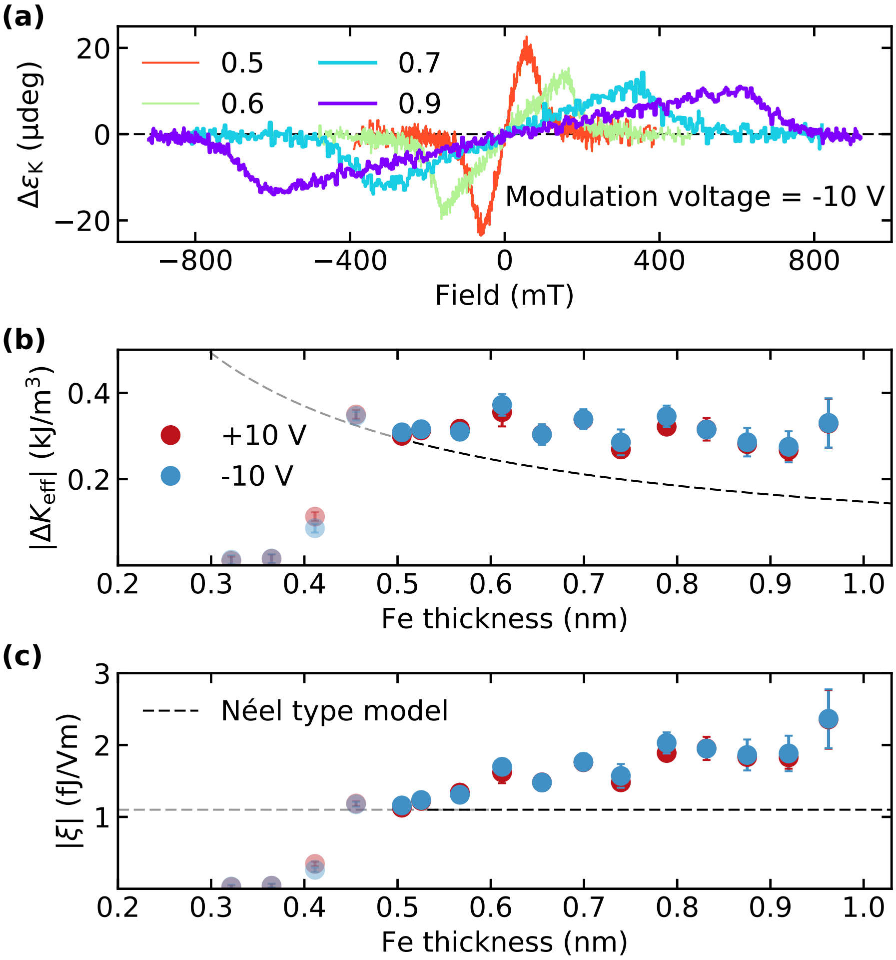

Figure 4.18.: VCMA vs. d_{Fe} dependency measured by means of the modulation technique on the CW sample where d_{Fe} ranges from 0 nm to 1 nm. (a) Representative measurement curves where the modulation voltage is −10 V. The numbers written inside the plot are Fe thicknesses in nanometer. (b) $|\Delta K_{\mathrm{eff}}|$ vs. d_{Fe} and (c) $|\xi|$ vs. d_{Fe} dependency. The dashed line in (b) and (c) gives the expected dependency for a VCMA which is only at the interface of the Fe layer (Néel type model).

voltage is −10 V. The numbers inside the plot give the d_{Fe} in nanometer. Figure 4.18(b) and (c) show the $|\Delta K_{\mathrm{eff}}|$ vs. d_{Fe} and $|\xi|$ vs. d_{Fe} plot extracted from the modulation curves via the area method. The red and blue markers correspond to a modulation voltage of ±10 V, respectively. All data points with a d_{Fe} smaller than 0.5 nm are semi-transparent. In this d_{Fe} region the equilibrium magnetization orientation is not fully in the sample plane (see section 4.3.2 for details) and thus the obtained values should only be interpreted in a qualitative manner. The following quantitative discussion is restricted to the d_{Fe} range from 0.5 nm to 1 nm

The magnitude of ΔK_{eff} and ξ measured with a modulation voltage of ±10 V are virtually identical, confirming the linear U_{g} dependence of the VCMA extracted by the modulation technique. The sinusoidal f_{m} of 37 Hz employed here results in an effective gating time far below 27 ms. Thus it can be assumed that mainly the electronic VCMA is probed. However, the d_{Fe} dependency of both ΔK_{eff} and ξ significantly deviates from the expected Néel-type behaviour. In a Néel-type model the VCMA is only at the interface of the sample. Such VCMA is naturally expected to be observed in Fe layers due to the very short screening length in metals which restricts any electric field to the topmost atomic layer of the metal film in a metal/dielectric bilayer exposed to a gate voltage [54, 58, 120]. The interface origin of the VCMA in Fe was clearly demonstrated by Bauer et al., who showed that the insertion of one atomic layer of Au in between the interface of a MgO/Fe bilayer structure is sufficient to completely annihilate the VCMA in the Fe film [32]. The Néel-type model describes the ΔK_{eff} dependency on d_{Fe} by a function $\sim 1/d_{\mathrm{Fe}}$ and consequently ξ is expected to be constant over the whole d_{Fe} range. The Neél-type $|\Delta K_{\mathrm{eff}}|$ and $|\xi|$ dependency on d_{Fe} is plotted as dashed line in figure 4.18(b) and (c), respectively. In stark contrast to the model here a constant $|\Delta K_{\mathrm{eff}}|$ of approximately 0.35 kJ/m^3 is observed over the whole d_{Fe} range and $|\xi|$ increases by over 200 % where d_{Fe} increases from 0.5 nm ($|\xi|$ =1.1 fJ/Vm) to 0.97 nm ($|\xi|$ = 2.4 fJ/Vm). In the following three possible explanations for this observation are discussed. The explanations rely on d_{Fe} dependent strain, the piezo VCMA and a d_{Fe} dependent Au surface segregation during the Fe layer preparation.

Very recently Lau et al. [49] reported an increase of $|\xi|$ by almost 200 % in MgO/CoFeB bilayer based structures where the CoFeB thickness increases from 0.5 nm to 1.2 nm. In a phenomenological manner they are able to fit the unexpected thickness dependence of $|\xi|$ with respect to a higher order MEA constant which is derived from the $K_{\mathrm{eff}} \cdot d_{\mathrm{CoFeB}}$ vs. d_{CoFeB} dependency in its non-linear region [100, 102, 106, 107]. Lau et al. argue that the higher order MEA is related to thickness dependent strain and as the strain develops in the CoFeB film also an alteration of its electronic system and thus the VCMA can be expected. Indeed it has been shown that film strain severely impacts the characteristics of the VCMA voltage dependence [64] and for example was used to explain the the v-shaped voltage dependence of the VCMA reported by Nozaki et al. in the MgO/Fe/MgO trilayer based structures [27]. However, in our case the introduction of higher order MEA constants is not justified since the $K_{\mathrm{eff}} \cdot d_{\mathrm{Fe}}$ vs. d_{Fe} dependency is linear in the examined d_{Fe} region. Thus the influence of a d_{Fe} dependent strain on the VCMA characteristics of the ultrathin Fe layers is excluded.

The next possible explanation of the here observed constant ΔK_{eff} and increase of ξ with increasing d_{Fe} is based on the Au segregation observed during the epitaxy of Fe [29, 167–175]. Due to the short screening length of metals [54, 58], which restrict the electric field to the topmost atomic layer, it is clear that any amount of Au located in between the interface of the investigated Fe/MgO bilayers, will significantly reduce the VCMA. For example, Bonnel et al. estimated by X-ray absorption measurements that 0.8 ± 0.3 ML of Au segregate to the surface of an 1 nm thick epitaxial Fe film. It has been shown that the amount of Au decreases with increasing d_{Fe} [168, 173]. Thus, it seems very likely that the observed increase of $|\xi|$ with increasing d_{Fe} is directly related to a decrease of Au atoms on

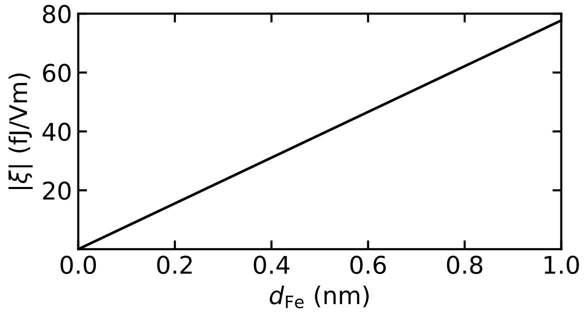

Figure 4.19.: Estimation of the piezo VCMA in Fe. The $|\xi|$ vs. d_{Fe} dependency is derived assuming that the inverse piezoelectric effect measured in MgO by Naik et al. [35] is fully translated to the Fe layer and there leads to the VCMA through the modulation of the MEA.

the Fe surface and thus a decrease of screening of the VCMA with increasing d_{Fe}. In order to further confirm this assumption a d_{Fe} dependent measurement of the surface chemistry of the investigated Fe films would be very interesting.

The third explanation for the unexpected d_{Fe} dependence of ξ and ΔK_{eff} is based on the report of the inverse piezoelectric effect in MgO by Naik et al. [35]. By PFM measurements they extract a significant strain coefficient d_{zz} of 37 pm in a 5 nm thick MgO layer where a U_{g} of 1 V is applied. The observation of the inverse piezo effect is quite surprising as MgO is a non-polar crystal. If indeed this effect persists, a piezo VCMA is expected to occur in an adjacent magnetic layer caused by an alteration of the MEA. In the following the piezo VCMA in Fe expected from the results of Naik et al. is estimated. It is assumed that the inverse piezoelectric effect in the MgO layer is fully translated into the Fe layer. Furthermore the MEA of the Fe layer is approximated by that of an isotropic material, which is written as [107]

$$E_{\mathrm{MEA}} = -\frac{3}{2}\lambda_{\mathrm{s}} E \epsilon \cos\theta, \tag{4.1}$$

where λ_{s} is the magnetostriction constant, E the Young modulus and ϵ the strain. For bulk Fe, λ_{s} is -7×10^{6} and E is 200 GPa [73]. Inserting these values and d_{zz} measured by Naik et al. into equation 4.1 leads to a $|\Delta K_{\mathrm{eff}}|$ of $8\,\mathrm{kJ/m^3}$ for an electric field in the MgO layer of 0.1 V/nm. As it is assumed that the inverse piezo effect is fully translated into the Fe layer, the resulting piezo VCMA naturally occurs as a volume effect where ΔK_{eff} is independent of d_{Fe}. Respectively $|\xi|$ will linearly increase with d_{Fe}. In figure 4.19 the $|\xi|$ vs. d_{Fe} dependency expected by the above made estimation is plotted for d_{Fe} ranging from 0 nm to 1 nm. The magnitude of ξ at 1 nm is 80 fJ/Vm which is far higher than the here extracted value of 2.4 fJ/Vm. The high magnitude of ξ predicted by the piezo VCMA is a direct consequence of the high d_{zz} reported by Naik et al. [35]. Furthermore both using the MEA of an isotropic system and assuming that the inverse piezo electric

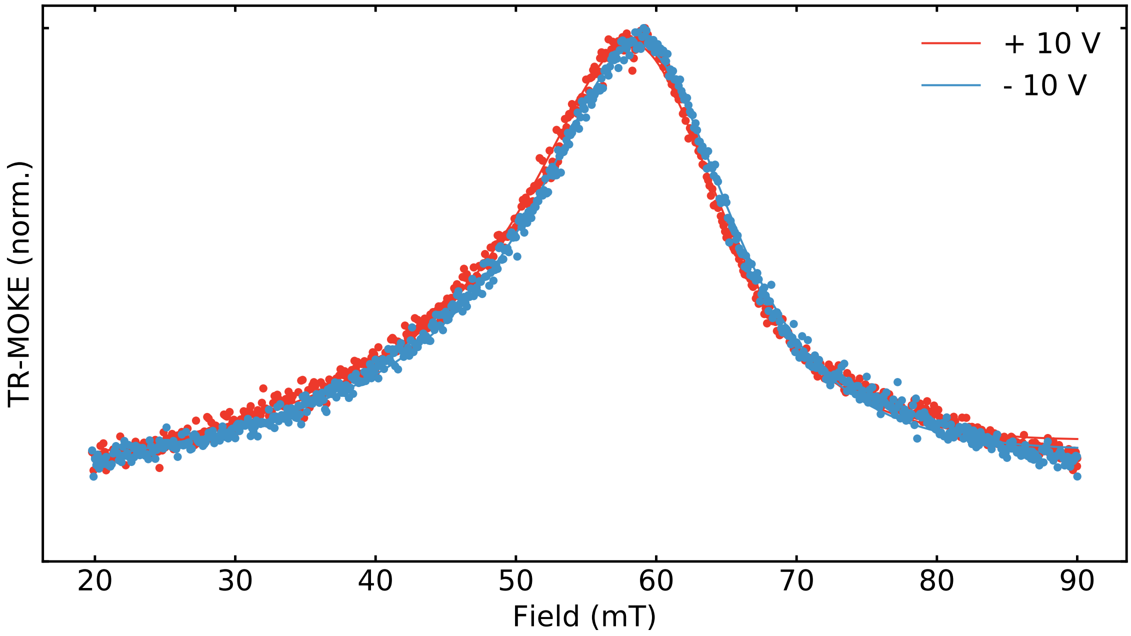

Figure 4.20.: Voltage control of the FMR field. Representative FMR spectra measured on the 0.61 nm TR-MOKE device where a U_g of ±10 V is applied. The field is oriented along the Fe[100] direction. The peak amplitudes of both spectra are normalized to their maximum for a better comparability.

effect is fully translated into the Fe layer are only crude estimations and could lead to an overestimation of the piezo VCMA. However, the qualitative agreement between the estimated and observed d_{Fe} dependence of both $|\xi|$ and $|\Delta K_{\mathrm{eff}}|$ shows that indeed the piezo VCMA could be causing the here observed peculiar d_{Fe} dependence of the VCMA. Further experiments, which prove or disprove the inverse piezoelectric effect in the non-polar MgO crystal, are highly desirable.

4.7. Voltage control of the ferromagnetic resonance position

Preliminary results show the voltage control of the FMR position. These results offers an exciting new route for future investigations of the VCMA impact on the fourfold interface MCA.

Figure 4.20 shows the 0.61 nm TR-MOKE samples FMR spectra measured with a U_g of ±10 V as red and blue points, respectively. The data is fitted well by equation 3.13, solid red and blue lines in the figure. Clearly, a shift of H_{FMR} towards higher fields with negative U_g is visible, i.e. electron depletion in the Fe layer at the MgO/Fe interface increases the PMA of the sample, which is in accordance with both the literature [6] and the VCMA measurements conducted in the modified MOKE setup. The measurements shown in figure 4.20 are repeated in total six times for each gate voltage polarity, where in any case a shift of H_{FMR} due to the VCMA is observed. From these measurements the average shift in

H_{FMR} (where for each spectra H_{FMR} is extracted by the respective fit) is estimated to be (0.52 ± 0.19) mT (where ΔU_{g} is 20 V). This shift corresponds to a ΔK_{eff}[3] of (0.45 ± 0.17) kJ/m^3 and a ξ of (0.67 ± 0.25) fJ/Vm.

This $|\xi|$ is significantly reduced as compared to the value measured by the modulation technique (1.6 fJ/Vm). The difference in ξ is especially surprising with respect to the involved gating times: approximately 1 h is needed to measure each of the FMR spectra shown in figure 4.20. Thus charge trapping and magneto-ionic effects are expected to dominate the VCMA. In contrast the VCMA measured with the modulation technique involves gating times below 27 ms and thus mainly the electronic VCMA is probed. The discrepancy between the VCMA magnitude evaluated from the FMR measurements compared to the values extracted by the modulation technique still is an open question. In future a LIA measurement technique is planned to be implemented in the TR-MOKE setup which will allow to investigate the gating time dependence of the VCMA in more detail.

Achieving the voltage control of H_{FMR} is quite a challenging task. It turns out that measuring the FMR spectra with applied U_{g} in the standard TR-MOKE setup described in section 3.7 leads to an almost immediate breakdown of the capacitor devices in the region where the laser beam pulse impacts the sample surface. This observation leads to the conclusion that water adsorbed on the sample surface is ionized by the highly focused laser beam. The created radicals than strongly promote the dielectric breakdown of the capacitor devices under gating. This problem was solved by implementing a vacuum chamber in the TR-MOKE setup with optical access to the sample. The vacuum chamber ensures that the water adsorbate on the sample surface is minimized. Indeed, the voltage control of H_{FMR} could only be achieved in vacuum environment, where the measurements shown in figure 4.20 where yielded from the last not destructed capacitor device (of all six TR-MOKE samples).

The established measurement technique described above offers an exciting new route to investigate the true origin of the thickness dependence of $K_4^{\|}$ in ultrathin Fe layers, which is usually attributed to an interface MA contribution [81, 82]. If this assumption holds true one can expect an alteration of $K_4^{\|}$ under gating. By measuring the angular dependence of the voltage control of FMR position one can determine such a voltage dependence of $K_4^{\|}$.

---

[3] ΔK_{eff} can be calculated via the relation: $M_{\mathrm{eff}} = -2K_{\mathrm{eff}}/M_{\mathrm{s}}$, as the shift in H_{FMR} directly yields the change in M_{eff}.

5. Voltage control of magnetic anisotropy in MgO/Fe/Cr

In this chapter the results on the VCMA in ultrathin Fe layers grown on a Cr(001) template are discussed. The chapter has three parts. In the first part the multilayer preparation by MBE is described. In the second part the magnetic properties of the ultrathin Fe layers are characterized by analyzing the out-of-plane magnetization curves measured by MOKE. Finally the results on the VCMA are presented.

5.1. Epitaxial growth

All layers are grown by MBE in the ultrahigh vacuum system described in section 3.1. Figure 5.1 shows a cross sectional cartoon of the prepared multilayer structure. In the following each growth step is discussed in detail. The crystalline quality of the epitaxial films is evaluated by means of RHEED.

The multilayer structure is deposited on “epi-ready” MgO substrates with a (001) surface orientation. The same substrate preparation procedure as described in section 4.1 is utilized. Figures 5.2(a) and (b) show the RHEED pattern of the MgO substrate surface after annealing as well as after deposition of the 6 nm thick buffer layer, respectively. Weak Laue circles are visible in the RHEED pattern of the prepared buffer which indicates a slight polycrystalline surface ordering.

Next a 30 nm thick Cr buffer layer is grown which later serves as template for the ultrathin Fe layers. The deposition is conducted by RTE at a growth rate of 1 ML/min. During the whole preparation procedure the pressure inside the growth chamber stays below 1×10^{-9} mbar. The sample is kept at room temperature up to a film thickness of

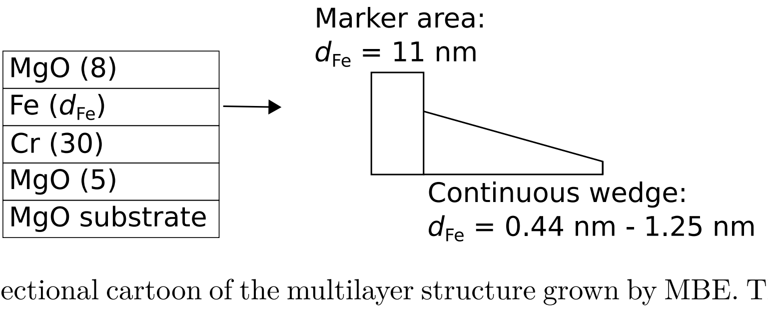

Figure 5.1.: Cross sectional cartoon of the multilayer structure grown by MBE. The numbers in brackets are thicknesses in nm.

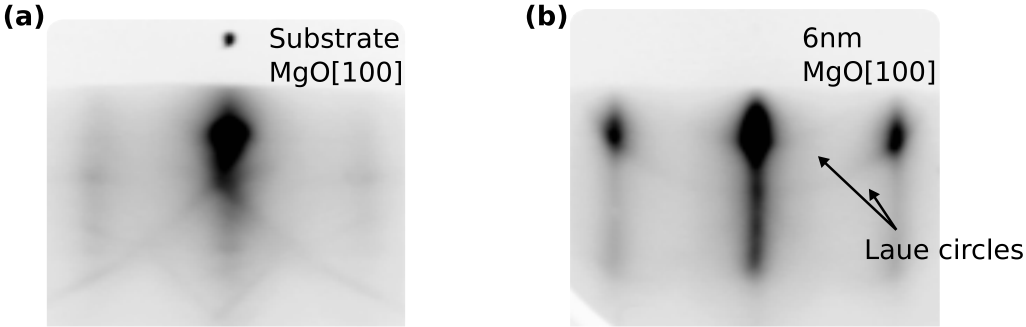

Figure 5.2.: MgO buffer layer preparation. (a) RHEED pattern of the annealed MgO substrate. (b) RHEED pattern after deposition of the 6 nm thick MgO buffer layer. The electron beam is oriented along the [100] direction in both images.

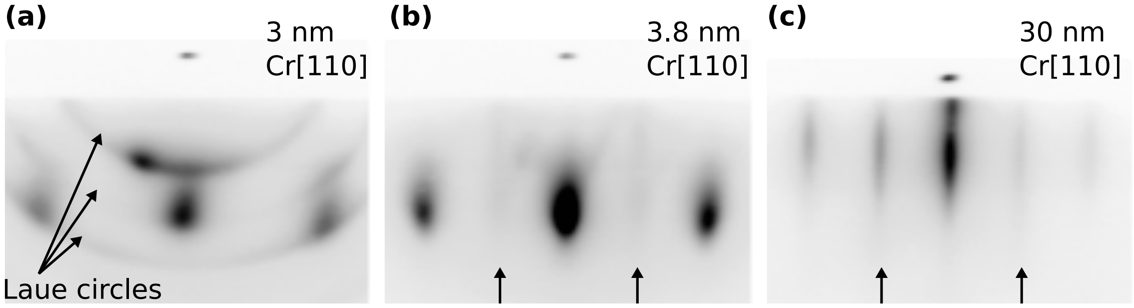

Figure 5.3.: Cr buffer layer preparation. In all three images the electron beam is along the Cr[110] direction. The Cr thickness is (a) 3 nm, (b) 3.8 m and (c) 30 nm.

3 nm. A strong transition towards a polycrystalline ordering is observed in the RHEED pattern, see figure 5.3(a). In order to promote the transition towards the good crystalline morphology the sample is heated to approximately 500 °C (filament power is set to 60 W) while continuing the deposition process. Almost immediately the Laue circles disappear, see figure 5.3(b) where the RHEED pattern of the Cr film is shown for a layer thickness of 3.8 nm. The RHEED pattern of the Cr layer evolves with increasing film thickness into thin streaks showing the excellent surface quality of the prepared buffer, see figure 5.3(c) where the RHEED pattern of the Cr buffer layer at its final thickness of 30 nm is shown.

Superstructure streaks are visible in between the main Cr (1×1) diffraction pattern, which increase in intensity with increasing Cr thickness (see streaks marked by arrows in figure 5.3(b) and (c)). The superstructure streaks are attributed to a $c(2 \times 2)$ adsorbate surface reconstruction as no surface reconstruction for a clean Cr(001) is expected to occur [1]. The reconstruction origin is discussed elsewhere.

Next the ultrathin Fe wedge with a d_{Fe} ranging from 0.44 nm to 1.25 nm is prepared in the same manner as described in section 4.1. The employed marker area has a d_{Fe} of 11 nm. Clear RHEED oscillations are measured during the marker area growth, see figure 6.3(a)[1].

---

[1] Here, the intensity of the (01) diffraction spot is measured where the incident electron beam fulfills the first anti-Bragg condition.

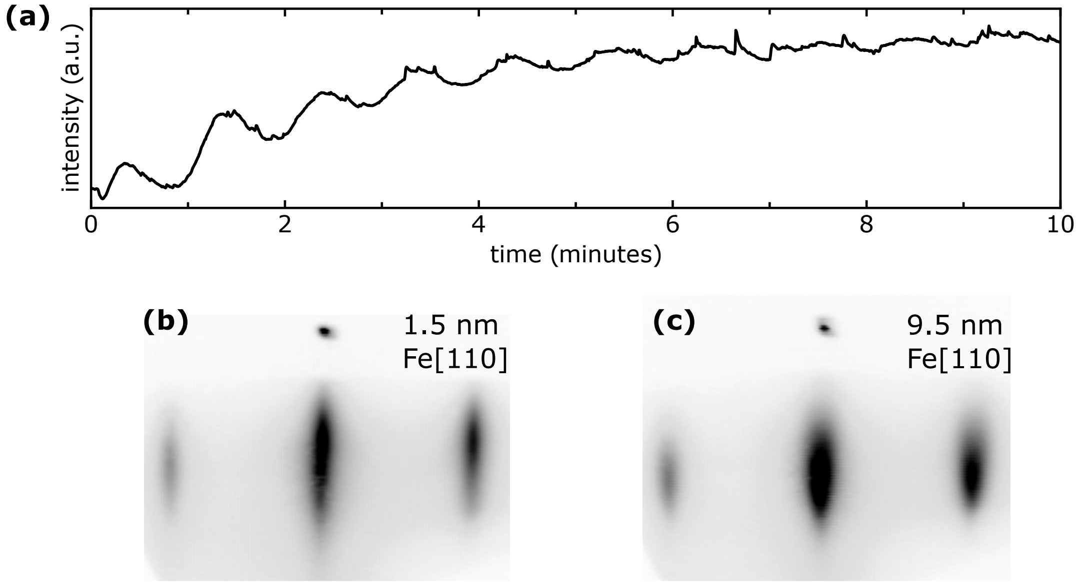

Figure 5.4.: (a) RHEED intensity oscillations of the specular spot intensity measured during the Fe deposition. RHEED pattern of the Fe film where the electron beam is oriented along the Fe[110] direction and d_{Fe} is (b) 1.5 nm and (c) 9.5 nm.

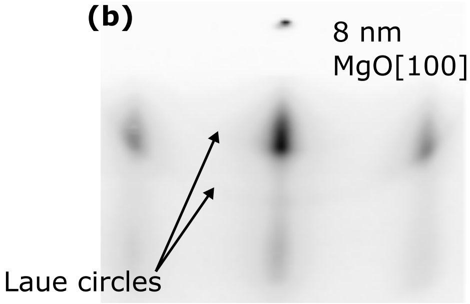

Figure 5.5.: RHEED pattern of the 8 nm thick top MgO dielectric layer. Here the electron beam is oriented along the [100] direction.

The observation of RHEED oscillations shows that the initial growth occurs in the LBL mode and thus one can expect a very smooth Fe surface. The damping of the oscillations is caused by an increase of surface roughness with increasing d_{Fe}, as can be seen from the evolution of the RHEED patterns (see figure 6.3(b) and (c) where the RHEED pattern of the Fe layers with a d_{Fe} of 1.5 nm and 9.5 nm is shown, respectively). Please note that the superstructure streaks are not visible anymore in the RHEED pattern of the prepared Fe layer.

Finally the 8 nm thick MgO dielectric layer is prepared. The growth is conducted in the same manner as described in section 4.1. Very weak Laue rings appear in the RHEED pattern of the prepared MgO layer, see figure 6.5, indicating a slight transition towards a polycrystalline crystal morphology.

5.2. Magnetic properties

The epitaxial Fe layers are characterized by analyzing the out-of-plane magnetization curves measured by MOKE in polar configuration. Strong PMA is found for the thinnest samples and a giant interface MCA is extracted from the $K_{\mathrm{eff}} \cdot d_{\mathrm{Fe}}$ vs. d_{Fe} plot.

Figures 5.6(a-e) show representative out-of-plane magnetization curves. The respective Fe layer film thickness is written as numbers inside each plot. Square out-of-plane hysteresis loops are measured in a d_{Fe} range from 0.40 nm to 0.59 nm. The hysteresis loops clearly show that the respective samples have PMA, which is in accordance with the recent reports of the PMA in epitaxial MgO/Fe/Cr based multilayer structures [1–3, 46]. For a d_{Fe} bigger than ∼0.65 nm the out-of-plane loops are hard axis like, showing that for this d_{Fe} and above the systems easy axis transitions into the sample plane, see figure 5.6(d) and (c). From the out-of-plane hard axis curves, K_{eff} is extracted via the area method, assuming square in-plane magnetization loops. Figure 5.6(f) shows the respective $K_{\mathrm{eff}} \cdot d_{\mathrm{Fe}}$ vs. d_{Fe} data plotted as full black circles. From the linear fit to the data (black solid line in figure 5.6(f)) K_{i} of $1.56\,\mathrm{mJ/m^2}$ and K_{v} of $-2.50\,\mathrm{MJ/m^3}$ are extracted. The giant K_{i} is similar in magnitude to the recent values reported in the literature (for MgO/Fe/Cr based system) [1–3, 46].

Material systems with strong PMA are very interesting from a technological point of view as they yield the high thermal stability needed for the realization of future high density p-MRAM devices. A strong PMA exceeding the values observed in the traditional Co/Pt- [107] and more modern MgO/CoFeB-based multilayers [5] has been theoretically predicted for MgO/Fe bilayer based structures [57, 97]. The PMA in this material system is mainly attributed to the weak Fe-d_3 and O-p_2 interface orbit hybridization [57, 97]. However, it also has been shown that the PMA crucially depends on the (exact amount of) Fe oxidation at the MgO/Fe interface [57, 97]. From an experimental point of view Koo et al. [1] showed that strong PMA in MgO/Fe/Cr based multilayers is only observed if an adsorbate induced c(2 × 2) surface reconstruction is visible in the RHEED pattern of the epitaxial Cr buffer layer (as observed here, see section 5.1). They attribute the observed superstructure to an oxygen adsorbate reconstruction which then is believed to lead to the right oxygen stoichiometry at the MgO/Fe interface yielding PMA [57, 97, 98]. However, more recently Nozaki et al. could show by Auger electron analysis that the c(2 × 2) superstructure appearing in the RHEED pattern of an Cr layer grown on a MgO(001) substrate might as well be carbon adsorbate-induced. They employ annealing temperatures of 800 °C during the Cr buffer preparation which is far higher as than ones employed here (500 °C). It is unclear if the annealing temperature employed here is sufficient to mobilize the carbon impurities implemented in the MgO substrate and lead to their surface segregation through the MgO buffer layer (which is employed as carbon diffusion barrier). In any case, whether oxygen or carbon adsorbate reconstructions induce the c(2 × 2) superstructure observed in the RHEED pattern of the Cr buffer layer, the observation of such surface reconstructions here is confirmed to lead to strong PMA in the successively deposited Fe layers.

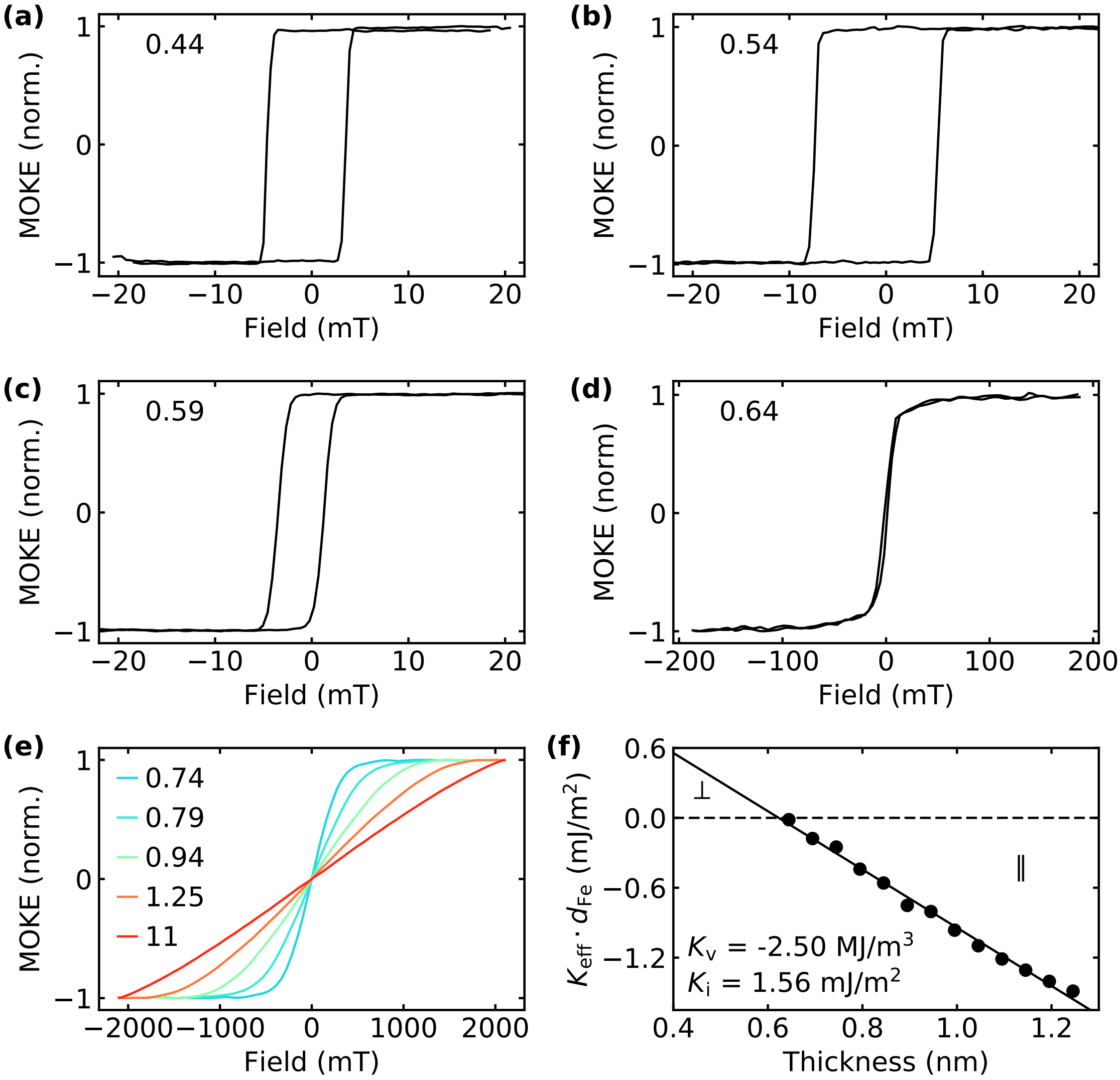

Figure 5.6.: (a)-(e) Out-of-plane magnetization curves measured by MOKE. The Fe thickness is written as number in nanometer inside the figures. (f) $K_{\mathrm{eff}} \cdot d_{\mathrm{Fe}}$ vs. d_{Fe} plot derived via the area method from the hard axis out-of-plane magnetization curves, assuming rectangular in-plane loops.

5.3. Voltage control of magnetic anisotropy

The VCMA is investigated in a capacitor device with d_{Fe} of 0.67 nm. A cartoon showing the cross-sectional capacitor device layout is shown in figure 5.7(a). The device is microfabricated as described in section 4.2. Figure 5.7(b) shows the modulation curve measured on the capacitor device in the modified MOKE setup where U_{g} is modulated by a sinusoidal f_{m} of 37 Hz in between ±10 V. By the area method ΔK_{eff} of 0.4 kJ/m^3 is extracted which corresponds to ξ of 1.0 fJ/Vm.

This VCMA coefficient is quite small as compared to the giant value of 290 fJ/Vm reported by Nozaki et al. for the MgO/Fe/Cr-based material system [46]. A the magnetic

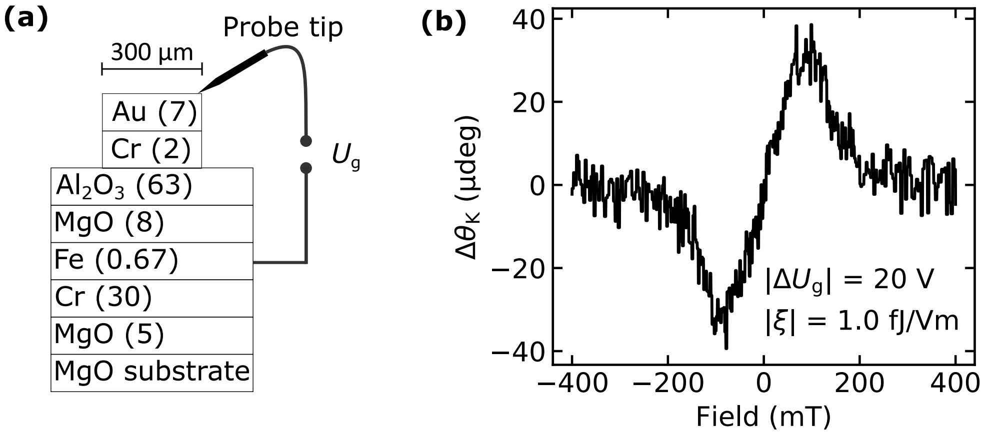

Figure 5.7.: (a) Cross sectional cartoon of the capacitor device with a Fe thickness of 0.67 nm in which the VCMA is measured in the modified MOKE setup. The numbers in brackets are thicknesses in nanometer. (b) Modulation curve measured on the device.

properties of the prepared Fe layers are excellent, with PMA for a Fe thickness from 0.40 nm to 0.59 nm, this result is rather surprising and concludes that the good magnetic properties are not sufficient in order to achieve strong VCMA.

Most likely the reduced VCMA coefficient is related to the preparation of the MgO layer by the homebuilt e-beam evaporator. With this technique a MgO crystal held by a Ta cup is heated by e-beam bombardment, see appendix A for a detailed description of the evaporator. In contrast to most commercial e-beam evaporators, the Ta holder is not cooled and thus a small amount of Ta (or other materials) might evaporate during the MgO layer preparation. This assumption is backed by the RHEED pattern observation during buffer and top MgO layer preparation where a slight transition towards a polycrystalline ordering is visible, see figure 5.2 and 6.5, respectively, which very likely is induced by impurities. For future experiments it is proposed to use alternative deposition methods which promise a higher MgO film purity and thus enhanced VCMA magnitude. These methods could be alternating-current (ac) sputter deposition from a high purity MgO target, or e-beam evaporation of a pure MgO crystal directly placed on a water cooled holder.

6. Voltage control of magnetic anisotropy in MgO/Co/Fe/Au

The VCMA is investigated in a MgO/Co/Fe/Au-based multilayer structure. In the following three sections, first the epitaxial growth, second the magnetic properties and third the results concerning the VCMA are discussed.

6.1. Epitaxial growth

A cross sectional cartoon of the multilayer structure grown by MBE is shown in figure 6.1. As substrate an epitaxial ready MgO(001) wafer with dimensions 10 mm × 10 mm is used. A Fe wedge with d_{Fe} ranging from 0.33 nm to 0.70 nm is prepared across the wafer where at one edge a marker area with d_{Fe} of 5.0 nm is deposited. After the Fe wedge and marker area preparation the sample is covered by a 0.3 nm thin layer of Co. In the following the single growth steps are discussed in more detail where the epitaxial film quality is analyzed by means of RHEED.

The MgO substrate preparation and buffer layer deposition is conducted as described in section 4.1. Figure 6.2 shows the RHEED pattern of the 10 nm thick MgO buffer layer surface where the electron beam is oriented along the [100] direction. Sharp diffraction streaks are observed where the spots of enhanced intensity are perfectly arranged on the zeroth Laue circle. This RHEED pattern shows that a MgO buffer layer with excellent surface quality is prepared.

Next a 10 nm thick Fe seed layer is prepared which is needed to force the (001) surface orientation of the subsequently deposited Au buffer layer [158, 175]. The Fe seed layer is

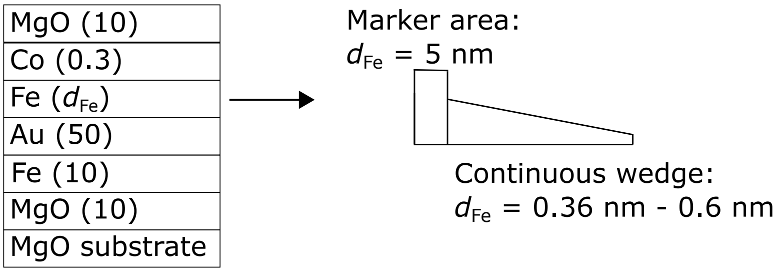

Figure 6.1.: Cross sectional cartoon of the multilayer structure grown by MBE. The numbers in brackets are thicknesses in nanometer.

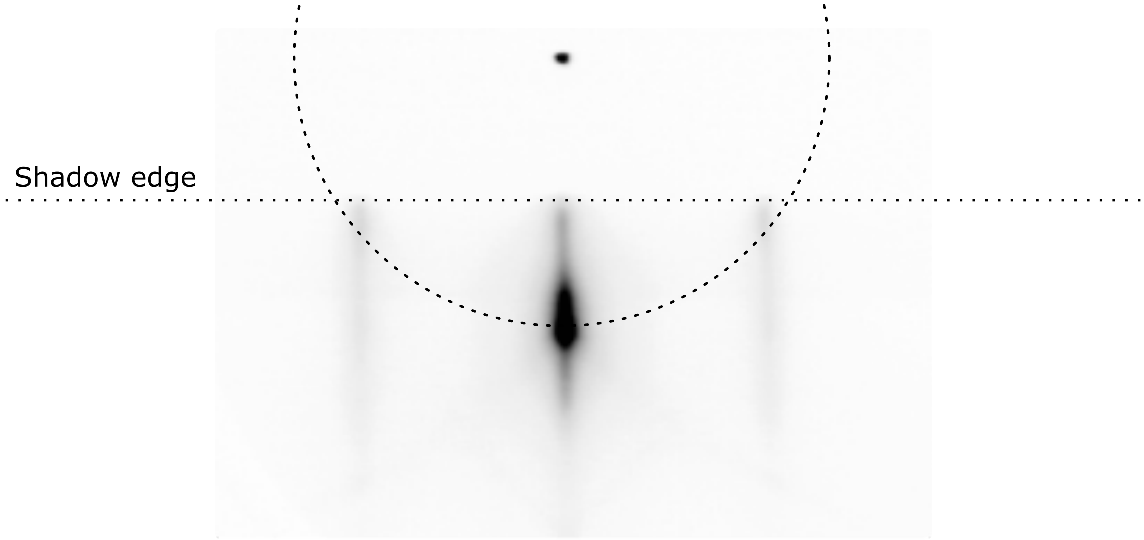

Figure 6.2.: RHEED pattern of the 10 nm thick MgO buffer layer surface where the electron beam is oriented along the [100] direction.

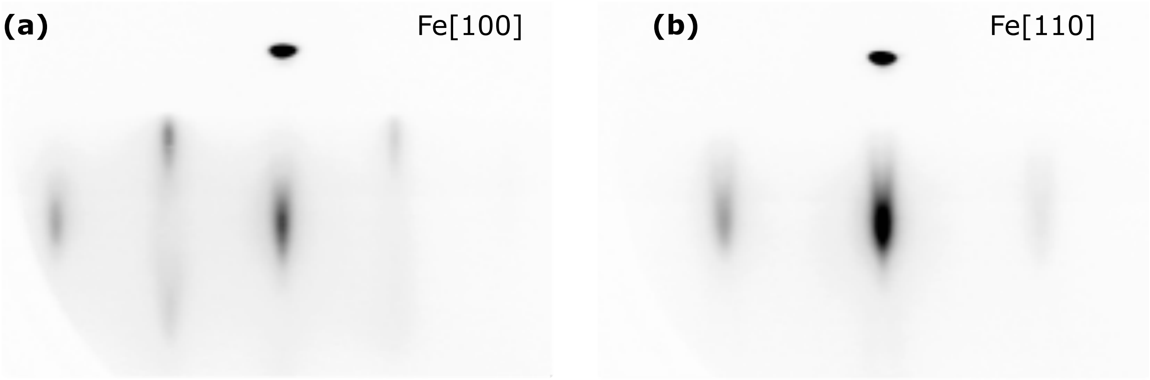

Figure 6.3.: RHEED pattern of the 10 nm thick Fe seed layer where the electron beam is oriented along the (a) [100] and (b) [110] direction.

deposited by RTE at a growth rate of 1.5 ML/min where the sample temperature is held at 150 °C. During deposition, the system pressure stays below 1×10^{-9} mbar. Figure 6.3 shows the RHEED pattern of the 10 nm Fe layer along the (a) [100] and (b) [110] direction. Clearly crystalline ordering with a 3D terminated surface is yielded. Furthermore symmetric fan-out-streaks are visible in the RHEED pattern along the [110] orientation. The origin of these fan-out-streaks is discussed later in the text.

Next the 50 nm thick Au buffer layer is deposited in the same manner as described in section 4.1. Figure 6.4 shows the prepared Au layer RHEED pattern along the (a) [100] and (b) [110] direction. Strong symmetric fan-out-streaks appear in the RHEED pattern. The fan-out-streaks are strongest along the Au[100] orientation and completely disappear when the electron beam is oriented along the Au[110] orientation. Fan-out-streaks of such symmetry are a well known phenomenon in MBE growth and attributed to a rectangular

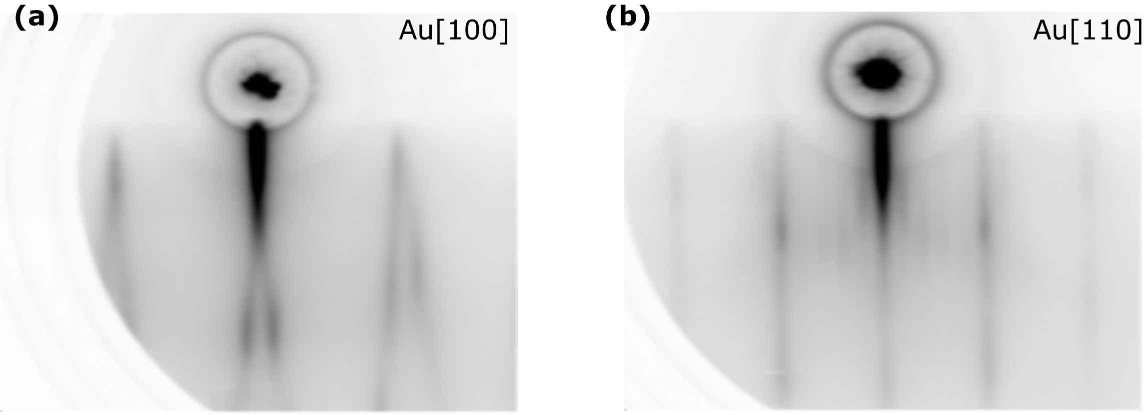

Figure 6.4.: RHEED pattern of the 50 nm thick Au layer where the electron beam is oriented along the (a) [100] and (b) [110] direction.

network of line defects oriented along the Au⟨110⟩ directions [146, 147]. The formation of such a network of line defects during the deposition of a Au film upon a Fe(001) template would be rather surprising as the epitaxial relation Au[100]||Fe[110] yields a very small η of only 0.5 %. Strain relaxation processes, which lead to the formation of line defects are more likely to occur for the Fe deposition upon the MgO(001) surface where η is 3.8 % for the epitaxial relation: Fe[100]||MgO[110]. Thus it is assumed that the misfit dislocations are already formed during the Fe seed layer preparation and then adapted by the successively deposited Au layer. Clear 5×1 surface reconstruction are visible in the RHEED pattern of the Au buffer where the electron beam is oriented along the [110] orientation. The observation of these superstructures shows that, despite the misfit dislocations, a smooth Au surface has been prepared. Unfortunately the Fe and Co layers RHEED patterns could not be recorded, as the RHEED system was not working at the time of film preparation. In the following the expected growth of both layers is discussed with respect to the literature and the experimental results described in this thesis (section 4.1).

The Fe wedge and marker area are prepared in the exact same manner as described in section 4.1. A very good surface quality of the Fe layer is expected upon deposition on a flat Au(001) surface with respect to both the literature [167–171] and the results described in section 4.1.

The 0.3 nm thin Co layer is prepared by means of RTE at a growth rate of 1 ML/min. The sample is held at room temperature and the pressure inside the MBE chamber stays below 1×10^{-9} mbar during deposition. Bulk Co stabilizes in the hexagonal closed package (hcp) crystal structure. However, it has been shown that one can prepare ultrathin Co layers with bcc structure by epitaxial growth on lattice matched substrates [187, 188]. The lattice constant of bcc Co can be estimated by the following procedure. It is well known that $\mathrm{Fe}_{(\mathrm{x})}\mathrm{Co}_{(1-\mathrm{x})}$ alloys grow in the bcc phase where $1 \geq x \geq 0.25$ [187]. From extrapolating the alloy composition vs. lattice constant dependency, the bcc Co lattice constant is estimated to be 2.81 Å [187]. Thus a reasonably low η of 2.1 % is achieved for the epitaxial growth

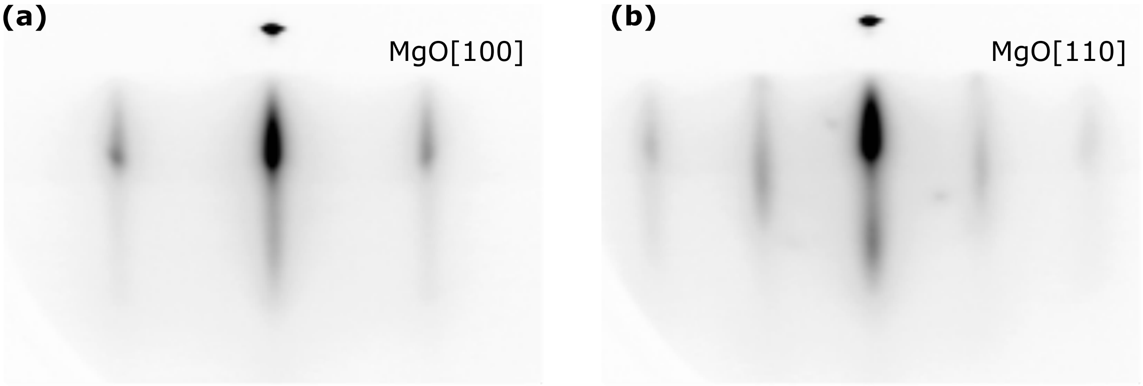

Figure 6.5.: RHEED pattern of the 10 nm thick top MgO dielectric layer where the electron beam is oriented along the (a) [100] and (b) [110] direction.

of a bcc Co layer upon a Fe(001) surface template. However, Dekoster et al. showed that ultrathin Co layers grown upon a Fe(001) template only adapt the metastable bcc crystal structure for the deposition at an elevated temperature of 175 °C [188]. Future RHEED investigations are needed in order to gain insight into the crystal structure of the prepared Co layer.

Finally the 10 nm thick MgO dielectric layer is prepared in the same manner as described in section 4.1. Figure 6.5 shows the (expected) RHEED patterns of the MgO film after deposition where the electron beam is along the (a) [100] and (b) [110] direction. Both RHEED pattern show very narrow diffraction streaks indicating the smooth surface of the prepared MgO dielectric layer.

6.2. Magnetic properties

The magnetic properties of the Co/Fe layers is investigated by analyzing the out-of-plane magnetization curves measured by polar MOKE.

The magnetization curves are typical hard axis curves where the total magnetic layer thickness ranges from 0.71 nm to 0.9 nm (see figure 6.6(a)). In this thickness range K_{eff} is extracted via the area method assuming rectangular in-plane easy axes loops. Furthermore the saturation magnetization of the Co/Fe sample for each total magnetic layer thickness is estimated as the weighted (by the single layer thickness) average of the respective Fe and Co bulk values (1720 kA/m for Fe and 1370 kA/m for Co [73]). The $K_{\mathrm{eff}} \cdot d$ vs. d dependency yielded by this procedure (where d is the total magnetic layer thickness) is plotted in figure 6.6(b) as full black circles. From the linear fit to the data K_{i} of $1.20\,\mathrm{mJ/m^2}$ and K_{v} of $-1.98\,\mathrm{MJ/m^3}$ is determined.

The enhancement of K_{i} yielded here, as compared to the MgO/Fe/Au based multilayer (see section 4), shows that the additional deposited Co layer increases the MA contributions favoring PMA. PMA has been reported by Shiota et al. for the $\mathrm{Fe_{80}Co_{20}}$ alloy films with a thickness of 0.50 nm and 0.40 nm [7]. However, PMA in the Co/Fe bilayers investigated

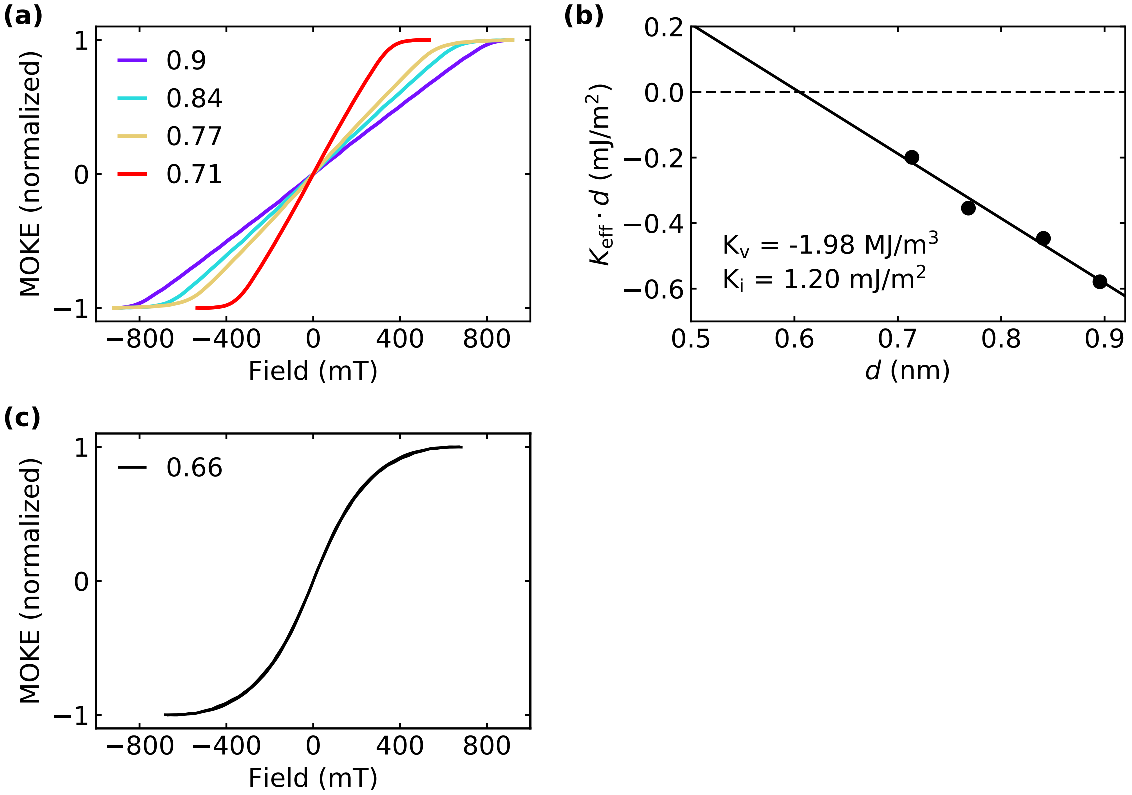

Figure 6.6.: (a) Out-of-plane magnetization curves measured on the Fe/Co wedge by polar MOKE. The numbers written in the figure are the total magnetic layer thicknesses in nanometer. (b) $K_{\mathrm{eff}} \cdot d$ vs. d plots extracted via the area method from the curves shown in (a). Out-of-plane curve for a combined Fe/Co thickness of 0.66 nm.

here could not be achieved. In contrast, the out-of-plane magnetization curves of the Co/Fe layer start to deviate from the ideal sharp saturation behaviour for decreasing Fe thickness, see figure 6.6(c), where the Co/Fe out-of-plane curve for a total magnetic layer thickness of 0.66 nm is shown. The rounded form of this curve shows that the magnetic layer is roughened and thus the observed magnetization reversal is the average of several contributing layers with different effective film thicknesses. This finding indicates a growth of the Co layer with hcp crystal structure, which due to the undefined epitaxial relation to the Fe(001) template, might well lead to a 3D surface.

6.3. Voltage control of magnetic anisotropy

The VCMA in a capacitor devices with total magnetic layer thicknesses of 0.71 nm is measured via the modulation technique.

Figure 6.7(a) shows a cross sectional cartoon of the capacitor device layout. The device microfabrication is conducted as described in section 4.2. The modulation curve is measured in the modified MOKE setup where U_g is modulated by a sinusoidal f_m of 37 Hz inbetween

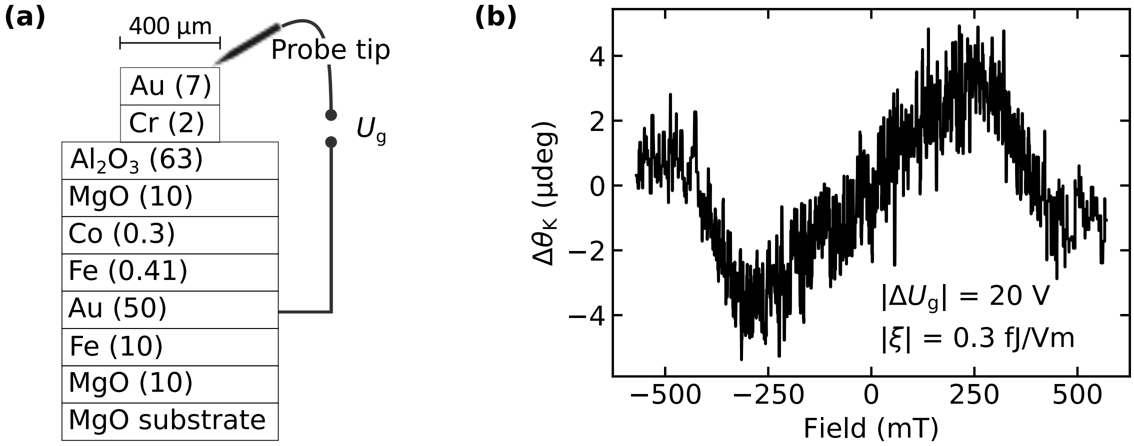

Figure 6.7.: (a) Cross sectional cartoon showing the layer structure of the capacitor device with a Co/Fe layer thickness of 0.71 nm. The numbers in brackets are thicknesses in nanometer (b) Modulation curve measured on the capacitor device.

±10 V. The yielded curves are shown in figure 6.7(b). By the area method ξ of 0.3 fJ/Vm is extracted. The films saturation magnetization is estimated as the weighted average of the respective Fe and Co bulk values (1720 kA/m for Fe and 1370 kA/m for Co [73]), resulting in an average saturation magnetization of 1573 kA/m.

The VCMA coefficient is significantly reduced as compared to the values reported in the literature [7]. Most likely the reduction is caused by a 3D Co layer growth, as indicated by the magnetic characterisation. In future a growth of the Co layer at elevated sample temperatures is proposed in order to promote the well defined pseudomorphic growth upon the Fe(001) surface template [188] and thus improve the VCMA.

7. Summary

A UHV system with MBE growth chamber was developed and constructed as part of this thesis. With this system the epitaxial growth procedure of three different dielectric/ferromagnet metal heterostructures with VCMA was established. The structures are based on MgO/Fe/Au, MgO/Fe/Cr and MgO/Co/Fe/Au multilayers. Table 7.1 gives an overview of the most important magnetic and VCMA properties obtained by the experiments conducted in this thesis. In the following a summary of the experimental procedure, the experimental results, and respective conclusions for each material system are given.

MgO/Fe/Au

The RHEED analysis conducted during the preparation of the MgO/Fe/Au-based multilayers shows the excellent crystalline quality of the samples.

The magnetic properties of the Fe wedge with thickness ranging from 0 nm to 1 nm are investigated in detail by analyzing the in- and out-of-plane magnetization curves measured by MOKE and furthermore the FMR angular and frequency dependencies measured by TR-MOKE. The analysis reveals the expected MCA of a cubic system. An additional, strong, uniaxial in-plane MA contribution is found. This MA is attributed to a vicinal substrate surface. The interface MCA of the system is revealed, which leads to PMA in the sample where the Fe thickness is in between 0.3 nm and 0.4 nm. This result shows the excellent properties of the ultrathin Fe layers.

The VCMA is investigated in detail by different techniques. The gate voltage is modulated by a frequency generator and the MOKE response is measured via LIA while sweeping an external magnetic field. Furthermore static magnetization curves and FMR spectra are measured with different applied gate voltages.

Comparing the VCMA coefficient measured with the modulation technique (where the gating time is <1 s) and by evaluating magnetization curves measured in a static manner with different applied gate voltages (where the gating time is ∼10 min) yields an increase in the effects magnitude of approximately 300 %. A hysteresis is observed in the gate voltage vs. VCMA magnitude dependency measured in a static manner. In contrast, a linear relationship is obtained in the gate voltage vs. VCMA magnitude dependency measured via the modulation technique. These findings imply that charge trapping and/or magneto-ionic effects, which have long transient times, strongly affect the VCMA measured in a static manner. By analyzing the modulation frequency dependence of the VCMA coefficient measured by the modulation technique it is shown that the onset of the charge trapping

	MgO/Fe/Au	MgO/Fe/Cr	MgO/Co/Fe/Au
d_{VCMA} (nm)	0 - 1	0.67	0.71
$\lvert\xi_{\text{max}}\rvert$ (fJ/Vm)	2.4	1.0	0.3
d_{magn} (nm)	0 - 1	0.44 - 1.25	0.66 - 0.90
K_{i} (mJ/m^2)	0.59, 0.70	1.59	1.20
K_{v} (kJ/m^3)	-1.23, -1.40	-2.50	-1.98
PMA	✓	✓	

Table 7.1.: Summary of the interface MA constant K_{i}, volume MA constant K_{v} and the maximum VCMA coefficient $\lvert\xi_{\text{max}}\rvert$ yielded for the three material systems investigated in this thesis. The value d_{VCMA} and d_{magn} gives the total magnetic layer thickness (range) in which the VCMA and magnetic properties are investigated, respectively. Two values K_{i} and K_{v} are given for the MgO/Fe/Au based material system. These values are obtained by MOKE and FMR measurements, respectively. The row PMA is denoted by a checkmark if selfsame is observed.

and/or magneto-ionic effects occur for a gating time ≈1.3 ms.

The VCMA thickness dependence is measured quantitatively in a Fe thickness range from 0.5 nm to 1 nm. An unexpected increase of the VCMA coefficient from 1.1 fJ/Vm to 2.4 fJ/Vm over the investigated thickness range is observed. This finding stands in stark contrast to the expected behavior for the electronic VCMA which is located at the topmost atomic layer of the ferromagnetic film. As explanation, two mechanisms are proposed. An inverse piezo electric effect in the MgO dielectric layer, which would lead to an alteration of the Fe layers (volume) MEA. Or a thickness-dependent Au segregation to the Fe layer surface during epitaxial growth, which leads to a decrease of electric field shielding and consequently an increase of the VCMA with increasing Fe thickness. Thickness-dependent film strain as origin of this unexpected observation is excluded due to the linear $K_{\text{eff}} \cdot d_{\text{Fe}}$ vs. d_{Fe} dependence.

Furthermore preliminary measurement results attained by TR-MOKE are shown where the FMR position is tuned upon gating. The aim of this experiment is to measure the angular dependence of the FMR position upon gating, which will give insight into the interfacial nature of the in-plane MCA.

MgO/Fe/Cr

The very good epitaxial quality of the prepared Fe wedge is confirmed by RHEED oscillations. A slight transition towards a polycrystalline morphology is observed in the RHEED pattern of the buffer and topmost MgO layer.

The magnetic properties of the Fe wedge layer are investigated in a thickness range from 0.44 nm to 1.27 nm by analyzing the out-of-plane magnetization curves measured by MOKE. PMA is found in Fe layers with a thickness ranging from 0.44 nm to 0.60 nm. A giant K_{i} of 1.56 mJ/m^2 is extracted from the $K_{\text{eff}} \cdot d_{\text{Fe}}$ vs. d_{Fe} plot, showing the superior magnetic properties of the prepared Fe layers.

Despite the very promising magnetic properties only a rather small VCMA coefficient of 1.0 fJ/Vm is measured in a capacitor device with a Fe layer thickness of 0.67 nm. This result is attributed to an impurity induced, imperfect MgO layer prepared by the homebuilt e-beam evaporator. For future experiments it is proposed to utilize alternative deposition methods like ac sputtering from a high purity MgO target, or e-beam evaporation of MgO placed in a water cooled holder. These methods could improve the purity of the prepared MgO layers and increase the VCMA magnitude.

MgO/Co/Fe/Au

An epitaxial Fe wedge is prepared in a similar manner as in case of the MgO/Fe/Au sample. An additional 0.3 nm thin Co layer is deposited on top of the Fe wedge.

The magnetic properties of the Co/Fe layers are investigated in a magnetic layer thickness range of 0.66 nm to 0.90 nm. From the $K_\mathrm{eff} \cdot d$ vs. d plot (where d is the total magnetic layer thickness) $K_\mathrm{i} = 1.2\,\mathrm{mJ/m^2}$ is extracted. The enhancement of K_i as compared to the Fe layers of the MgO/Fe/Au-based material system, in principle shows that the additional Co layer enhances the MA contributions favoring PMA. However, a very rounded magnetization curve is observed for the thinnest sample where d is 0.66 nm. This finding is attributed to an inhomogeneous Co layer growth.

The VCMA is investigated via the modulation technique in a capacitor device with a Co/Fe layer thickness of 0.71 nm. A small VCMA coefficient of only 0.3 fJ/Vm is extracted and attributed to the 3D growth of the Co layer. An improved Co layer deposition procedure is proposed which in future should allow to prepare smoother layers with enhanced VCMA.

A. Homebuilt thin film evaporators

As part of this thesis three types of evaporators used for the deposition of thin films in (ultra) high vacuum growth chambers have been developed and manufactured: Two types of resistive thermal evaporators (RTE) employed for the growth of low vapor pressure metals, as well as one type of electron-beam evaporator used to deposit oxides like MgO or Al_2O_3. In the following a detailed description of the three evaporators is given.

A.1. Resistive thermal evaporators

Two types of RTEs are designed: The first design is based on resistive heating through a Ta sheet filament and the second design on resistive heating through a solenoid W filament.

Tantalum sheet filament

Figure A.1(a) shows a photograph of the RTE based on heating through a Ta sheet filament. The RTE is built upon a CF 35 high power feed-through with additional c-type thermocouple feed-through. The evaporator is mainly used in the MBE chamber where it is embedded into a liquid N_2-cooled cryo shroud. Due to the special requirements of the shroud the evaporator has a slim, tower like design.

Figure A.1(b) shows a cross sectional 3D CAD drawing of the evaporator unit. The basic operation principle is as follows. Low vapor metals like Au, Ag, Cr, Cu, Al, Co, Fe, Ni are placed in a crucible which is made either out of Al_2O_3 or pyrolitic BN (PBN). The crucible has a diameter and height of 12 mm, where the wall thickness is 1 mm. The crucible is resistively heated by passing current through a 50 µm thin Ta sheet which surrounds the crucible. In figure A.1(c) only the sheet filament and crucible of the evaporator are shown in order to clarify the heating principle. The crucible and Ta sheet filament are enclosed by a 100 µm thin Ta sheet which acts as a radiation shield and significantly enhances the efficiency of the evaporator. The crucible temperature is estimated by a c-type thermocouple attached close to the bottom of the crucible.

These evaporators can be supplied with up to 250 Watts of power, while remaining stable. A typical current voltage relation under operation would be 4 V and 50 A. With these parameters the evaporator yields rates in the order of 1 ML/min. The exact rate obviously depends on the material and sample-source distance (which in the MBE system is approximately 200 mm).

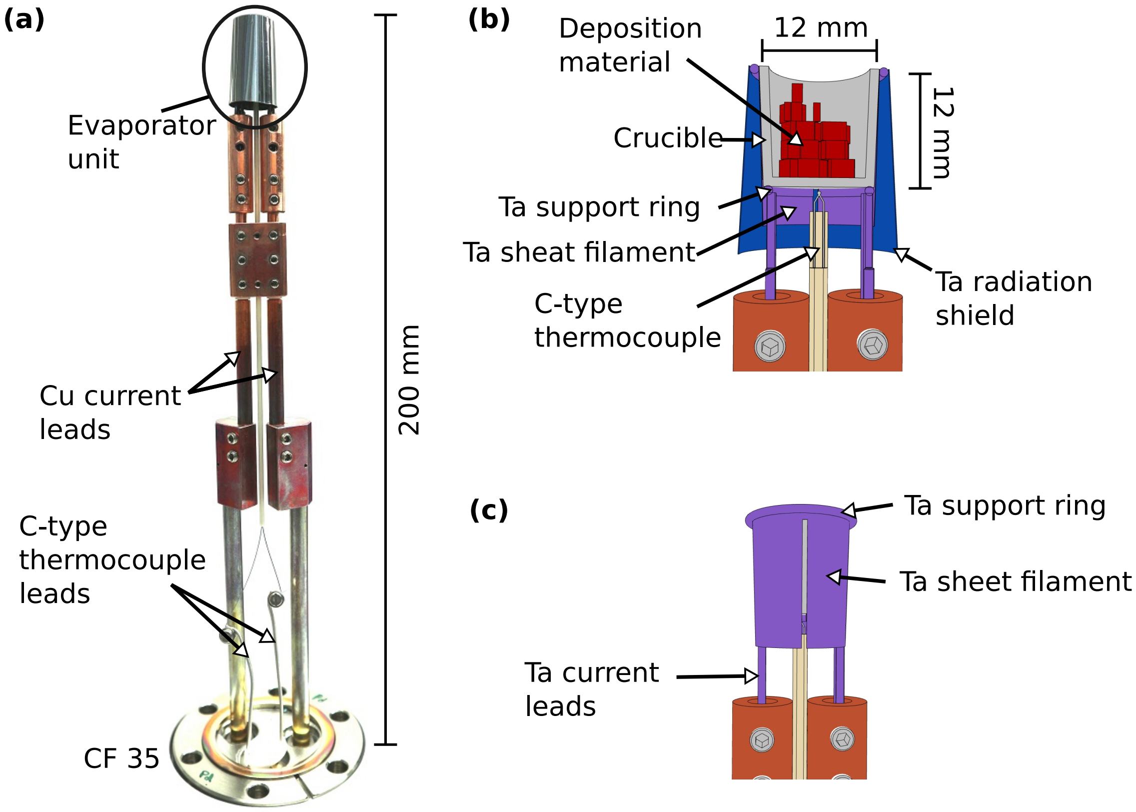

Figure A.1.: (a) Photography of the RTE based on heating through a Ta sheet filament. (b) Cross sectional 3D CAD drawing of the evaporation unit. (c) 3D CAD drawing of the evaporator unit without radiation shield.

Tungsten solenoid filament

Figure A.2(a) shows an image of the RTE based on heating through a solenoid W filament, without radiation shield. In figure A.2(b) the evaporator is shown with Ta radiation shield. The evaporator is built upon a CF 35 high power Cu feed-through. The evaporator unit consists of Al_2O_3 or PBN crucibles surrounded by a solenoid W filament. In order to increase the efficiency, the evaporator unit is surrounded by a 100 µm thick Ta radiation shield.

These evaporators are very robust and can be powered easily with 400 W with no need for concern about a thermal breakdown. This evaporator is employed in the metallization chamber for the deposition of low vapor metals like Au, Ag, Cr, Cu, Al, Co, Fe, Ni. Typical rates which are achieved here at a sample source distance of 240 mm are in the order of 1 Å/s.

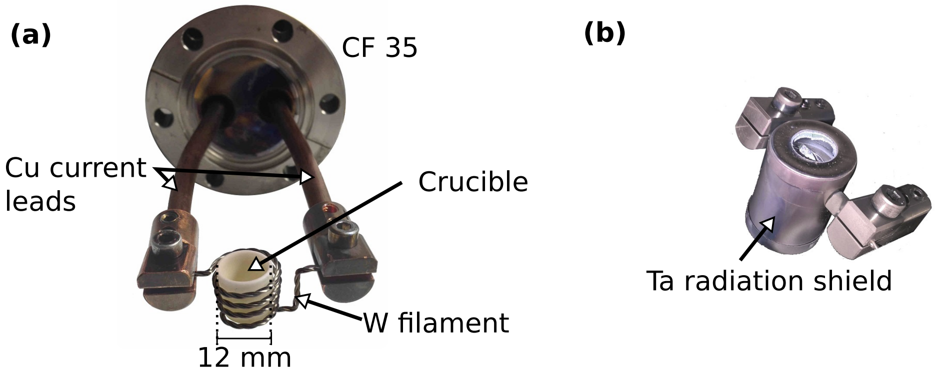

Figure A.2.: (a) Photography of the RTE based on heating through a W solenoid filament, without radiation shield. (b) Photography of a similar evaporator with radiation shield.

A.2. Electron-beam evaporator

A.3(a) shows a 3D CAD drawing of the electron-beam evaporator. The slim tower-like design is attributed to the MBE shroud dimensions. The e-beam evaporator is built upon a CF 35 flange with four power feed-throughs. Figure A.3(b) shows an image of the e-beam evaporation unit (marked by the circle in figure A.3(a)). A high purity MgO crystal rod with a diameter 6 mm and height of 10 mm is clamped by a 2 mm high cup made of Ta. The cup is held by a 1 mm diameter Ta rod, which also serves as a high voltage lead. Electrons are supplied via a 150 µm diameter tungsten wire filament spot-welded onto a 1 mm diameter Ta rod. A W wire mounted on the radiation shield is used as a form stabilizing support for the filament. The Ta radiation shield is supported by a 1 mm diameter Ta rod and is mounted 6 mm above the MgO crystal.

During operation 2 A of filament current are supplied by a voltage of approximately 20 V. The MgO crystal is biased with 1 kV, where MgO crystal and filament share a common ground. Under these conditions typically an emission current of 40 mA is measured which yields a rate of approximately 2 ML/min.

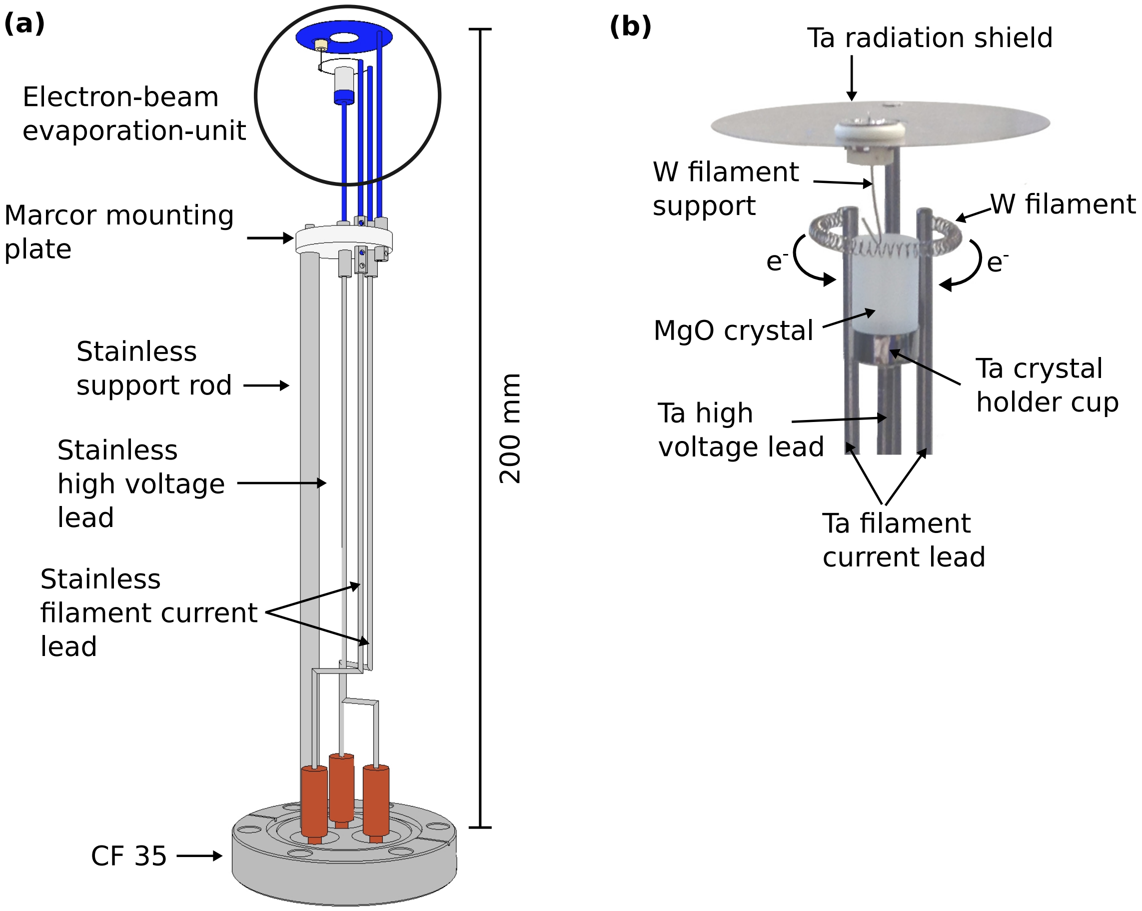

Figure A.3.: (a) 3D CAD drawing of the electron-beam evaporator constructed as part of this thesis. (b) Image of the evaporation unit.

B. Sample microfabrication - recipes

In the following two sections the microfabrication to the TR-MOKE and MOKE devices is described.

B.1. TR-MOKE devices

In total six TR-MOKE devices are microfabricated on the 5 mm × 10 mm epitaxial CW sample. Figure B.1 shows an optical microscope image of the sample with microfabricated devices, before they are separated by diamond saw cutting. The devices are microfabricated by means of electron beam lithography, Ar^+-ion milling, metal deposition and lift-off technique. Figure B.2(a-c) shows CAD drawings[1] of the single lithography steps, arranged in the order of the process progression. The figures denoted by primed letters are magnified views. In the following the single microfabrication steps are described in detail.

1. Dielectric passivation

A 37.5 nm thick Al_2O_3 layers is deposited by ALD in the Savannah 100 system at a reactor temperature of 80 °C. This layer later enables the leakage current free gating of the capacitor structures.

2. Coplanar waveguide and magnetic element

The coplanar waveguide and magnetic elements are defined by electron beam lithography and subsequently milled out by employing Ar^+-ion sputtering. The structures are colored blue in the CAD drawings shown in B.2. In the following the single steps of the microfabrication procedure are listed in the order of their appearance:

- Adhesion promoter (Allresist Ar 300-80), spin coated at 4000 RPM (1 min), tempered at 150 °C (2 min), rinsed with aceton and isopropanol, dried.
- Negative e-beam resist (Allresist AR-N 7520.18), spin coated at 6000 RPM (1 min), tempered at 80 °C (2 min).
- EBL, acceleration voltage 20 kV, dose 100 $\mu C/cm^2$.
- Developed in AR 300-47 (3 min), rinsed in distilled water, dried.

---

[1] Utilizing the eDraw CAD software from nanonics

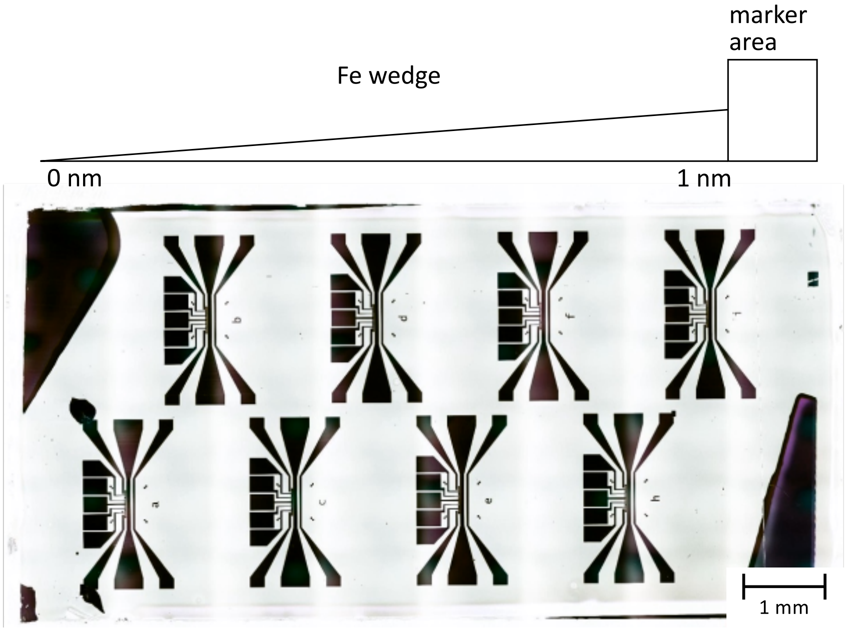

Figure B.1.: Microfabricated TR-MOKE devices on the CW sample.

- Ar^+-ion milling, acceleration voltage 750 V, Ar background pressure 1×10^{-5} mbar, endpoint detection by SIMS
- Resist removal by aceton (12 h), rinsed with isopropanol, dried.

3. Top gate

Four semitransparent top gates are microfabricated on top of the magnetic element placed in between signal and ground line. The top gates are colored green in the CAD drawing shown in figure B.2. The single microfabrication steps are:

- Positive e-beam resist (Allresist AR-P 641.09), spin-coated at 6000 RPM (1 min), tempered at 150 °C (2 min).
- EBL, acceleration voltage 20 kV, dose 220 $\mu C/cm^2$.
- Developed in MIBK:H_2O | 1:1 (10 sec), rinsed in isopropanol, dried.
- Thermal evaporation of 2 nm Cr and 7 nm Au in the metallization chamber.
- Lift-off in aceton (12 h), rinsed with isopropanol, dried.

4. Crosslinked PMMA patch

A crosslinked PMMA patch is used to isolate bottom from top electrode. The PMMA patch is colored purple in the CAD drawing shown in figure B.2. The microfabrication of the PMMA patch involves following steps:

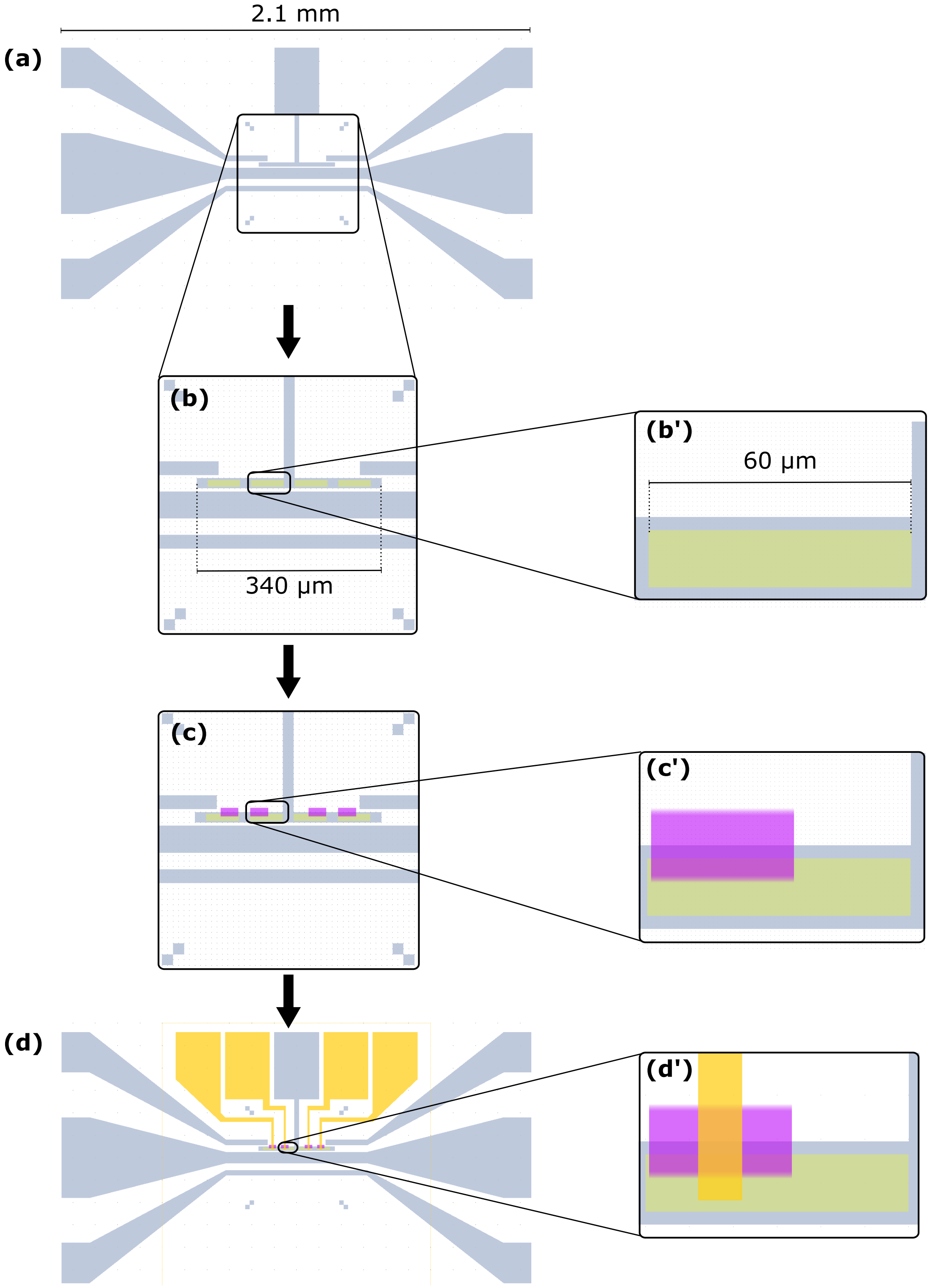

Figure B.2.: CAD (eDraw) drawings of the lithographic structures employed in the microfabrication of the TR-MOKE device. The magnetic element and coplanar waveguide are colored blue, the top gates green, the PMMA insulating patch purple and the top gate yellow. Figure (a-d) are arranged in the order of the lithography process progression. The figure denoted by primed letters are magnified views.

- Positive e-beam resist (Allresist AR-P 641.07), spin coated at 6000 RPM (1 min), tempered at 150 °C (2 min).
- EBL, acceleration voltage 20 kV, dose 18 000 µC/cm^2.
- Rinsed in aceton and isopropanol, dried.

The cross-linked PMMA patch has a thickness of ∼80 nm.

5. Top gate leads

The top gate is contacted by Au leads. The leads are colored yellow in the CAD drawing shown in figure B.2. In the following the microfabrication steps procedure are listed:

- Positive e-beam resist (Allresist AR-P 641.09), spin coated at 6000 RPM (1 min), tempered at 150 °C (2 min).
- EBL, acceleration voltage 20 kV, dose 200 µC/cm^2.
- Developed in MIBK:H_2O | 1:1 (10 sec), rinsed in isopropanol, dried.
- Thermal evaporation of 10 nm Cr and 110 nm Au in the metallization chamber.
- Lift-off in aceton (12 h), rinsed with isopropanol, dried.

B.2. MOKE devices

Multiple capacitor devices are microfabricated on both the CW and SW epitaxial sample with dimensions 5 mm × 10 mm. An optical microscope image of the CW sample with capacitor devices is shown in figure 4.7. In the following the single microfabrication steps are described in detail.

1. Dielectric passivation

As a first step 62.5 nm of Al_2O_3 are deposited by ALD in the Savannah 100 system at a reactor temperature of 80 °C. This layer later enables the leakage current free gating of the capacitor structures.

3. Top gate

Multiple semitransparent top gates with a diameter of 400 µm are microfabricated on top of the CW sand SW ample. The microfabrication includes the following steps:

- Positive e-beam resist (Allresist AR-P 641.09), spin-coated at 6000 RPM (1 min), tempered at 150 °C (2 min).
- EBL, acceleration voltage 20 kV, dose 220 µC/cm^2.

- Developed in MIBK:H_2O | 1:1 (10 sec), rinsed in isopropanol, dried.
- Thermal evaporation of 2 nm Cr and 7 nm Au in the metallization chamber.
- Lift-off in aceton (12 h), rinsed with isopropanol, dried.

Bibliography

1. Koo, J. W., Mitani, S., Sasaki, T. T., Sukegawa, H., Wen, Z. C., Ohkubo, T., Niizeki, T., Inomata, K. & Hono, K. Large perpendicular magnetic anisotropy at Fe/MgO interface. *Appl. Phys. Lett.* **103,** 192401 (2013).
2. Lambert, C.-H., Rajanikanth, A., Hauet, T., Mangin, S., Fullerton, E. E. & Andrieu, S. Quantifying perpendicular magnetic anisotropy at the Fe-MgO(001) interface. *Appl. Phys. Lett.* **102,** 122410 (2013).
3. Okabayashi, J., Koo, J. W., Sukegawa, H., Mitani, S., Takagi, Y. & Yokoyama, T. Perpendicular magnetic anisotropy at the interface between ultrathin Fe film and MgO studied by angular-dependent x-ray magnetic circular dichroism. *Appl. Phys. Lett.* **105,** 122408 (2014).
4. Yuasa, S., Nagahama, T., Fukushima, A., Suzuki, Y. & Ando, K. Giant room-temperature magnetoresistance in single-crystal Fe/MgO/Fe magnetic tunnel junctions. *Nat. Mater.* **3,** 868–871 (2004).
5. Ikeda, S., Miura, K., Yamamoto, H., Mizunuma, K., Gan, H. D., Endo, M., Kanai, S., Hayakawa, J., Matsukura, F. & Ohno, H. A perpendicular-anisotropy CoFeB–MgO magnetic tunnel junction. *Nat. Mater.* **9,** 721–724 (2010).
6. Maruyama, T. *et al.* Large voltage-induced magnetic anisotropy change in a few atomic layers of iron. *Nat. Nanotechnol.* **4,** 158–161 (2009).
7. Shiota, Y., Maruyama, T., Nozaki, T., Shinjo, T., Shiraishi, M. & Suzuki, Y. Voltage-Assisted Magnetization Switching in Ultrathin Fe 80 Co 20 Alloy Layers. *Appl. Phys Express* **2,** 063001 (2009).
8. Endo, M., Kanai, S., Ikeda, S., Matsukura, F. & Ohno, H. Electric-field effects on thickness dependent magnetic anisotropy of sputtered MgO/Co40Fe40B20/Ta structures. *Appl. Phys. Lett.* **96,** 212503 (2010).
9. Ha, S.-S., Kim, N.-H., Lee, S., You, C.-Y., Shiota, Y., Maruyama, T., Nozaki, T. & Suzuki, Y. Voltage induced magnetic anisotropy change in ultrathin Fe80Co20/MgO junctions with Brillouin light scattering. *Appl. Phys. Lett.* **96,** 142512 (2010).
10. Nozaki, T., Shiota, Y., Shiraishi, M., Shinjo, T. & Suzuki, Y. Voltage-induced perpendicular magnetic anisotropy change in magnetic tunnel junctions. *Appl. Phys. Lett.* **96,** 022506 (2010).

11. Bonell, F., Murakami, S., Shiota, Y., Nozaki, T., Shinjo, T. & Suzuki, Y. Large change in perpendicular magnetic anisotropy induced by an electric field in FePd ultrathin films. *Appl. Phys. Lett.* **98,** 232510 (2011).

12. Chiba, D., Fukami, S., Shimamura, K., Ishiwata, N., Kobayashi, K. & Ono, T. Electrical control of the ferromagnetic phase transition in cobalt at room temperature. *Nat. Mater.* **10,** 853–856 (2011).

13. Seki, T., Kohda, M., Nitta, J. & Takanashi, K. Coercivity change in an FePt thin layer in a Hall device by voltage application. *Appl. Phys. Lett.* **98,** 212505 (2011).

14. Shiota, Y., Murakami, S., Bonell, F., Nozaki, T., Shinjo, T. & Suzuki, Y. Quantitative Evaluation of Voltage-Induced Magnetic Anisotropy Change by Magnetoresistance Measurement. *Appl. Phys Express* **4,** 043005 (2011).

15. Shiota, Y., Nozaki, T., Bonell, F., Murakami, S., Shinjo, T. & Suzuki, Y. Induction of coherent magnetization switching in a few atomic layers of FeCo using voltage pulses. *Nat. Mater.* **11,** 39–43 (2011).

16. Wang, W.-G., Li, M., Hageman, S. & Chien, C. L. Electric-field-assisted switching in magnetic tunnel junctions. *Nat. Mater.* **11,** 64–68 (2011).

17. Bauer, U., Przybylski, M., Kirschner, J. & Beach, G. S. D. Magnetoelectric Charge Trap Memory. *Nano Lett.* **12,** 1437–1442 (2012).

18. Kanai, S., Yamanouchi, M., Ikeda, S., Nakatani, Y., Matsukura, F. & Ohno, H. Electric field-induced magnetization reversal in a perpendicular-anisotropy CoFeB-MgO magnetic tunnel junction. *Appl. Phys. Lett.* **101,** 122403 (2012).

19. Kita, K., Abraham, D. W., Gajek, M. J. & Worledge, D. C. Electric-field-control of magnetic anisotropy of Co0.6Fe0.2B0.2/oxide stacks using reduced voltage. *J. Appl. Phys.* **112,** 033919 (2012).

20. Liu, L., Pai, C.-F., Ralph, D. C. & Buhrman, R. A. Magnetic Oscillations Driven by the Spin Hall Effect in 3-Terminal Magnetic Tunnel Junction Devices. *Phys. Rev. Lett.* **109** (2012).

21. Meng, H., Sbiaa, R., Akhtar, M. A. K., Liu, R. S., Naik, V. B. & Wang, C. C. Electric field effects in low resistance CoFeB-MgO magnetic tunnel junctions with perpendicular anisotropy. *Appl. Phys. Lett.* **100,** 122405 (2012).

22. Nozaki, T. *et al.* Electric-field-induced ferromagnetic resonance excitation in an ultrathin ferromagnetic metal layer. *Nat. Phys.* **8,** 492–497 (2012).

23. Schellekens, A., van den Brink, A., Franken, J., Swagten, H. & Koopmans, B. Electric-field control of domain wall motion in perpendicularly magnetized materials. *Nat. Commun.* **3,** 847 (2012).

24. Skowroński, W., Wiśniowski, P., Stobiecki, T., Cardoso, S., Freitas, P. P. & van Dijken, S. Magnetic field sensor with voltage-tunable sensing properties. *Appl. Phys. Lett.* **101,** 192401 (2012).

25. Tournerie, N., Engelhardt, A. P., Maroun, F. & Allongue, P. Influence of the surface chemistry on the electric-field control of the magnetization of ultrathin films. *Phys. Rev. B* **86** (2012).

26. Zhu, J. *et al.* Voltage-Induced Ferromagnetic Resonance in Magnetic Tunnel Junctions. *Phys. Rev. Lett.* **108** (2012).

27. Nozaki, T., Yakushiji, K., Tamaru, S., Sekine, M., Matsumoto, R., Konoto, M., Kubota, H., Fukushima, A. & Yuasa, S. Voltage-Induced Magnetic Anisotropy Changes in an Ultrathin FeB Layer Sandwiched between Two MgO Layers. *Appl. Phys Express* **6,** 073005 (2013).

28. Bauer, U., Emori, S. & Beach, G. S. D. Voltage-controlled domain wall traps in ferromagnetic nanowires. *Nat. Nanotechnol.* **8,** 411–416 (2013).

29. Bonell, F., Lam, D., Yoshida, S., Takahashi, Y., Shiota, Y., Miwa, S., Nakamura, T. & Suzuki, Y. Investigation of Au and Ag segregation on Fe(001) with soft X-ray absorption. *Surf. Sci.* **616,** 125–130 (2013).

30. Rajanikanth, A., Hauet, T., Montaigne, F., Mangin, S. & Andrieu, S. Magnetic anisotropy modified by electric field in V/Fe/MgO(001)/Fe epitaxial magnetic tunnel junction. *Appl. Phys. Lett.* **103,** 062402 (2013).

31. Shiota, Y., Bonell, F., Miwa, S., Mizuochi, N., Shinjo, T. & Suzuki, Y. Opposite signs of voltage-induced perpendicular magnetic anisotropy change in CoFeB|MgO junctions with different underlayers. *Appl. Phys. Lett.* **103,** 082410 (2013).

32. Bauer, U., Przybylski, M. & Beach, G. S. D. Voltage control of magnetic anisotropy in Fe films with quantum well states. *Phys. Rev. B* **89** (2014).

33. Okada, A., Kanai, S., Yamanouchi, M., Ikeda, S., Matsukura, F. & Ohno, H. Electric-field effects on magnetic anisotropy and damping constant in Ta/CoFeB/MgO investigated by ferromagnetic resonance. *Appl. Phys. Lett.* **105,** 052415 (4, 2014).

34. Kanai, S., Gajek, M., Worledge, D. C., Matsukura, F. & Ohno, H. Electric field-induced ferromagnetic resonance in a CoFeB/MgO magnetic tunnel junction under dc bias voltages. *Appl. Phys. Lett.* **105,** 242409 (2014).

35. Naik, V. B., Meng, H., Xiao, J. X., Liu, R. S., Kumar, A., Zeng, K. Y., Luo, P. & Yap, S. Effect of electric-field on the perpendicular magnetic anisotropy and strain properties in CoFeB/MgO magnetic tunnel junctions. *Appl. Phys. Lett.* **105,** 052403 (2014).

36. Wisniowski, P., Dąbek, M., Skowronski, W., Stobiecki, T., Cardoso, S. & Freitas, P. P. Reduction of low frequency magnetic noise by voltage-induced magnetic anisotropy modulation in tunneling magnetoresistance sensors. *Appl. Phys. Lett.* **105,** 082404 (2014).

37. Miwa, S., Matsuda, K., Tanaka, K., Kotani, Y., Goto, M., Nakamura, T. & Suzuki, Y. Voltage-controlled magnetic anisotropy in Fe|MgO tunnel junctions studied by x-ray absorption spectroscopy. *Appl. Phys. Lett.* **107,** 162402 (2015).

38. Hirayama, E., Kanai, S., Ohe, J., Sato, H., Matsukura, F. & Ohno, H. Electric-field induced nonlinear ferromagnetic resonance in a CoFeB/MgO magnetic tunnel junction. *Appl. Phys. Lett.* **107,** 132404 (2015).

39. Nawaoka, K., Miwa, S., Shiota, Y., Mizuochi, N. & Suzuki, Y. Voltage induction of interfacial Dzyaloshinskii–Moriya interaction in Au/Fe/MgO artificial multilayer. *Appl. Phys Express* **8,** 063004 (2015).

40. Nawaoka, K., Shiota, Y., Miwa, S., Tomita, H., Tamura, E., Mizuochi, N., Shinjo, T. & Suzuki, Y. Voltage modulation of propagating spin waves in Fe. *J. Appl. Phys.* **117,** 17A905 (2015).

41. Skowroński, W., Nozaki, T., Lam, D. D., Shiota, Y., Yakushiji, K., Kubota, H., Fukushima, A., Yuasa, S. & Suzuki, Y. Underlayer material influence on electric-field controlled perpendicular magnetic anisotropy in CoFeB/MgO magnetic tunnel junctions. *Phys. Rev. B* **91** (2015).

42. Li, X. *et al.* Thermally stable voltage-controlled perpendicular magnetic anisotropy in Mo|CoFeB|MgO structures. *Appl. Phys. Lett.* **107,** 142403 (5, 2015).

43. Skowroński, W., Nozaki, T., Shiota, Y., Tamaru, S., Yakushiji, K., Kubota, H., Fukushima, A., Yuasa, S. & Suzuki, Y. Perpendicular magnetic anisotropy of Ir/CoFeB/MgO trilayer system tuned by electric fields. *Appl. Phys Express* **8,** 053003 (2015).

44. Tanaka, K., Miwa, S., Shiota, Y., Mizuochi, N., Shinjo, T. & Suzuki, Y. Large voltage-induced magnetic anisotropy field change in ferrimagnetic FeGd. *Appl. Phys Express* **8,** 073007 (2015).

45. Goto, M., Nawaoka, K., Miwa, S., Hatanaka, S., Mizuochi, N. & Suzuki, Y. Electric field modulation of tunneling anisotropic magnetoresistance in tunnel junctions with antiferromagnetic electrodes. *Japanese Journal of Applied Physics* **55,** 080304 (2016).

46. Nozaki, T., Kozioł-Rachwał, A., Skowroński, W., Zayets, V., Shiota, Y., Tamaru, S., Kubota, H., Fukushima, A., Yuasa, S. & Suzuki, Y. Large Voltage-Induced Changes in the Perpendicular Magnetic Anisotropy of an MgO-Based Tunnel Junction with an Ultrathin Fe Layer. *Phys. Rev. Appl* **5** (2016).

47. Park, K.-W., Park, J.-Y., Baek, S.-h. C., Kim, D.-H., Seo, S.-M., Chung, S.-W. & Park, B.-G. Electric field control of magnetic anisotropy in the easy cone state of Ta/Pt/CoFeB/MgO structures. *Appl. Phys. Lett.* **109,** 012405 (2016).

48. Hibino, Y., Koyama, T., Obinata, A., Hirai, T., Ota, S., Miwa, K., Ono, S., Matsukura, F., Ohno, H. & Chiba, D. Peculiar temperature dependence of electric-field effect on magnetic anisotropy in Co/Pd/MgO system. *Appl. Phys. Lett.* **109,** 082403 (2016).

49. Lau, Y.-C., Sheng, P., Mitani, S., Chiba, D. & Hayashi, M. Electric field modulation of the non-linear areal magnetic anisotropy energy. *Appl. Phys. Lett.* **110,** 022405 (2017).

50. Miwa, S. *et al.* Voltage controlled interfacial magnetism through platinum orbits. *Nat. Commun.* **8,** 15848 (2017).

51. Li, X. *et al.* Enhancement of voltage-controlled magnetic anisotropy through precise control of Mg insertion thickness at CoFeB|MgO interface. *Appl. Phys. Lett.* **110,** 052401 (2017).

52. Kozioł-Rachwał, A., Nozaki, T., Freindl, K., Korecki, J., Yuasa, S. & Suzuki, Y. Enhancement of perpendicular magnetic anisotropy and its electric field-induced change through interface engineering in Cr/Fe/MgO. *Sci. Rep.* **7** (2017).

53. Zhang, S. Spin-Dependent Surface Screening in Ferromagnets and Magnetic Tunnel Junctions. *Phys. Rev. Lett.* **83,** 640–643 (1999).

54. Duan, C.-G., Velev, J. P., Sabirianov, R. F., Zhu, Z., Chu, J., Jaswal, S. S. & Tsymbal, E. Y. Surface Magnetoelectric Effect in Ferromagnetic Metal Films. *Phys. Rev. Lett.* **101,** 137201 (2008).

55. Tsujikawa, M. & Oda, T. Finite Electric Field Effects in the Large Perpendicular Magnetic Anisotropy SurfacePt/Fe/Pt(001): A First-Principles Study. *Phys. Rev. Lett.* **102** (2009).

56. Nakamura, K., Shimabukuro, R., Fujiwara, Y., Akiyama, T., Ito, T. & Freeman, A. J. Giant Modification of the Magnetocrystalline Anisotropy in Transition-Metal Monolayers by an External Electric Field. *Phys. Rev. Lett.* **102** (2009).

57. Nakamura, K., Akiyama, T., Ito, T., Weinert, M. & Freeman, A. J. Role of an interfacial FeO layer in the electric-field-driven switching of magnetocrystalline anisotropy at the Fe/MgO interface. *Phys. Rev. B* **81** (2010).

58. Niranjan, M. K., Duan, C.-G., Jaswal, S. S. & Tsymbal, E. Y. Electric field effect on magnetization at the Fe/MgO(001) interface. *Appl. Phys. Lett.* **96,** 222504 (2010).

59. He, K. H., Chen, J. S. & Feng, Y. P. First principles study of the electric field effect on magnetization and magnetic anisotropy of FeCo/MgO(001) thin film. *Appl. Phys. Lett.* **99,** 072503 (2011).

60. Zhang, J., Lukashev, P. V., Jaswal, S. S. & Tsymbal, E. Y. Model of orbital populations for voltage-controlled magnetic anisotropy in transition-metal thin films. *Phys. Rev. B* **96,** 014435 (2017).

61. Bauer, U., Emori, S. & Beach, G. S. D. Electric field control of domain wall propagation in Pt/Co/GdOx films. *Appl. Phys. Lett.* **100,** 192408 (2012).

62. Bauer, U., Yao, L., Tan, A. J., Agrawal, P., Emori, S., Tuller, H. L., van Dijken, S. & Beach, G. S. D. Magneto-ionic control of interfacial magnetism. *Nat. Mater.* **14,** 174–181 (2014).

63. Bonell, F., Takahashi, Y. T., Lam, D. D., Yoshida, S., Shiota, Y., Miwa, S., Nakamura, T. & Suzuki, Y. Reversible change in the oxidation state and magnetic circular dichroism of Fe driven by an electric field at the FeCo/MgO interface. *Appl. Phys. Lett.* **102,** 152401 (2013).

64. Ong, P. V., Kioussis, N., Odkhuu, D., Amiri, P. K., Wang, K. L. & Carman, G. P. Giant voltage modulation of magnetic anisotropy in strained heavy metal/magnet/insulator heterostructures. *Phys. Rev. B* **92** (2015).

65. Sander, D. The correlation between mechanical stress and magnetic anisotropy in ultrathin films. *Rep. Prog. Phys.* **62,** 809 (1999).

66. BAUER, E. Phänomenologische Theorie der Kristallabscheidung an Oberflächen. I. *Zeitschrift für Kristallographie - Crystalline Materials* **110** (1958).

67. BAUER, E. Phänomenologische Theorie der Kristallabscheidung an Oberflächen. II. *Zeitschrift für Kristallographie - Crystalline Materials* **110** (1958).

68. Venables, J. A. Atomic processes in crystal growth. *Surf. Sci.* **299-300,** 798–817 (1994).

69. Tersoff, J., van der Gon, A. W. D. & Tromp, R. M. Critical island size for layer-by-layer growth. *Phys. Rev. Lett.* **72,** 266–269 (1994).

70. Henzler, M. Growth of epitaxial monolayers. *Surf. Sci.* **357-358,** 809–819 (1996).

71. Alex Hubert, R. S. *Magnetic Domains* (Springer-Verlag GmbH, 22, 2008).

72. Van Vleck, J. H. On the Anisotropy of Cubic Ferromagnetic Crystals. *Phys. Rev.* **52,** 1178–1198 (1937).

73. Coey, J. M. D. *Magnetism and Magnetic Materials* (Cambridge University Press, 2009).

74. Benson, H. & Mills, D. L. Spin Waves in Thin Films; Dipolar Effects. *Phys. Rev.* **178,** 839–847 (1969).

75. Heinrich, B., Purcell, S. T., Dutcher, J. R., Urquhart, K. B., Cochran, J. F. & Arrott, A. S. Structural and magnetic properties of ultrathin Ni/Fe bilayers grown epitaxially on Ag(001). *Phys. Rev. B* **38,** 12879–12896 (1988).

76. Draaisma, H. J. G. & de Jonge, W. J. M. Surface and volume anisotropy from dipole-dipole interactions in ultrathin ferromagnetic films. *J. Appl. Phys.* **64,** 3610–3613 (1988).

77. Heinrich, B., Cochran, J. F., Kowalewski, M., Kirschner, J., Celinski, Z., Arrott, A. S. & Myrtle, K. Magnetic anisotropies and exchange coupling in ultrathin fcc Co(001) structures. *Phys. Rev. B* **44,** 9348–9361 (1991).

78. Heinrich, B. & Cochran, J. Ultrathin metallic magnetic films: magnetic anisotropies and exchange interactions. *Adv. Phys.* **42,** 523–639 (1993).

79. Heinrich, B., Cochran, J. F., Arrott, A. S., Purcell, S. T., Urquhart, K. B., Dutcher, J. R. & Egelhoff, W. F. Development of magnetic anisotropies in ultrathin epitaxial films of Fe(001) and Ni(001). *Appl. Phys. A.* **49,** 473–490 (1989).

80. Gradmann, U. Magnetic surface anisotropies. *J. Magn. Magn. Mater.* **54-57,** 733–736 (1986).

81. Heinrich, B., Celinski, Z., Cochran, J. F., Arrott, A. S. & Myrtle, K. Magnetic anisotropies in single and multilayered structures (invited). *J. Appl. Phys.* **70,** 5769–5774 (1991).

82. Brockmann, M., Miethaner, S., Onderka, R., Köhler, M., Himmelhuber, F., Regensburger, H., Bensch, F., Schweinböck, T. & Bayreuther, G. In-plane spin reorientation transition in ultrathin epitaxial Fe(001) films. *J. Appl. Phys.* **81,** 5047–5049 (1997).

83. Brockmann, M., Zolfl, M., Miethaner, S. & Bayreuther, G. In-plane volume and interface magnetic anisotropiesin epitaxial Fe films on GaAs(001). *J. Magn. Magn. Mater.* **198-199,** 384–368 (1999).

84. Néel, L. Anisotropie magnétique superficielle et surstructures d'orientation. *J. Phys. Radium* **15,** 225–239 (1954).

85. Den Broeder, F., Hoving, W. & Bloemen, P. Magnetic anisotropy of multilayers. *J. Magn. Magn. Mater.* **93,** 562–570 (1991).

86. Bruno, P. Tight-binding approach to the orbital magnetic moment and magnetocrystalline anisotropy of transition-metal monolayers. *Phys. Rev. B* **39,** 865–868 (1989).

87. Daalderop, G. H. O., Kelly, P. J. & Schuurmans, M. F. H. Magnetic anisotropy of a free-standing Co monolayer and of multilayers which contain Co monolayers. *Phys. Rev. B* **50,** 9989–10003 (1994).

88. Weller, D., Wu, Y., Stöhr, J., Samant, M. G., Hermsmeier, B. D. & Chappert, C. Orbital magnetic moments of Co in multilayers with perpendicular magnetic anisotropy. *Phys. Rev. B* **49,** 12888–12896 (1994).

89. Nakajima, N., Koide, T., Shidara, T., Miyauchi, H., Fukutani, H., Fujimori, A., Iio, K., Katayama, T., Nývlt, M. & Suzuki, Y. Perpendicular Magnetic Anisotropy Caused by Interfacial Hybridization via Enhanced Orbital Moment inCo/PtMultilayers: Magnetic Circular X-Ray Dichroism Study. *Phys. Rev. Lett.* **81,** 5229–5232 (1998).

90. Monso, S., Rodmacq, B., Auffret, S., Casali, G., Fettar, F., Gilles, B., Dieny, B. & Boyer, P. Crossover from in-plane to perpendicular anisotropy in Pt/CoFe/AlOx sandwiches as a function of Al oxidation: A very accurate control of the oxidation of tunnel barriers. *Appl. Phys. Lett.* **80,** 4157–4159 (2002).

91. Rodmacq, B., Auffret, S., Dieny, B., Monso, S. & Boyer, P. Crossovers from in-plane to perpendicular anisotropy in magnetic tunnel junctions as a function of the barrier degree of oxidation. *J. Appl. Phys.* **93,** 7513–7515 (2003).

92. Manchon, A. *et al.* Analysis of oxygen induced anisotropy crossover in Pt/Co/MOx trilayers. *J. Appl. Phys.* **104,** 043914 (2008).

93. Nistor, L. E., Rodmacq, B., Auffret, S. & Dieny, B. Pt/Co/oxide and oxide/Co/Pt electrodes for perpendicular magnetic tunnel junctions. *Appl. Phys. Lett.* **94,** 012512 (2009).

94. Li, C. & Freeman, A. J. Giant monolayer magnetization of Fe on MgO: A nearly ideal two-dimensional magnetic system. *Phys. Rev. B* **43,** 780–787 (1991).

95. Urano, T. & Kanaji, T. Atomic and Electronic Structure of Ultrathin Iron Film on MgO(001)Surface. *Journal of the Physics Society Japan* **57,** 3403–3410 (1988).

96. Meyerheim, H. L., Popescu, R., Kirschner, J., Jedrecy, N., Sauvage-Simkin, M., Heinrich, B. & Pinchaux, R. Geometrical and Compositional Structure at Metal-Oxide Interfaces: MgO on Fe(001). *Phys. Rev. Lett.* **87** (2001).

97. Yang, H. X., Chshiev, M., Dieny, B., Lee, J. H., Manchon, A. & Shin, K. H. First-principles investigation of the very large perpendicular magnetic anisotropy at Fe|MgO and Co|MgO interfaces. *Phys. Rev. B* **84** (2011).

98. Hallal, A., Yang, H. X., Dieny, B. & Chshiev, M. Anatomy of perpendicular magnetic anisotropy in Fe/MgO magnetic tunnel junctions: First-principles insight. *Phys. Rev. B* **88** (2013).

99. Bochi, G., Song, O. & O'Handley, R. Surface magnetoelastic coupling coefficients of single-crystal fcc Co thin films. *Phys. Rev. B* **50,** 2043 (1994).

100. Jungblut, R., Johnson, M. T., aan de Stegge, J., Reinders, A. & den Broeder, F. J. A. Orientational and structural dependence of magnetic anisotropy of Cu/Ni/Cu sandwiches: Misfit interface anisotropy. *J. Appl. Phys.* **75,** 6424–6426 (1994).

101. Song, O., Ballentine, C. A. & O'Handley, R. C. Giant surface magnetostriction in polycrystalline Ni and NiFe films. *Appl. Phys Letters* **64,** 2593 (1994).

102. Bochi, G., Ballentine, C. A., Inglefield, H. E., Thompson, C. V. & O'Handley, R. C. Evidence for strong surface magnetoelastic anisotropy in epitaxial Cu/Ni/Cu(001) sandwiches. *Phys. Rev. B* **53,** R1729–R1732 (1996).

103. Koch, R., Weber, M., Thürmer, K. & Rieder, K. Magnetoelastic coupling of Fe at high stress investigated by means of epitaxial Fe(001) films. *J. Magn. Magn. Mater.* **159,** L11–L16 (1996).

104. Wedler, G., Walz, J., Greuer, A. & Koch, R. Stress dependence of the magnetoelastic coupling constants B_1 and B_2 of epitaxial Fe(001). *Phys. Rev. B* **60,** R11313–R11316 (16 1999).

105. Tian, Z., Sander, D. & Kirschner, J. Nonlinear magnetoelastic coupling of epitaxial layers of Fe, Co, and Ni on Ir(100). *Phys. Rev. B* **79,** 024432 (2 2009).

106. Gowtham, P. G., Stiehl, G. M., Ralph, D. C. & Buhrman, R. A. Thickness-dependent magnetoelasticity and its effects on perpendicular magnetic anisotropy in Ta/CoFeB/MgO thin films. *Phys. Rev. B* **93** (2016).

107. Johnson, M. T., Bloemen, P. J. H., den Broeder, F. J. A. & de Vries, J. J. Magnetic anisotropy in metallic multilayers. *Rep. Prog. Phys.* **59,** 1409–1458 (1996).

108. Bruno, P. & Renard, J.-P. Magnetic Surface Anisotropy of Transition Metal Ultrathin Films. *Appl. Phys. A* **49,** 499–506 (1989).

109. Sander, D. The magnetic anisotropy and spin reorientation of nanostructures and nanoscale films. *J. Phys.: Condens. Matter* **16,** R603–R636 (2004).

110. Chen, J. & Erskine, J. L. Surface-step-induced magnetic anisotropy in thin epitaxial Fe films on W(001). *Phys. Rev. Lett.* **68,** 1212–1215 (1992).

111. Park, Y., Fullerton, E. E. & Bader, S. D. Growth-induced uniaxial in-plane magnetic anisotropy for ultrathin Fe deposited on MgO(001) by oblique-incidence molecular beam epitaxy. *Appl. Phys. Lett.* **66,** 2140 (1995).

112. Zhan, Q.-f., Vandezande, S., Haesendonck, C. V. & Temst, K. Manipulation of in-plane uniaxial anisotropy in Fe/MgO(001) films by ion sputtering. *Appl. Phys. Lett.* **91,** 122510 (2007).

113. Krebs, J. J., Jonker, B. T. & Prinz, G. A. Properties of Fe single-crystal films grown on (100)GaAs by molecular-beam epitaxy. *J. Appl. Phys.* **61,** 2596 (1987).

114. Wilgocka-Ślęzak, D., Freindl, K., Kozioł, A., Matlak, K., Rams, M., Spiridis, N., Ślęzak, M., Ślęzak, T., Zając, M. & Korecki, J. Thickness-driven polar spin reorientation transition in ultrathin Fe/Au(001) films. *Phys. Rev. B* **81** (2010).

115. Urquhart, K. B., Heinrich, B., Cochran, J. F., Arrott, A. S. & Myrtle, K. Ferromagnetic resonance in ultrahigh vacuum of bcc Fe(001) films grown on Ag(001). *J. Appl. Phys.* **64,** 5334–5336 (1988).

116. Dutcher, J. R., Cochran, J. F., Heinrich, B. & Arrott, A. S. Brillouin light scattering studies on an iron whisker. *J. Appl. Phys.* **64,** 6095–6097 (1988).

117. Liu, C. & Bader, S. D. Perpendicular surface magnetic anisotropy in ultrathin epitaxial Fe films. *J. Vac. Sci. Technol. A* **8,** 2727–2731 (1990).

118. Ohno, H., Chiba, D., Matsukura, F., Omiya, T., Abe, E., Dietl, T., Ohno, Y. & Ohtani, K. Electric-field control of ferromagnetism. *Nature* **408,** 944–946 (21, 2000).

119. Weisheit, M., Fahler, S., Marty, A., Souche, Y., Poinsignon, C. & Givord, D. Electric Field-Induced Modification of Magnetism in Thin-Film Ferromagnets. *Science* **315,** 349–351 (2007).

120. Awschalom, D. D. & Flatté, M. E. Challenges for semiconductor spintronics. *Nat. Phys.* **3,** 153–159 (2007).

121. Song, C., Cui, B., Li, F., Zhou, X. & Pan, F. Recent progress in voltage control of magnetism: Materials, mechanisms, and performance. *Prog. Mater Sci.* **87,** 33–82 (Supplement C 1, 2017).

122. Bi, C., Liu, Y., Newhouse-Illige, T., Xu, M., Rosales, M., Freeland, J., Mryasov, O., Zhang, S., te Velthuis, S. & Wang, W. Reversible Control of Co Magnetism by Voltage-Induced Oxidation. *Phys. Rev. Lett.* **113** (2014).

123. Newhouse-Illige, T. *et al.* Voltage-controlled interlayer coupling in perpendicularly magnetized magnetic tunnel junctions. *Nat. Commun.* **8,** 15232 (2017).

124. Arrot, A. S. *Ultrathin Magnetic Structures 1* (ed J.A.C. Bland, B. H.) (Springer Nature, 2005).

125. Pelzl, J., Meckenstock, R., Spoddig, D., Schreiber, F., Pflaum, J. & Frait, Z. Spin–orbit-coupling effects on g -value and damping factor of the ferromagnetic resonance in Co and Fe films. *J. Phys.: Condens. Matter* **15,** S451 (2003).

126. Woltersdorf, G. *Spin pumping and two magnon scattering in magnetic multilayers* PHD (Simon Fraser University, Burnaby Canada, 2004).

127. Celinski, Z., Urquhart, K. B. & Heinrich, B. Using ferromagnetic resonance to measure the magnetic moments of ultrathin films. *J. Magn. Magn. Mater.* **166,** 6–26 (1, 1997).

128. Smit, J. & Beljers, H. G. Ferromagnetic Resonance Absorption in $BeFe_{12}O_{19}$, a highly Anisotropic Crystal. *Philips research reports* **10,** 113–130 (1955).

129. Suhl, H. Ferromagnetic Resonance in Nickel Ferrite Between One and Two Kilomegacycles. *Phys. Rev.* **97,** 555–557 (1955).

130. Kerr, J. On Rotation of the Plane of Polarization by Reflection from the Pole of a Magnet. *Philos. Mag.* **3,** 321 (1877).

131. Kerr, J. Reflection of Polarized Light from the Equatorial Surface of a Magnet. *Philos. Mag.* **5,** 161 (1878).

132. Ding, H., Pütter, S., Oepen, H. & Kirschner, J. Experimental method for separating longitudinal and polar Kerr signals. *J. Magn. Magn. Mater.* **212,** 5–11 (2000).

133. Moog, E. R., Liu, C., Bader, S. D. & Zak, J. Thickness and polarization dependence of the magnetooptic signal from ultrathin ferromagnetic films. *Phys. Rev. B* **39,** 6949–6956 (1989).

134. Moog, E. R., Bader, S. D. & Zak, J. Role of the substrate in enhancing the magneto-optic response of ultrathin films: Fe on Au. *Appl. Phys. Lett.* **56,** 2687 (1990).

135. Zak, J., Moog, E., Liu, C. & Bader, S. Universal approach to magneto-optics. *J. Magn. Magn. Mater.* **89,** 107–123 (1990).

136. Suzuki, Y., Katayama, T., Yoshida, S., Tanaka, K. & Sato, K. New magneto-optical transition in ultrathin Fe(100) films. *Phys. Rev. Lett.* **68,** 3355–3358 (1992).

137. Suzuki, Y., Katayama, T., Geerts, W., .Grünberg, P., Takanashi, K., Schreiber, R., Bruno, P. & Yuasa, S. Magneto-Optical Effects of Ultrathin Ferro-, Antiferro- and Non-Magnetic Films. *MRS Proceedings* **475,** 227 (1997).

138. Buchmeier, M., Schreiber, R., Bürgler, D. E. & Schneider, C. M. Thickness dependence of linear and quadratic magneto-optical Kerr effects in ultrathin Fe(001) films. *Phys. Rev. B* **79** (2009).

139. Katayama, T., Suzuki, Y., Awano, H., Nishihara, Y. & Koshizuka, N. Enhancement of the magneto-optical Kerr rotation in Fe/Cu bilayered films. *Phys. Rev. Lett.* **60,** 1426–1429 (1988).

140. Zak, J., Moog, E. R., Liu, C. & Bader, S. D. Magneto-optics of multilayers with arbitrary magnetization directions. *Phys. Rev. B* **43,** 6423–6429 (1991).

141. *Ultrathin Magnetic Structures II* (eds Heinrich, B. & Bland, J. A. C.) (Springer Nature, 1994).

142. Braun, W. *Applied RHEED* 236 pp. (Springer, 20, 2013).

143. O'Hanlon, J. F. *A User's Guide to Vacuum Technology* 536 pp. (John Wiley and Sons Ltd, 22, 2003).

144. ICHIMIYA, A. & COHEN, P. I. . *Reflection High Energy Electron Deflection* (Cam, 2004).

145. Hottier, F. & Theeten, J. B. Comparative LEED and RHEED examination of stepped surfaces; application to Cu(111) and GaAs(001) vicinal surfaces. *Surf. Sci.* **65,** 563–577 (1977).

146. Pukite, P. R., Batra, S. & Cohen, P. I. Anisotropic Growth Processes On GaAs(100) And Ge(100). *SPIE, Growth of Compound Semiconductors* **796,** 22 (1987).

147. Woltersdorf, G. & Heinrich, B. Two-magnon scattering in a self-assembled nanoscale network of misfit dislocations. *Phys. Rev. B* **69,** 184417 (2004).

148. Sudijono, J., Johnson, M. D., Snyder, C. W., Elowitz, M. B. & Orr, B. G. Surface evolution during molecular-beam epitaxy deposition of GaAs. *Phys. Rev. Lett.* **69,** 2811–2814 (1992).

149. Hopkins, J., Leys, M., Brübach, J., van der Vleuten, W. & Wolter, J. A RHEED study of the dynamics of GaAs and AlGaAs growth on a (001) surface by MBE. *Appl. Surf. Sci.* **84,** 299–307 (1995).

150. Monsma, D. & Becker, J. The Savannah ALD System - An Excellent Tool for Atomic Layer Deposition. *Material Matters* **1,** 5–7 (2006).

151. Brunner, S. *Optimierung von* Al_2O_3*-Isolationsschichtenauf GaAs hergestellt mit Atomlagenabscheidung* Bachelors thesis (Universität Regensburg, 2012).

152. Ribow, M. *Antiferromagnetically Coupled Tunneling Strucures based on Silicon* Diploma thesis (Universität Regensburg, 2011).

153. Qiu, Z. Q. & Bader, S. D. Surface magneto-optic Kerr effect. *Rev. Sci. Instrum.* **71,** 1243 (2000).

154. Ding, H. F., Pütter, S., Oepen, H. P. & Kirschner, J. Spin-reorientation transition in thin films studied by the component-resolved Kerr effect. *Phys. Rev. B* **63** (2001).

155. Farle, M., Silva, T. & Woltersdorf, G. in *Magnetic Nanostructures* DOI: 10.1007/978-3-642-32042-2_2, 37–83 (Springer, Berlin, Heidelberg, 2013).

156. Sicot, M., Andrieu, S., Tiusan, C., Montaigne, F. & Bertran, F. On the quality of molecular-beam epitaxy grown Fe/MgO and Co/MgO(001) interfaces. *J. Appl. Phys.* **99,** 08D301 (2006).

157. Zhan, Q.-f., Vandezande, S., Temst, K. & Haesendonck, C. V. Magnetic anisotropies of epitaxial Fe/MgO(001) films with varying thickness and grown under different conditions. *New J. Phys.* **11,** 063003 (2009).

158. Spiridis, N. & Korecki, J. Influence of Au reconstruction on growth of Fe on Au(100). *Appl. Surf. Sci.* **141,** 313–318 (1999).

159. Keavney, D. J., Fullerton, E. E. & Bader, S. D. Perpendicular conductance and magnetic coupling in epitaxial Fe/MgO/Fe(100) trilayers. *J. Appl. Phys.* **81,** 795 (1997).

160. Vassent, J., Marty, A., Gilles, B. & Chatillon, C. Thermodynamic analysis of molecular beam epitaxy of MgO(s) I. MgO vaporization by electron bombardment. *J. Cryst. Growth* **219,** 434–443 (2000).

161. Green, A. K., Dancy, J. & Bauer, E. Insignificance of Lattice Misfit for Epitaxy. *J. Vac. Sci. Technol.* **7,** 159 (1970).

162. Palmberg, P. W., Rhodin, T. N. & Todd, C. J. Epitaxial growth of gold and silver on magnesium oxide cleaved in ultrahigh vacuum. *Appl. Phys. Lett.* **11,** 33 (1967).

163. Sheng, P., Bang, D., Nozaki, T., Miwa, S. & Suzuki, Y. Spin-dependent quantum well effect in fully epitaxial Cr/ultrathin Fe/MgO/Fe magnetic tunnel junctions. *Solid State Commun.* **152,** 273–277 (2012).

164. Jiang, Q., He, Y.-L. & Wang, G.-C. Thermal stability and intermixing of ultrathin Fe films on a Au(001) surface. *Surf. Sci.* **295,** 197–212 (1993).

165. Brockmann, M. *Epitaxie und magnetische in-plane-Anisotropie dünner Fe(001)-Schichten auf Au(001) und GaAs(001)* PHD (Universität Regensburg, Regensburg Germany, 2004).

166. Mezey, L. Z. & Giber, J. The Surface Free Energies of Solid Chemical Elements: Calculation from Internal Free Enthalpies of Atomization. *Jpn. J. Appl. Phys.* **21,** 1569–1571 (1982).

167. Himpsel, F. J. Fe on Au(100): Quantum-well states down to a monolayer. *Phys. Rev. B* **44,** 5966–5969 (1991).

168. He, Y.-L. & Wang, G.-C. Observation of atomic place exchange in submonolayer heteroepitaxial Fe/Au(001) films. *Phys. Rev. Lett.* **71,** 3834–3837 (1993).

169. Begley, A. M., Kim, S. K., Quinn, J., Jona, F., Over, H. & Marcus, P. M. Growth of ultrathin films of Fe on Au001. *Phys. Rev. B* **48,** 1779–1785 (1993).

170. Hernán, O., de Parga, A. V., Gallego, J. & Miranda, R. Self-surfactant effect on Fe/Au(100): place exchange plus Au self-diffusion. *Surf. Sci.* **415,** 106–121 (1998).

171. Karaś, W., Handke, B., Krop, K., Kubik, M., Ślęzak, T., Spiridis, N., Wilgocka-Ślęzak, D. & Korecki, J. CEMS Studies of Au/Fe/Au Ultrathin Films and Monoatomic Multilayers. *Phys. Status Solidi A* **189,** 287–292 (2002).

172. Opitz, R., Löbus, S., Thissen, A. & Courths, R. An angle-scanned photoelectron diffraction (XPD) study of the growth and structure of ultrathin Fe films on Au(001). *Surf. Sci.* **370,** 293–310 (1997).

173. Blum, V. *et al.* Fe thin-film growth on Au(100): A self-surfactant effect and its limitations. *Phys. Rev. B* **59,** 15966–15974 (1999).

174. Sano, K.-i. & Miyagawa, T. Surface Segregations during Epitaxial Growth of Fe/Au Multilayers on GaAs(001). *Jpn. J. Appl. Phys.* **30,** 1434–1441 (1991).

175. Kawagoe, T., Kotaki, T., Shibasaki, T., Ohmori, Y. & Itoh, A. The temperature-dependent growth of Fe submonolayer film on Au(001) studied by barrier height imaging using scanning tunneling microscopy. *Surf. Sci.* **468,** 1–9 (2000).

176. Vassent, J. L., Dynna, M., Marty, A., Gilles, B. & Patrat, G. A study of growth and the relaxation of elastic strain in MgO on Fe(001). *J. Appl. Phys.* **80,** 5727 (1996).

177. Klaua, M., Ullmann, D., Barthel, J., Wulfhekel, W., Kirschner, J., Urban, R., Monchesky, T. L., Enders, A., Cochran, J. F. & Heinrich, B. Growth, structure, electronic, and magnetic properties of MgO/Fe(001) bilayers and Fe/MgO/Fe(001) trilayers. *Phys. Rev. B* **64,** 134411 (2001).

178. Wulfhekel, W., Klaua, M., Ullmann, D., Zavaliche, F., Kirschner, J., Urban, R., Monchesky, T. & Heinrich, B. Single-crystal magnetotunnel junctions. *Appl. Phys. Lett.* **78,** 509 (2001).

179. Popova, E. *et al.* Epitaxial MgO layer for low-resistance and coupling-free magnetic tunnel junctions. *Appl. Phys. Lett.* **81,** 1035 (2002).

180. Tiusan, C., Faure-Vincent, J., Bellouard, C., Hehn, M., Jouguelet, E. & Schuhl, A. Interfacial Resonance State Probed by Spin-Polarized Tunneling in Epitaxial F e / M g O / F e Tunnel Junctions. *Phys. Rev. Lett.* **93** (2004).

181. Tasker, P. & Duffy, D. The structure and properties of the stepped surfaces of MgO and NiO. *Surf. Sci.* **137,** 91–102 (1984).

182. Miwa, S. & Suzuki, Y. private communication. 2015.

183. Nibarger, J. P., Lopusnik, R., Celinski, Z. & Silva, T. J. Variation of magnetization and the Landé g factor with thickness in Ni–Fe films. *Appl. Pyhs. Lett.* **83,** 93–95 (2003).

184. Amara-Dababi, S., Sousa, R. C., Chshiev, M., Béa, H., Alvarez-Hérault, J., Lombard, L., Prejbeanu, I. L., Mackay, K. & Dieny, B. Charge trapping-detrapping mechanism of barrier breakdown in MgO magnetic tunnel junctions. *Appl. Phys. Lett.* **99,** 083501 (2011).

185. Baldrati, L., Tan, A. J., Mann, M., Bertacco, R. & Beach, G. S. D. Magneto-ionic effect in CoFeB thin films with in-plane and perpendicular-to-plane magnetic anisotropy. *Appl. Phys. Lett.* **110,** 012404 (2, 2017).

186. Sim Jung, J., Rha, S.-H., Ki Kim, U., Jang Chung, Y., Soo Jung, Y., Choi, J.-H. & Seong Hwang, C. The charge trapping characteristics of Si $_3$ N $_4$ and Al $_2$ O $_3$ layers on amorphous-indium-gallium-zinc oxide thin films for memory application. *Appl. Phys. Lett.* **100,** 183503 (30, 2012).

187. Prinz, G. A. Stabilization of bcc Co via Epitaxial Growth on GaAs. *Phys. Rev. Lett.* **54,** 1051–1054 (1985).

188. Dekoster, J., Jedryka, E., Mény, C. & Langouche, G. Epitaxial growth of bcc Co/Fe superlattices. *J. Magn. Magn. Mater.* **121,** 69–72 (1993).

Acknowledgement

Foremost I want to thank Professor Georg Woltersdorf for giving me the opportunity to conduct this thesis under his supervision. He is by far the most impressive experimentator if have ever met and I am genuinely thank-full for everything I learned from him.

I want to thank Liane Brandt who built up the (modified) MOKE setup and measured the magnetization and modulation curves discussed in this thesis.

I want to thank Rouven Dreyer who is responsible for the TR-MOKE setup and measured the FMR spectra discussed in this thesis.

I want to thank Prof. Georg Schmidt for giving me the opportunity to use the clean room facilities of the IZM and in particular the Ar^{+}-ion milling system.

For the critical reading of (parts of) this thesis I would like to thank Professor Georg Woltersdorf and (appearing in alphabetical order) Liane Brandt, Rouven Dreyer, Chris Körner, Niklas Liebing, Simon Wisotzki and Emilia Wisotzki.

Finally I want to thank all my family members, friends and colleagues for their support.

Curriculum Vitae

Mirko Ribow
Carl-Robert-Str. 37
06114 Halle (Saale)

mirko.ribow@gmail.com
+49(0)176 32083499

Date & place of birth: 02.03.1984, Ochsenhausen (Germany)

Education

10/2011 - 11/2017	PhD in physics at the Martin-Luther university Halle-Wittenberg and university of Regensburg Thesis: Voltage control of magnetic anisotropy in ultrathin epitaxial magnetic layers Supervisor: Prof. Dr. Georg Woltersdorf
04/2005 - 10/2011	Studies of physics at the university of Regensburg Thesis: Antiferromagnetic coupled tunnel structures based on Si Degree: Diploma (1.4) Supervisor: Prof. Dr. Christian Back
10/2004 - 04/2005	Studies of chemistry at the university of Regensburg
05/2004 - 09/2009	Willibald-Gymnasium in Eichstätt Degree: Abitur

Publications and conference contributions

Publications

Ribow, M., Brandt, L., & Woltersdorf, G. Thickness dependent voltage control of magnetic anisotropy in ultrathin iron *submitted* (2017)

Seifert, T., Martens, U., Radu, I., Wolf, M., Münzenberg, M., Ribow, M., Woltersdorf, G. & Kampfrath, T. The anomalous Hall conductivity of magnetic metals is flat from DC up to 40 terahertz *submitted* (2017)

Melnikov, A., Razdolski, I., Ribow, M., Brandt, L., & Woltersdorf, G. THz spin waves generated generated by spin torque in ultrathin iron layers *in preparation* (2017)

Wei, D., Obstbaum, M., Ribow, M., Back, C. H. & Woltersdorf, G. Spin Hall voltages from a.c. and d.c. spin currents. *Nat. Commun.* **5** (2014)

Conference contributions

M. Ribow, L. Brandt and G. Woltersdorf
Quantifying the electric field induced change of magnetic anisotropy in ultrathin Fe layers
DPG Spring Meeting, poster (Dresden 2017)

Erklärung

Hiermit erkläre ich, dass ich diese Arbeit selbstständig und ohne fremde Hilfe verfasst, keine anderen als die von mir angegebenen Quellen und Hilfsmittel benutzt und die den Werken wörtlich oder inhaltlich entnommenen Stellen als solche erkenntlich gemacht habe.

Halle (Saale), November 2017 Mirko Ribow